Critical Components in Microfluidic Systems for Drug Delivery

Bitsch, Lennart

Publication date:
2006

Document Version
Publisher's PDF, also known as Version of record

PhD thesis, s960370

Critical components in microfluidic systems for drug delivery:

energy consumption in safe, turning microvalves

Lennart Bitsch

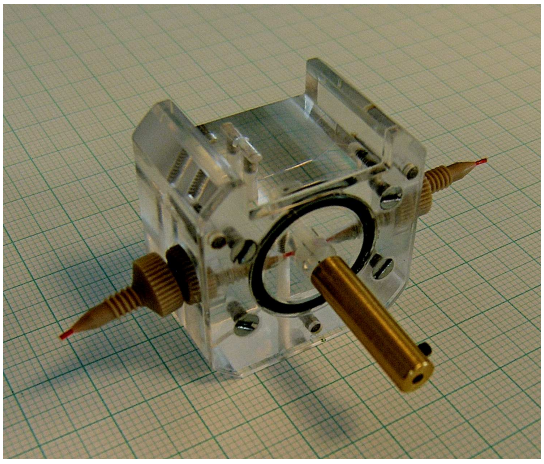

Supervisor: Henrik Bruus
Co-supervisor: Jörg P. Kutter

MIC – Department of Micro and Nanotechnology
Technical University of Denmark

Industrial supervisor: Torben Storgaard-Larsen

Diabetes Research Unit
Novo Nordisk A/S

27 June 2006

Abstract

The goal of this thesis has been to evaluate microfluidic systems for applications in drug delivery. In particular, we have focused on safety in reciprocating pumps, for continuous insulin delivery, and identified the microvalves, as being critical components.

We have investigated a technology for engineering of microfluidic components which promises good sealing properties. A good sealing property is a mean to ensure a high safety level for applications in drug delivery, and we have used the technology to fabricate a turning microvalve, which provides a significantly higher safety level compared to delivery systems using prestressed check valves.

The technology is based on construction with soft incompressible rubber materials and hard surfaces. By basic studies on sliding friction between rubber and a hard substrate we show that friction force scales with contact area, and depends linearly on the contact pressure. Therefore, energy savings are obtained by down-scaling. Similar basic flow studies show that sealing properties depend on contact pressure, and how well the rubber-incompressibility is utilized in the actual geometry. In addition to the basic studies, scaling properties and dependency on contact pressure for turning valves are illustrated by construction and test of a large and a small turning valve. Therefore, low-energy, turning microvalves with high-pressure seals are feasible.

The major benefits of down-scaling mechanical systems are the more compact and less energy consuming devices. We show the feasibility of a low-energy, turning microvalve with a high pressure seal by construction and test of a demonstrator with a rod diameter of 250 μm, the actuation energy of opening and closing is 0.15 mJ, and it withstand a pressure above 0.7 MPa.

We have also used the studied technology to suggest the design and construction of a pump in an unexplored branch of micropumps, namely, the reciprocating piston pump. The pump utilizes turning microvalves to rectify the fluid flow, and it appears feasible to construct true micro-scale demonstrators of this pump. Further optimization and understanding of the friction processes could therefore provide a pump which is attractive for drug delivery.

Resumé

Formålet med denne afhandling har været at evaluere mulighederne for at anvende mikrofluide systemer til medicinsk behandling. Vi har især fokuseret på sikkerhed i reciprokerende pumper, med henblik på en kontinuer insulin behandling, og har identificeret mikroventiler som værende kritiske komponenter.

Vi har undersøgt en teknologi til fremstilling af mikrofluide komponenter, der lover gode pakningsegenskaber. En pakning med gode tæthedsegenskaber er et middel til at opnå et højt sikkerhedsniveau i forbindelse med medicinsk behandling, og vi har brugt teknologien til fabrikation af en dreje-mikroventil. Sammenlignet med systemer der benytter passive ventiler opnår vi et markant højere sikkerhedsniveau med en drejeventil.

Teknologien bygger på konstruktion med bløde inkompressible gummimaterialer, og hårde overflader. Grundlæggende studier af dynamisk friktion mellem gummi og en hård overflade viser at friktions kraften skalerer med kontaktarealet og stiger lineært med kontakttrykket. Derfor kan man opnå en energibesparelse ved at gøre systemet mindre. Ved lignende grundlæggende studier med væskeflow har vi vist at pakningsegenskaberne afhænger af kontakttrykket, og hvor godt gummiets inkompressibilitet er udnyttet i den aktuelle geometri. I tillæg til de basale studier, har vi vha. ventiltests vist hvordan energiforbrug og pakningsegenskaber afhænger af kontaktareal og kontakttrykket. Dette er illustreret ved konstruktion og test af en stor og en lille drejeventil. På det grundlag er det muligt at fremstille dreje-mikroventiler med gode pakninsgsegenskaber.

De overvejende fordele ved nedskalering af mekaniske systemer er mere kompakte, lavenergi-apparater. Vi har vist muligheden for at lave dreje-mikroventiler med lavt energiforbrug og gode pakningsegenskaber ved konstruktion og test af en demonstrator med en stiftdiameter på 250 μm. Akturingsenergien for at åbne og lukke er 0,15 mJ, og ventilen modstår tryk på over 0,7 MPa.

Vi har ligeledes benyttet den studerede teknologi til at fremsætte et forslag til design og konstruktion af en pumpe i et uberørt felt for mikroventiler, nemlig, reciprokerende stempelpumper. Pumpen benytter dreje-mikroventiler til at ensrette flowet, og en fremstilling af mikroskala pumper med denne teknologi virker plausibel. Yderligere optimering og forståelse af friktionsprocesserne kunne derfor muliggøre en pumpe der er attraktiv til medicinsk behandling.

Preface

The thesis is a part of the requirements in obtaining the PhD degree from the Technical University of Denmark (DTU) under the Industrial PhD Initiative of the Ministry of Science Technology and Innovation (VTU). The Industrial PhD Initiative aims at enhancing research and development in the Danish business sector, and the focus in this thesis is, therefore, both on research and its application.

The project has been carried out in a collaboration between Novo Nordisk A/S and MIC - Department of Micro and Nanotechnology at DTU. Novo Nordisk is a focused health care company with a long history in diabetes care, and the departure of this project has, therefore, been insulin delivery systems.

When I started at Novo Nordisk in April 2003 I was challenged by one the R&D engineers in table football. During the match I came under heavy pressure, and my strikers were surprisingly inefficient. In a desperate moment I tried to develop a better technique, which appeared spectacular, but with an even more inefficient outcome. The match was at that moment entitled the classical derby between the experienced R&D-engineer and the PhD student, where the latter was focusing on typical "PhD tricks" that looked good, but did not work. It is my hope that this thesis will contribute to the development of new technology that also works.

I would like to acknowledge the very valuable assistance from colleagues at both Novo Nordisk and MIC. In particular I would like to thank Jan Jacobsen, Bjørn G. Larsen, Steffen Hansen, Jan Preuthun, Ole Christian Nielsen, Gabriel Jørgensen, Ion M. Sivebæk, Klaus Bendix, Bo Pedersen, Mogens Papsøe, Mogens Juhl Nielsen, Per Elgaard, Ole Hansen, Laurits Olesen, Mads Jakob Jensen, and Anders Brask for fruitful discussions on design, fabrication, and test. A special thanks to colleagues and friends in the Microfluidic Theory and Simulation group (MIC), and Device Simulation (Novo Nordisk) for the warm and inspiring working environment. I would also like to thank family and friends for cheery comments, when things worked and when they did not.

Finally, I would like to express my gratitude to my industrial supervisor Torben Storgaard-Larsen, for initiating this project, and for excellent supervision. Also, without the extraordinary supervision and continuous support from my two academic supervisors Henrik Bruus and Jörg P. Kutter, this project would have been impossible.

Lennart Bitsch
MIC – Department of Micro and Nanotechnology
Technical University of Denmark
27 June 2006

Contents

List of Figures

List of Tables

List of symbols

Symbol	Description	Unit
A	Area	m^2
a	Length scale	m
A_{an}	Apparent nominal area	m^2
A_{rc}	Area of real contact	m^2
A_1	Torque model, Area	m^2
D_{f}	PIV, focal depth	m
D_h	Hydraulic diameter	m
f	frequency	Hz
F_{bal}	Force on balance	N
F_n	Normal force	N
F_N	Normal force	N
F_t	Tangential force	N
g	Gravitational acceleration	$\mathrm{m\,s}^2$
H_1	Torque model, height	m
h	PIV, height of channel	m
I	PIV, intensity	Dimensionless
k_c	Correction to elastic module	dimensionless
k_e	Theoretical elastic module	$\mathrm{Pa\,m}^{-1}$
k_m	Emperical elastic module (measured)	$\mathrm{Pa\,m}^{-1}$
L	Length	m
L_{lev}	Length of lever	m
L_1	Plug-sealing model, length	m
ℓ_p	Length of perimeter	m
ℓ_1	Plug-sealing model, length	m
ℓ_2	Hydraulic resistor model, length	m
m_{bal}	Measured, mass on balance	kg
n	Speed	rps
$\tilde{p}$	Dimensionless pressure	Dimensionless
p	Pressure	Pa
p^0_{leak}	Setup, leakage threshold pressure	Pa
p_{th}	Threshold pressure	Pa
Q_{acc}	Accumulating flow rate	$\mathrm{m}^3\,\mathrm{s}^{-1}$

Symbol	Description	Unit
Q_{bal}	Measured flow rate	$\mathrm{m^3\,s^{-1}}$
Q_{leak}	Plug-sealing flow rate	$\mathrm{m^3\,s^{-1}}$
Q_p	Measured, pressure derived flow rate	$\mathrm{m^3\,s^{-1}}$
Q_{pump}	Set flow rate	$\mathrm{m^3\,s^{-1}}$
R_{hyd}	Hydraulic resistance	$\mathrm{Pa\,s\,m^{-3}}$
R_{hi}	Hydraulic resistance, inlet	$\mathrm{Pa\,s\,m^{-3}}$
R_{hp}	Hydraulic resistance, plug	$\mathrm{Pa\,s\,m^{-3}}$
R_{he}	Hydraulic resistance, edge	$\mathrm{Pa\,s\,m^{-3}}$
R_{ho}	Hydraulic resistance, outlet	$\mathrm{Pa\,s\,m^{-3}}$
R_1	Plug-sealing model, rod radius	m
R_2	Torque model, rod radius	m
r_1	Plug-sealing model, inner tube radius	m
r_2	Plug-sealing model, outer tube radius	m
r_3	Torque model, inner tube radius	m
r_4	Torque model, outer tube radius	m
Re	Reynolds number	Dimensionless
Re	Transitional Reynolds number	Dimensionless
T_g	Glass transition temperature	K
t_0	Time sample	s
t_1	Time sample	s
t_2	Time sample	s
t_3	Time sample	s
u_1	Plug-sealing model, displacement	m
u_2	Plug-sealing model, displacement	m
u_3	Plug-sealing model, displacement	m
u_4	Plug-sealing model, displacement	m
u_5	Torque model, displacement	m
u_6	Hydraulic resistor model, displacement	m
v	velocity	$\mathrm{m\,s^{-1}}$
$\tilde{\mathbf{v}}$	Dimensionless velocity vector	Dimensionless
$v_{\mathrm{conv}}(z)$	PIV, convolved velocity	$\mathrm{m\,s^{-1}}$
v_{max}	Max. velocity	$\mathrm{m\,s^{-1}}$
V_{mean}	Mean velocity	$\mathrm{m\,s^{-1}}$
v_{NS}	PIV, theoretical velocity	$\mathrm{m\,s^{-1}}$
$v_{\mathrm{PIV}}(z)$	PIV, experimental velocity	$\mathrm{m\,s^{-1}}$
w	velocity	$\mathrm{m\,s^{-1}}$
x, y, z	Spatial coordinates	
z	PIV, distance from focal plane	m
z_1	Plug-sealing model, length	m
z_2	Plug-sealing model, length	m
Δp	Plug-sealing model, pressure	Dimensionless

Symbol	Description	Unit
ϵ	Fitting parameter	Dimensionless
η	Friction coefficient	Dimensionless
θ	Angle	rad
μ	Dynamic viscosity	Pa s
ρ	Density	$\mathrm{kg\,m^{-3}}$
σ_{rr}	Pressure	Pa
$\sigma_v(z)$	PIV, estimate of vel. errorbar	m
$\sigma_{r\theta}$	Friction stress	m^2
τ	Torque	N m
τ_{mot}	Torque delivered by motor	m^2

Chapter 1

Introduction

Diabetes is a life threatening condition and affects millions of people. According to the World Health Organization [1] (WHO) the number of diabetics in year 2000 was 171 million and the number is expected to reach 366 million in 2030. In other words, the number of incidents is increasing rapidly, and this thread to the global public health is getting worse.

The mission of WHO Diabetes Programme is to prevent diabetes, and, where that is not possible, to minimize the complications and increase quality of life [1]. Preventing diabetes is unfortunately out of the scope for the present work, and we will therefore focus on the latter part. More concrete, we will from a technical point of view study the possibilities of improving safety and convenience of current therapies. We shall be concerned with the challenge of improving current drug delivery systems, and our main goal will be for applications in diabetes.

1.1 Diabetes

Diabetes is a highly complex disease, and we will in this chapter give a short introduction to the most relevant aspects, which should provide an understanding for the basic treatment.

Diabetes is a disease where the body does not regulate the blood glucose level properly. The blood glucose level is the amount of glucose in the circulating blood, and glucose is the fuel needed to keep biological processes in the cells running.

Insulin is a hormone controlling the entry of glucose into the cells, and when the blood insulin level, the concentration of insulin in the blood, is insufficient this entry is impaired.

There are different types of the disease, and the most common are referred to as type 1 and type 2 diabetes. Fig. 1.1 illustrates the blood insulin level during the day for a healthy person, and two persons with type 1 and type 2 diabetes, respectively. For a healthy person the insulin level can be considered as a basal level with an additional contribution or bolus which peaks around mealtimes. To illustrate the complexity of the natural regulation, it would be reasonable to anticipate that an increasing insulin level is initiated by an increasing glucose level, but as a matter of fact the concentration of insulin

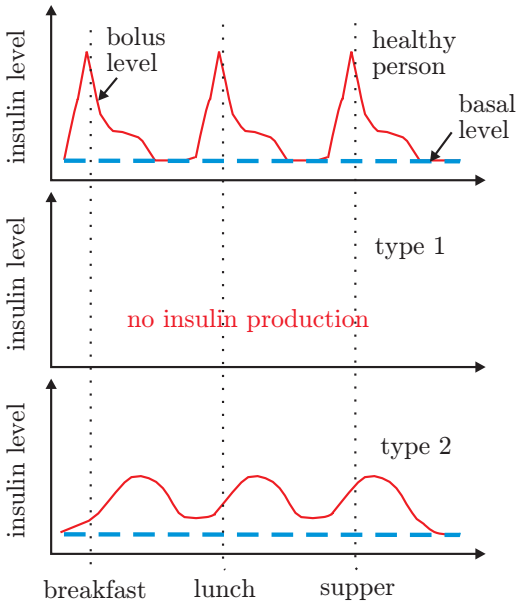

Figure 1.1: Blood insulin level in three different cases. The upper graph resembles the regulation for a normal functioning person, where the insulin level is seen to peak around the daily meals. This profile is sometimes considered as an additional contribution on top of a basal level. The basal level is indicated on the figure. The middle graph shows the level for a person with type 1 diabetes, where no natural blood insulin is present. The lower graph shows the blood insulin level for a person with type 2 diabetes. In this case, the body produce an insufficient amount of insulin, and cells are less sensitive to insulin. The picture is redrawn from Ref. [2]

increases even before mealtimes. In other words, expectations of a future meal is preparing the body on an expected increase in glucose concentration. People with type 1 diabetes do not produce insulin, whereas people with type 2 diabetes produce an insufficient amount, and their cells are, furthermore, less sensitive to insulin.

1.2 Living with diabetes

Type 2 diabetes can to some extent be treated with tablets to stimulate the natural insulin production, or the insulin sensitivity. Type 1 diabetes can today only be treated with insulin, which is injected under the skin. This is referred to as subcutaneous delivery, and is necessary as an oral introduction will result in a digestion of the molecule, and, consequently, no blood glucose regulation. Pulmonary delivery (delivery across lung tissue) appears also feasible, and future delivery systems are aiming at utilizing this entry.

Insulin is a very potent drug. If too much insulin is injected, the blood glucose concentration is reduced to a critical limit, and the person may become unconscious and, in the worst case, die. A too low glucose concentration, is referred to as a hypoglycemic incidence, and it is a short term complication. The opposite case, hyperglycemia, can

result in long term complications like blindness, kidney failure, and amputations. Long term complications of a poorly controlled diabetes are seen within eight to ten years.

Conventionally type 1 diabetes is treated with multiple daily injections and blood glucose measurements. For a well controlled diabetes it is necessary to perform several injections and measurements each day [3]. The number of all these extra daily routines may result in lack of flexibility, and reduced quality of life, and a therapy which minimizes such concerns is desired.

Clearly, the ideal treatment would automatically resemble the insulin level of a healthy functioning body, and the strategy has, therefore, been to combine a long-acting with a short-acting insulin analogue. The long-acting analogue is a modified human insulin molecule, which acts over a long time and to some extend resembles the basal rate. The short-acting analogue is injected before mealtimes, and resembles the bolus rate. Such a treatment is referred to as a basal-bolus therapy, and although it approaches the natural regulation, it is obviously not automatic.

In recent years there has been advances in pump therapy, which also is known as therapy with continuous subcutaneous insulin infusion (CSII). Today, insulin pumps on the size of a box of playing cards can be attached on a belt and connected to the patient by an infusion set. The pump is then delivering a short-acting insulin in accordance with the desired profile.

The ultimate goal for a device administrated treatment is to combine continuous glucose measurements with a continuous infusion system in a closed loop regulation. However, the insulin dosing is not solely dependent on glucose level, and there are also different individual time scales that need to be considered.

For type 1 diabetics, the ultimate treatment is probably found in therapy with stem cells, where the objective is to grow and implement new beta-cells, which are the cells responsible for insulin production in a normal functioning body. However, type 1 diabetes is a result of an auto-immune response, where the body's own immune system destroys the beta-cells. Therefore, if new beta-cells are implemented they would still need a protection against the immune system.

1.3 Structure of thesis

In Chapter 2, the thesis departs in an analysis of current insulin pumps. The aim is to identify critical components, and the pumps are primarily evaluated in terms of safety and convenience. On this basis, it is decided to focus on the valve function, as it is a determining factor of the safety level. As silicone based systems are most suitable for liquid handling, we chose to develop our components with a technology involving a soft rubber

and a hard substrate. Increased convenience is an inherited property of microtechnology, as miniaturization is regarded as a mean for such an improvement. Chapter 3 is an outline of the basic concepts and frameworks necessary to analyze and characterize microfluidic systems, and in particular micro valves involving rubber friction. This leads to Chapter 4, where we establish two basic models to support our experimental study on sliding friction, the so-called threshold pressure, and leakage. The threshold pressure being the pressure to induce a leakage. Chapter 5 describes experiments and results on basic sealing properties, and the dependencies on friction between rubber and a hard substrate. In particular we study the dependency on contact area, as down-scaling is a way to reduce actuation energy of sliding friction. In Chapter 6 we characterize different realizations of turning valves, and utilize the developed models to predict the performance. Conclusion and outlook are presented in Chapter 7, where we sketch how the technology can be used for the construction of a piston micropump.

1.4 Publications during this thesis

Peer reviewed journal papers

1. *Low-energy, turning microvalve with high-pressure seal: sealing and friction.* Lennart Bitsch, Jörg P. Kutter, Torben Storgaard-Larsen, Henrik Bruus, JMM, (submitted 2006) [4]. Also shown in Appendix B.

2. *Micro particle-image velocimetry of bead suspensions and blood flows.* L. Bitsch, L.H. Olesen, C.H. Westergaard, H. Bruus, H. Klank, and J.P. Kutter Exp. Fluids **39**, 507 (2005) [5].

Conference proceedings

1. *Minimization of performance variations in microfluidic components using the method of robust design*, Lennart Bitsch, Henrik Bruus, and Jörg P. Kutter MicroTAS-2004, Malmö, Sweden, September 2004, proc. vol. 1, p. 572-574 [6]. Also shown in Appendix B.

2. *Micro PIV on blood flow in a microchannel*, Lennart Bitsch, Laurits H. Olesen, Carsten H. Westergaard, Henrik Bruus, Henning Klank, and Jörg P. Kutter. MicroTAS 2003, Lake Tahoe, USA, October 2003, proc. vol. 1, p. 825-828 [7].

3. *Transmission micro PIV resolving velocities normal to the focal plane*, Lennart Bitsch, Laurits H. Olesen, Carsten H. Westergaard, Henrik Bruus, Henning Klank, and Jörg P. Kutter MicroTAS 2003, Lake Tahoe, USA, October 2003, proc. vol. 1, p. 821-824 [8].

Patent applications

1. *Pump assembly with active and passive valve*, Lennart Bitsch, Torben Storgaard-Larsen, and Ole Christian Nielsen, 2005 (patent pending) [9].

Chapter 2

Microfluidics, critical components, and project focus

As stated in Chapter 1, the problem related to diabetes is that some people are unable to regulate the blood glucose concentration by natural means. To get straight to the point, it is our challenge to provide insulin by means of a drug delivery system, and, thereby, resemble the function of a normal body. Despite the fact that fairly small insulin pumps are already available on the market, we will in this chapter discuss how microfluidics can add new value to pump therapy, evaluate the current state of the technology (microfluidics), and define the focus of this thesis.

2.1 Microfluidics and drug delivery: a market survey

The discussion will take its departure in a market survey on microfluidics in life sciences. The survey, *FlowMap Microfluidics Roadmap* [10], is edited by Ducrée and Zengerle (2004), and is the work of a consortium of different European stakeholders within life sciences. According to their findings, the requirements for success in pumps for insulin delivery will be miniaturization, increase in accuracy, low energy consumption, and reliability. It is suggested that high costs could be permissible for high quality products, and especially for long term implantable pumps. As microfluidics, indeed, is an enabling technology for smaller, more efficient and accurate devices, focus on this area could be warranted.

Despite the fact that research on micropumps has been ongoing for the last two decades, the technology has, according to the survey, not properly matured. Still, more focus is needed on functional integration, and the facilities for high volume manufacturing are also insufficient. Some additional problems as regulatory issues, the conservativeness of the medical market are also mentioned, but the latter issues are not of a technical engineering character, and are not to be discussed further here.

		SI unit		Diabetes related/technical unit
Min. basal increment	0.27	$\mathrm{nL\,s^{-1}}$	0.1	$\mathrm{unit\,h^{-1}}$
Max. bolus flow rate	20	$\mu\mathrm{L\,s^{-1}}$	2	$\mathrm{unit\,s^{-1}}$
Reservoir size	3	mL	300	unit
Package size	30	mL	10	reservoir size
Battery	58	J	16	mAh

Table 2.1: Assumed specifications to an insulin micropump. Assumed battery: Varta lithium button ML 1220, size 0.24 mL, 3 V nominal voltage, 2 mA continuous current. One insulin unit (1 unit) is 10 μL. Inspiration to the specifications has been found on www.diabetesnet.com [11].

2.2 Current insulin pumps and micropumps

We will now analyze existing delivery systems and micropumps. In this way we establish the system specifications, which enables us to evaluate the feasibility of current technologies and pumping concepts.

Current insulin infusion devices are designed and fabricated with increased functionality, and are thereby becoming more and more complex. An overview of old, current and future insulin pumps can be found on diabetesnet.com [11], and the trend is clearly towards smaller, more convenient, and more functional devices that eases the administration of the complex treatment. Some of the hardware to provide these additional functions are memory, and communication platforms, and even though these technologies are important in a broad view, we shall concentrate on the system that is essential for liquid handling. We will refer to such a system as the basic portable delivery device, which on the first level consists of a power source, an actuator, and a fluidic system. On the next level of details, the fluidic system involves a reservoir, a pump mechanism, and an infusion system.

Insulin pump specifications
As the field of micropumps has existed for a couple of decades a number of pump reviews have already been published [12, 13]. This makes the overview and selection process easier, but, due to the technological complexity, a large challenge is still remaining in understanding qualities and problems in the different pumps.

If we use the number of publications as an indicator of maturity, one of the most mature concepts for pumping of small volumes is the reciprocating diaphragm pump with rectifying valves, as this type has more than 40 references in the mentioned review by Laser and Santiago [13]. As technological maturity is a prerequisite for applications in insulin delivery, we chose this pumping concept for further studies.

Table 2.1 contains the assumed specifications for an attractive micropump, where the website www.diabetesnet.com [11] has served as inspiration. Even though pump therapy is referred to as continuous delivery, the flow is in reality discrete. The minimum basal increment is a measure for the stroke volume, and if we for example dose in discrete steps of three minutes the stroke volume would be around 50 nL. As a comparison, the pump

chip by Maillefer [14] has a 160 nL stroke volume. The maximum bolus flow rate is given in units per second (unit s^{-1}), but a bolus duration may be around 30 seconds.

2.3 Critical components in reciprocating pumps

According to Ref. [13] positive displacement pumps can be divided into diaphragm and piston pumps, where the latter still is unseen in microscale pumps. Diaphragm pumps are also referred to as membrane pumps, which we preferably use in this thesis.

Highly inspired by the review of Woias *et al.*[12], we shall take a look on the history of the development of membrane micropumps. A miniature piezoelectric pump, and valves with electronic controls have been proposed for insulin dosing by Spencer *et al.* [15]. The disadvantage of this design is that high voltages are used for actuation, and the actuators are immersed into the pumped fluid, which is a potential hazard.

This problem was addressed by Smits [16] who constructed a membrane pump operated in a peristaltic way, where the actuators were separated from the pumped fluid. However, a disadvantage is still the high actuation voltage, and a risk for free fluid flow, if a large pressure should develop on the inlet side. The opening pressure increases with the stiffness of the membrane, but the stiffness has to be limited in such a way that it can be opened by the available actuation force. If we chose a large stiffness, we require a large actuation force, i.e, there is a conflict between a high safety level, and low energy consumption.

Another option has been the use of a single actuated pump membrane, where check valves are guiding the fluid flow. To avoid free flow, a third valve is added after the outlet check valve. This valve is connected to the inlet channel, and is, therefore, forced to close, when the inlet pressure increases [17]. However, there is a potential hazard in separating inlet and outlet only by a flexible wall. There may also be concerns related to the dynamic performance of such a system, and dose accuracy with the introduction of additional compliance, but so far this is only the authors speculation.

A different approach has been to pre-stress the inlet valve to give a higher opening pressure of 10 kPa [14]. However, when the opening pressure is exceeded the fluid can flow freely. Furthermore, pumping energy is lost in the process of deflecting the check valves.

Many problems relating to microfluidics are due to the rigid nature of silicon. Silicon has for historical reasons been chosen as a basis, as it offered many well known processes for micro-engineering. In Ref. [18] this problem was addressed, with the construction of flexible channels, where the flow could be pinched off with a strong pressure seal, due to the perfect adaption of the material. It may not be the first time a flexible rubber is used for microfluidic engineering purposes, but on the website www.fluidigm.com [19], where the technology is commercialized, this is mentioned as one of the reasons to the technical success of these valves. However, with respect to the useability in a portable system, it is a drawback for the valves in Ref. [18] that strong seals will require a strong actuator.

Hasselbrink *et al.*[20] have constructed passive plug valves in a rubber material and have characterized the nature of static friction in such systems. Kirby *et al.*[21] have realized the valves in a different configuration to obtain active valves.

2.4 Actuators

The overall performance of a drug delivery system is obviously dependent on the available actuators. Many different means to transform energy into motion has been explored, and a review is given in Ref. [22]. Some of the reviewed methods include electromechanical, thermomechanical, piezoelectric, magnetostrictive, electrohydrodynamic, electrostatic, phase change, shape memory, electrorheological, and diamagnetism.

We will be particularly interested in more conventional actuators as electromagnetic motors, as they also are commercial available in small and compact versions. For example Faulhaber [23] offers a micro brushless DC-motor with a diameter and length of 2 and 6.8 mm, respectively. The motor delivers a torque of 7.5 μN m without gearing.

2.5 Focus of the thesis

We shall in this thesis be primarily concerned with safety and energy consumption. Valves are critical components with respect to safety, and we will describe a valve which can provide a strong pressure seal without or with a limited increase in energy consumption. However, the goal is not just the construction of a device, but also the basic knowledge, which should enable us to tailor similar components.

Another concern of this thesis goes on methodology. As mentioned, an important criterion for a successful micropump is robustness and reliability, as inaccurate dosing can have fatal consequences. By robustness is meant that small variations in the construction and operation should not lead to a pump malfunction. In that aspect public research on micropumps appears to offer very little attention. Therefore, we shall in this thesis draw attention to this area.

2.5.1 Characterization and design of active micro valves

An often used valve is a passive check valve, but we would like to investigate the possibilities of using active valves, as they may offer interesting features with respect to safety, as it enables the capability of completely to shut-off for fluid flow in case of emergency. One way of characterizing active valves is by their stable modes, i.e., the mode they enter when the power is off [24]. The modes are, normally closed, normally open or bi-stable. An additional way of categorization of the valves could be by the way they operate, and we will in this way define three types of active valves. This categorization is gate valves, active-material valves, and pinch valves.

Fig. 2.1 illustrates the principles of how the different active valves are functioning. Fig. 2.1(a1) and (a2) shows the gate valve. The gate valve slides across the channel and blocks the flow. A gate valve can also be a turning valve, where the through going bore in a rod or a ball is parallel or transverse to the direction of flow. In principle, a gate valve could also be a check valve configuration, where the gate or boss is actively pulled in an upstream direction, in order to bring it in an open state. However, when the pressure across the valve increases, so will the actuation energy. Gate valves can be designed to be self-sealing, which means the pressure seal increases with the pressure drop across the

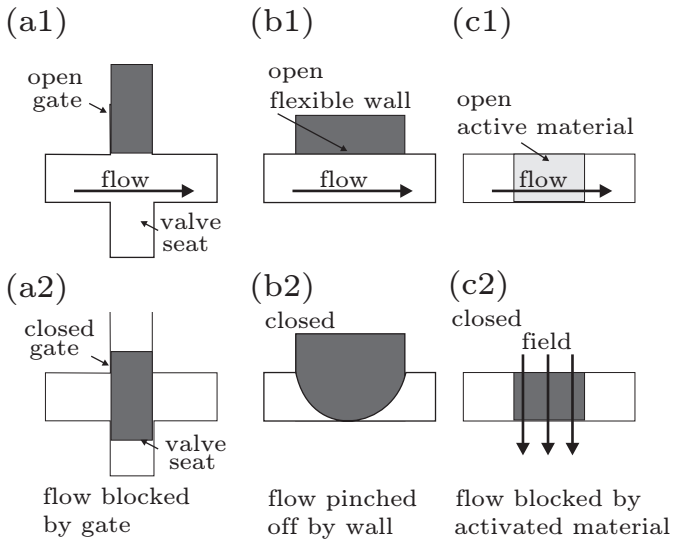

Figure 2.1: Categorization of active valves by the way they operate. The valves are sketched in their open and closed state. (a1) Open gate valve, (a2) closed gate valve, (b1) open pinch valve, (b2) closed pinch valve, (c1) open active material valve. When the active material is exposed to a field, it blocks the flow. (c2) Closed active material valve.

valve. Examples of gate valves are found in Ref. [25, 27]. Fig. 2.1(b1) and (b2) shows the pinch valve in its two states. When a pressure is applied on the channel wall, it pinches off the flow. The valve is not self-sealing, and a large fluid pressure requires a large force to seal the channel. An example of a pinch valve is found in Ref. [18]. Fig. 2.1(c1) and (c2) shows an active material valve in its open and closed state, respectively. The flow channel contains an active material, which block the channel, when it is exerted to a field. It could for example be a fluid containing magnetic particles, which is effected by a magnetic field Ref. [26]. The active material valve is not self sealing.

According to this categorization the only self sealing valve is the gate valve, which is a highly desirable feature, as it does not require additional actuation force to seal. The gate valves by Frank *et al.*[27] are made in silicon, but we would prefer silicone rubber, which promises good sealing properties cheaper manufacturing costs for high volume production.

We therefore chose to construct and study a turning rod valve made in silicone rubber as it is self-sealing, and promises low energy consumption. Depending on the actuator it can be normally open, normally closed, or even designed to only use energy in the switching process.

2.6 Summary

In this chapter, we have discussed the most important issues for construction of an insulin delivery system. We have chosen to focus on safety, and convenience in a small compact design. This leads to the focus on active microvalves of the gate type. In the next chapter, we discuss basic concepts for studying and characterization of such valves.

Chapter 3

Basic concepts

3.1 Fluid dynamics

We shall later, in Chapter 4, develop a model to describe the basic sealing properties, and we shall, therefore, briefly review the governing equations of an incompressible liquid

$$Re\Big(\tilde{\partial}_t\tilde{\mathbf{v}} + (\tilde{\mathbf{v}}\cdot\tilde{\boldsymbol{\nabla}})\tilde{\mathbf{v}}\Big) = -\tilde{\boldsymbol{\nabla}}\tilde{p} + \tilde{\boldsymbol{\nabla}}^2\tilde{\mathbf{v}}, \tag{3.1a}$$

$$\tilde{\boldsymbol{\nabla}}\cdot\tilde{\mathbf{v}} = 0, \tag{3.1b}$$

where $\tilde{\mathbf{v}}$ is a dimensionless velocity vector, $\tilde{p}$ is the dimensionless pressure. In Eq. (3.1a), first and second term on the left-hand side is a transient and convective term, respectively. These terms are also referred to as inertial terms, as they can come into play when inertial forces dominate. On the right-hand side we have the pressure gradient, and a term related to the viscous loss. Re is the Reynolds number and is interpreted as the ratio between inertial and viscous forces

$$Re = \frac{\rho a v}{\mu}, \tag{3.2}$$

where ρ is the mass density, a a characteristic length scale, v the linear velocity and μ the dynamic viscosity. Due to the small dimensions and moderate fluid velocities, the Reynolds number is small and we usually disregard the inertial terms on the left-hand side side of Eq. (3.1a). More specific, when viscous forces dominate we have a laminar flow, but where the Reynolds number exceed the transitional Reynolds number Re_t, we can expect a transition to a turbulent flow, where the inertial terms should be considered. The transitional Reynolds number is given by

$$Re_t = 30L/D_h, \tag{3.3}$$

where L and D_h is the length of the flow channel, and the hydraulic diameter, respectively. The hydraulic diameter is defined as $D_h = 4A/\ell_p$, where A is the cross sectional area, and ℓ_p is the length of the perimeter. If the flow channel is a circular tube, the hydraulic and circle diameter are identical. Re_t increases with decreasing D_h, but if the channel length is small, we can also observe inertial effects in microfluidic components, as shown by Gravesen *et al.* [28].

3.2 Flow characterization using μPIV

Usually, calculations of flow fields are experimentally verified, by measuring corresponding volume flow rates and dynamic pressures. Although, this gives a good indication of the actual flow field, it is not a direct observation. Especially in more complex geometries, and for non-Newtonian fluids as blood, a direct experimental measurement can be valuable. Such a possibility is offered by particle-image velocimetry (PIV), where high speed imaging of flow patterns, enables a direct and non-invasive measurement of the flow velocity field. However, a prerequisite is optical access to the flow, and for characterization of flow in microstructures we will need to image through a microscope. The technique is, therefore, referred to as microPIV or μPIV.

We have investigated the possibilities in using μPIV, for characterization of blood in micro structures, which is regarded as a rather complex fluid flow. However, in order to study the blood flow, we had to investigate the performance of the optical system, i.e., how well we could resolve the different planes in the flow. Therefore, tracer particles suspended in water was studied in a flat capillary to verify the system, and afterwards blood flow was studied in the same geometry. The following is an extract of our paper *Micro PIV on blood flow in a microchannel* [7].

3.2.1 Micro particle-image velocimetry of bead suspensions and blood flows

Studies of blood flow in microsystems presented in the literature often focus on measurements and models of the relation between flow rates and pressure drops[29], without utilizing the support of PIV. One exception is Sugii *et al.*[30] who presented an in vivo PIV experiment of blood flow. However, they did not investigate the influence of velocity gradients normal to the focal plane. Furthermore, the measurements were not compared to theoretical profiles.

Using μPIV in a transmission setup, we have measured velocity profiles of bead suspensions and blood flows in a flat glass capillary with a roughly rectangular cross-section of size 28 μm by 360 μm. Restricted to observations in a given focal plane μPIV has previously proven successful in both transmission and epi-fluorescent mode [31, 32]. We extend these results by taking into account the finite spatial resolution normal to the focal plane, the so-called focal depth, imposed by our optical system, and we present the first direct observation of the influence of the focal depth on the obtained experimental velocity profiles. Our analysis is based on the theoretical expression for the visibility of particles slightly out-of-focus derived by Olsen and Adrian[33]. For fluids with a high density of particles, such as blood, it can be difficult to determine the position of boundaries parallel to the focal plane. We show that these boundaries are related to a steep increase in the size of the errorbars of the measurements. The measurements on blood strongly indicate that blood in these dimensions flows as a plug flow and that it should be modelled as a two-phase flow. Moreover, we find indications of the presence of a 3 μm wide cell free boundary layer.

First we present the details of our μPIV setup. This is followed by the central concept

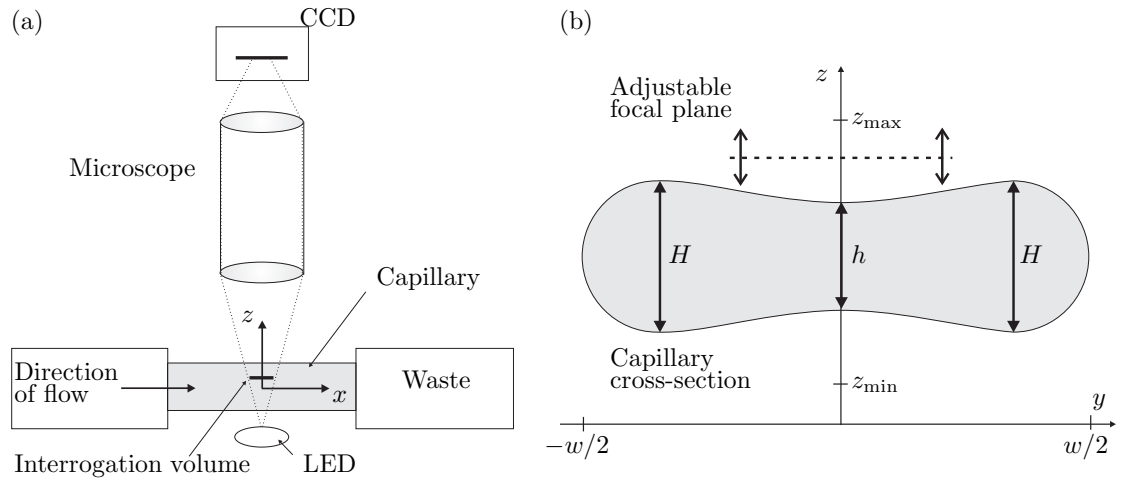

Figure 3.1: Sketch of PIV setup. (a) A sketch of the experimental setup containing the microfluidic system, the interrogation volume, the LED, the optical system, and the CCD camera. (b) The actual channel cross section in the yz plane obtained by optical inspection. The dimensions are $H = 32.5$ μm, $h = 28$ μm and $w = 360$ μm. The z-axis is normal to the focal plane. The velocity profiles were scanned by moving the focal plane (dotted line) between $z_{\min}$ and $z_{\max}$, 35 μm above and 25 μm below the channel, respectively.

of the focal depth, and a description of the theoretical expression for the convolved velocity field. We finish the extract from our paper with a discussion of the results.

3.2.2 The measurement setup for micro PIV

The measurement setup for μPIV is sketched in Fig. 3.1(a). It is centered around an optical microscope using a CCD camera to record images of the flow of blood or bead suspensions through the capillary. The capillary is placed horizontally in the microscope and illuminated from below by a high intensity light-emitting diode (LED) with a maximum intensity at a wavelength of 450 nm. The transmitted light is focused onto a CCD-camera. Camera and LED were synchronized and controlled by a FlowMap$^{(\mathrm{TM})}$ System Hub from Dantec Dynamics. The interrogation volume, indicated on the figure, is the volume focused onto the CCD.

A cross section of the capillary is seen in Fig. 3.1(b). During experiments it was filled with the fluid from a syringe pump. The flow rates were 50 nL s^{-1} for the bead suspension and 167 nL s^{-1} for blood.

An experiment consisted of a series of PIV measurements, where the horizontal focal plane was moved vertically down through the channel, as sketched in Fig. 3.1(b). In that way the velocity gradient could be resolved in the direction normal to the focal plane.

A PIV measurement consisted of 25 pairs of images recorded with intervals of 1 s. The time lapse between the two images in a pair was 500 μs, and the exposure time for each single image was given by the 100 μs LED pulses.

From each pulse pair an instantaneous velocity field of the particle images could be

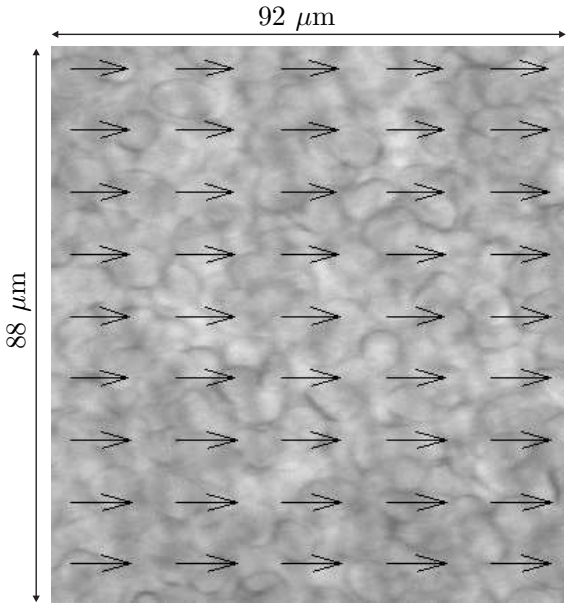

Figure 3.2: An example of a velocity field obtained for a flow measurement on blood. The map is 92 μm wide and 88 μm high. The blood cells are observed as dark rings, and the average velocity of some interrogation areas are indicated with an arrow.

calculated. As an example the velocity field for a blood flow measurement is seen in Fig. 3.2.

3.2.3 Theoretical velocity fields

The measured velocity fields from the μPIV analysis need to be compared with theoretical velocity fields. These are found by solving the Navier-Stokes equation with a constant negative pressure gradient along the flow direction and with the no-slip boundary conditions for the velocity at the channel walls.

For the bead suspension, being a Newtonian liquid, the calculated Navier-Stokes velocity field v_{NS} can be thought of as the well-known paraboloid Poiseuille profile being distorted at the boundary to fit the dumbbell shape depicted in Fig. 3.1(b) rather than a circular shape.

The non-Newtonian character of blood leads to a further distortion of the Poiseuille flow in the form of a more blunt velocity profile close to the center of the capillary. Due to the small dimension of the channel compared to the size of the red blood cells, another option is to model the fluid as a two-phase system.

However, in our μPIV experiments we expect to observe neither of these two simple Navier-Stokes velocity fields. Even though, we have performed a truncation in intensity levels, the remaining optical depth of our system will cause a pick-up of out-of-focus signals. Recently, Olsen and Adrian derived a theoretical expression for the visibility of particles slightly out-of-focus [33]. A particularly simple limiting case of their result is a

Lorentzian visibility function $I(z)$ given by

$$I(z) = \left(1 + \frac{4z^2}{D_{\mathrm{f}}^2}\right)^{-1}, \tag{3.4}$$

where I is the intensity, D_{f} is the focal depth (spatial resolution normal to the focal plane), and z is the vertical distance from the focal plane.

Using the simplified visibility function $I(z)$ we can model the distorted velocity field $v_{\mathrm{conv}}(z)$ as a convolution integral of the simple theoretical velocity field $v_{\mathrm{NS}}(z)$ with the visibility function:

$$v_{\mathrm{conv}}(z) = \frac{\int_{-h/2}^{h/2} v_{\mathrm{NS}}(z')\, I(z'-z)\, dz'}{\int_{-h/2}^{h/2} I(z'-z)\, dz'}, \tag{3.5}$$

where h is the height of the channel.

A theoretical estimate of the error bars $\sigma_v(z)$ can be obtained as being inversely proportional to the square root of the amount of statistical data,

$$\sigma_v(z) \propto \left[\int_{-h/2}^{h/2} I(z'-z)\, dz'\right]^{-1/2}. \tag{3.6}$$

It is important to notice that we cannot expect total agreement between $v_{\mathrm{conv}}(z)$ and the measured velocity $v_{\mathrm{PIV}}(z)$. $v_{\mathrm{conv}}(z)$ is the weighted average of a theoretical profile, where the weighting function $I(z)$ is given by Eq. 3.4, and no base-clipping is considered. v_{PIV} is based on measured data after base-clipping, which reduces the signal from out-of-focus particles. Despite the base-clipping there still is some influence from the finite optical resolution, and we estimate it qualitatively by means of a convolution.

3.2.4 Results and discussion

As a first result, Fig. 3.3(a) contains a comparison of two experimental velocity profiles $v_{\mathrm{PIV}}(z)$ with the simple theoretical profile $v_{\mathrm{NS}}(z)$ for the suspension of beads in water. The zero values of the theoretical profile indicate the channel boundaries. As the profile is fitted to the maximum velocity, there is a fine agreement at the center, but some discrepancy when the boundaries are approached. Beyond the boundaries, an out-of-focus signal is picked up, a feature which is not captured at all by the simple theoretical profile. However, the effect is real: it is nicely reproduced in the two different experiments.

Using instead the convolved theoretical profile $v_{\mathrm{conv}}(z)$ from Eq. (3.5) we obtain the new profile seen in Fig. 3.3(b), where it is seen that the convolution with the visibility function yields a qualitatively correct description of the non-zero values at the channel boundaries. It furthermore explains both the increase in the observed velocities outside the channel, and the rapid increase in uncertainty.

Our measurements on the beads demonstrate that it is possible to resolve velocities normal to the focal plane with a focal depth of 4 μm using volume illuminated μPIV, averaged cross-correlation and base-clipping.

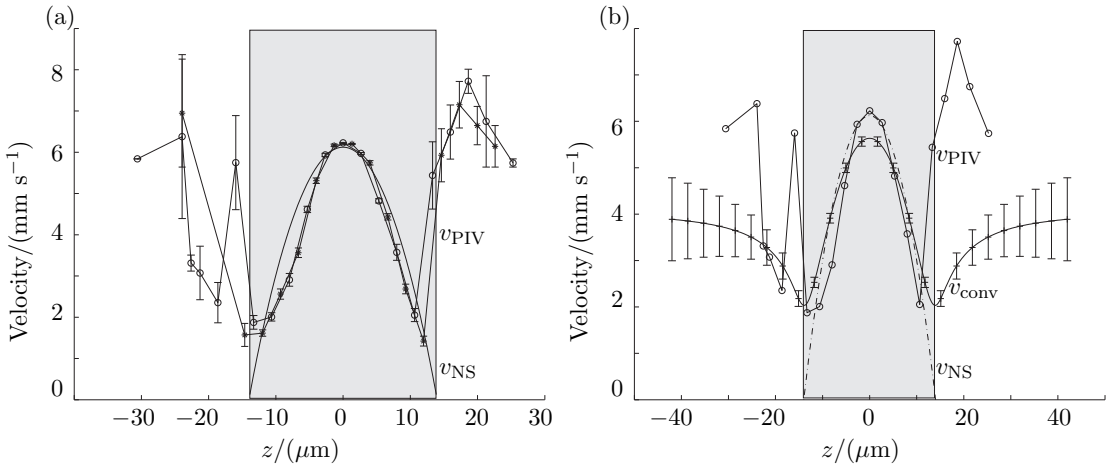

Figure 3.3: The velocity of the bead suspension versus z. (a) The z-axis has been centered around the middle of the channel. Legends: $(-\circ)$ first experiment v_{PIV}, $(-*)$ second experiment v_{PIV}, and $(-)$ Navier-Stokes theory $v_{\mathrm{NS}}(z)$. Experimental uncertainties are indicated with error bars. (b) The weighted theoretical profile $v_{\mathrm{conv}}(z)$ obtained from a convolution of the Navier Stokes profile $v_{\mathrm{NS}}(z)$ with the Lorentzian visibility function $I(z)$ of Eq. (3.4). Legends: $(-)$ theory $v_{\mathrm{conv}}(z)$, $(-\cdot)$ theory $v_{\mathrm{NS}}(z)$, and $(-\circ)$ first experiment v_{PIV}. Theoretical uncertainties are indicated with error bars. A fair qualitative agreement is achieved between experiment and theory.

We have seen that moving the focal plane outside the channel leads to an increase in observed velocities and to a steep increase in the associated uncertainties. This can be explained qualitatively as follows. When the focal plane and hence the maximum of the visibility function lies outside the channel, the observed average velocity increases because the high-velocity particles in the center of the channel are seen with the same (low) intensity as the low-velocity particles at the boundaries. Moreover, only very few particles are observed at all thus resulting in large $1/\sqrt{N}$-fluctuations and increased uncertainties.

For the blood measurements, the velocity profile is seen in Fig. 3.4(a) with the corresponding uncertainties. The uncertainty of a velocity measurement depends on the density of the moving refraction patterns (the image density) in the interrogation volume. For positions of the focal plane inside the blood-filled channel, the particle seeding is relatively high, and the uncertainties become correspondingly small. Even outside the channel the uncertainties are surprisingly small, but as in the case of the bead suspension they increase significantly as the focal plane is moved outside the channel. The first channel wall was positioned where the steepest increase in uncertainty was observed (bottom), and the second wall (top) was determined by the channel height.

Blood is known to develop cell free layers next to solid boundaries to lubricate the transport of a semi-solid plug consisting of cells[34], i.e., a two-phase system. The nearly flat velocity profile in Fig. 3.4(a) strongly suggests that such a two-phase model indeed is a good description of the system, whereas a single-phase model employing non-Newtonian viscosity data from bulk measurements does not fit the data. A two-phase model is seen in Fig. 3.4(b), where the velocity of the plug is 17 mm s^{-1}, and the cell free layer is a

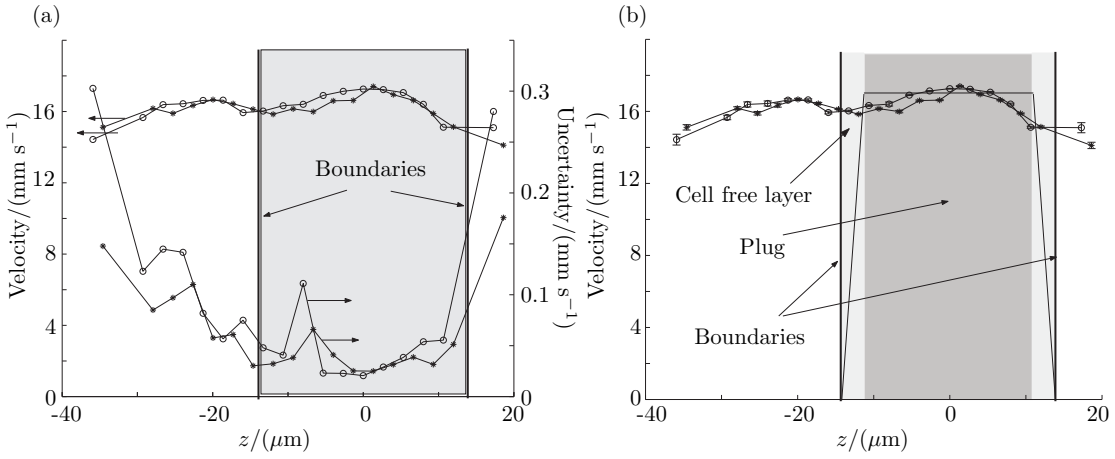

Figure 3.4: Measurements on blood flows. (a) The velocity (upper curves) and the uncertainty (lower curves) as a function of z. The z-axis has been centered around the middle of the channel. The channel boundaries (top and bottom) are indicated by vertical lines at $z = \pm 14$ μm. Legends: $(-\circ)$ first experiment, $(-*)$ second experiment. The uncertainty increases strongly outside the boundaries. (b) A comparison between the suggested two-phase model and the experimental results. Legends: $(-)$ two-phase model, $(-\circ)$ first experiment, $(-*)$ second experiment.

Newtonian liquid approximated with the viscosity of water. We can obtain an estimate of the width d of the cell-free layer by matching the nominal flow rate Q with the model. We find

$$d = 2\left(A - \frac{Q}{v_0}\right)\frac{1}{l}, \tag{3.7}$$

where $A = 1.09 \times 10^{-8}\mathrm{m}^2$ is the area of the channel, $v_0 = 17 \times 10^{-3}$ m s^{-1} is the plug velocity, and $l = 7.57 \times 10^{-4}$ m is the perimeter of the channel. The cell free layer was calculated to be $d = 3$ μm, which is 21% of the channel. In the literature it is reported that cell free layers in microtubes for diluted blood samples took up to about 10% of the volume[34]. Considering the increase in uncertainties and the fine agreement with the two-phase model, it is reasonable to assume that we have been able to resolve the velocities along the z-axis, and that we have observed a plug flow.

We have successfully measured steady state velocity profiles on suspensions of beads and human blood in a microchannel. The microflows were imaged through an optical system using pulsed back illumination. Due to the focal depth, the optical system limits the resolution vertical to the focal plane, which results in an averaging of velocities in adjacent planes.

In the blood suspension, we measured a velocity profile, which together with a two-phase model gives a strong indication of a plug flow. The fitting of a two-phase model resulted in a cell free layer of 3 μm.

We have hereby tested the technique, and found that it is suitable to obtain detailed information on complex fluids. However, in order to use PIV to measure the flow in more realistic microsystem, it will probably be necessary to switch the LED with a laser

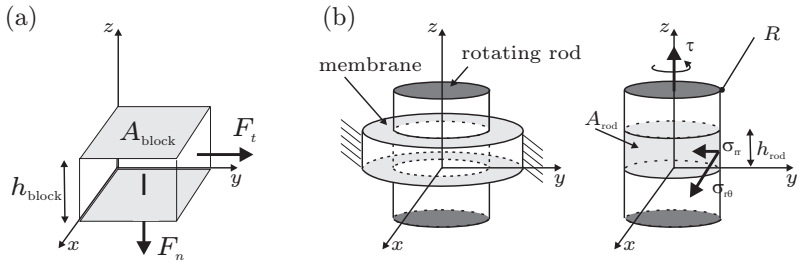

Figure 3.5: Illustration of energy savings by down scaling the contact area. (a) For a block with constant height h_{block} the friction energy is down-scaled with the area A_{block} due to a reduction of the normal force F_n. (b) For a rod rotating in a membrane an energy saving due to down scaling of A_{rod} is also obtained by a reduction of the normal force, i.e., the contact pressure σ_{rr} is constant. $\sigma_{r\theta}$ indicates the friction stress.

in order to get an adequate exposure. Also, many microsystems does not allow back illumination. In that case a setup with front illumination and epi-fluorescent beads, will be more suitable.

3.3 Theory of sealing and rubber friction

We will now leave the flow characterization, and return to mechanical issues relating to valve design. As we are optimizing pressure seals, with movable parts we are interested in both sealing and friction. The sealing capability is dependent on the contact pressure, and so is the friction. It is, therefore, necessary to understand the nature of both phenomenons, in order to balance the properties correctly. An example of modelling of a rectangular piston, sealed by an o-ring is presented by Nikas [35]. Although the model includes many important parameters as pressure and temperature, it appears difficult to extract the general knowledge from the model. Persson *et al.* have also developed a detailed sealing model, where surface roughness is taken into account, but also this model requires a significant effort to understand, and use for practical purposes [36].

The friction coefficient

The friction coefficient is defined as the ratio between the tangential force F_t and the normal force F_n acting on a sliding or static object

$$\eta = \frac{F_t}{F_n}. \tag{3.8}$$

The contact area A is not included explicitly in Eq. (3.8), and a general law is that the friction coefficient is independent of the area. This means that for a given load a small and a large block requires the same tangential force in order to slide.

Why friction scales with nominal area

Seeking an energy saving by scaling down the system, we have to reduce the normal force. We will now show how the energy is down scaled with the contact area, for the two systems

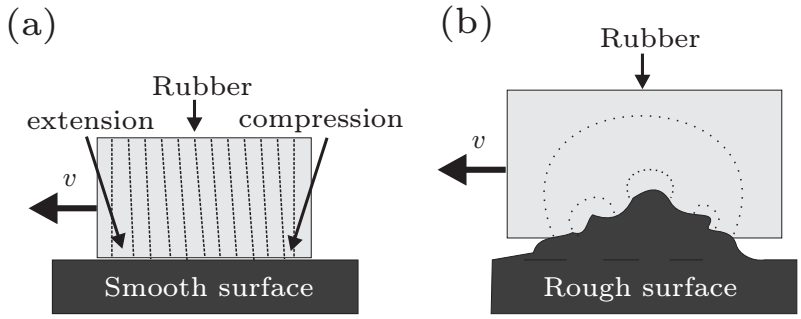

Figure 3.6: Illustration of friction processes. (a) Friction induced by adhesion forces on a smooth surface. See Ref. [37] for more details. (b) Friction induced by asperities on a rough surface. The volume of rubber (dashed line on figure) wherein the energy is dissipated is on the size of the asperity, i.e, the asperity length cubed. See Ref. [36] for more details.

sketched in Fig. 3.5. For a block with contact area A_{block}, height h_{block}, and density ρ, the sliding friction force is

$$F_{\text{fric}} = \eta\, \rho h_{\text{block}} A_{\text{block}}\, g, \tag{3.9}$$

where g is the gravitational acceleration and $g\rho h$ is an expression for the contact pressure. In this way we can reduce F_{fric} by down-scaling A. We shall later use a similar approach in reducing the actuation energy for rotating a rod supported by a compressive rubber matrix. To briefly discuss the idea, the torque for a rod with radius R and contact area $A_{\text{rod}} = 2\pi R h_{\text{rod}}$ is given by

$$\tau = \eta\, 2\pi R h_{\text{rod}}\, \sigma_{rr}\, R, \tag{3.10}$$

where σ_{rr} is the contact pressure, h is the hight of the contact area on the rod surface. If we for a constant pressure reduce the radius of the rod, the torque is decreased proportionally to R^2, which is very favorable.

The nature of rubber friction

In contrast to sliding between hard substrates, where friction is dominated by surface processes, rubber friction is governed by viscoelastic bulk properties.

There are two contributions to rubber friction [36], as illustrated in Fig. 3.6. On smooth surfaces as illustrated in panel (a), internal bulk friction is due to adhesive forces which induce surface oscillations by stick slip friction. A more detailed description of stick slip motion is given by Schallamach [37], where it is shown that the rubber surface moves in so-called waves of detachment. For rough surfaces, friction induced by the surface asperities will dominate. The asperities induces a viscous loss in the rubber, and the volume wherein energy is dissipated is defined by the size of the asperity [36]. The process is sketched in Fig. 3.6(b).

A clear evidence that friction is dominated by internal bulk friction, is proven by rubber sliding on a rough surface with a single length scale. If rubber is sliding with a velocity v on a surface with a roughness length scale l, friction is maximal, when the sliding frequency $f = v/l$ equals the frequency of maximum internal friction, Ref [36].

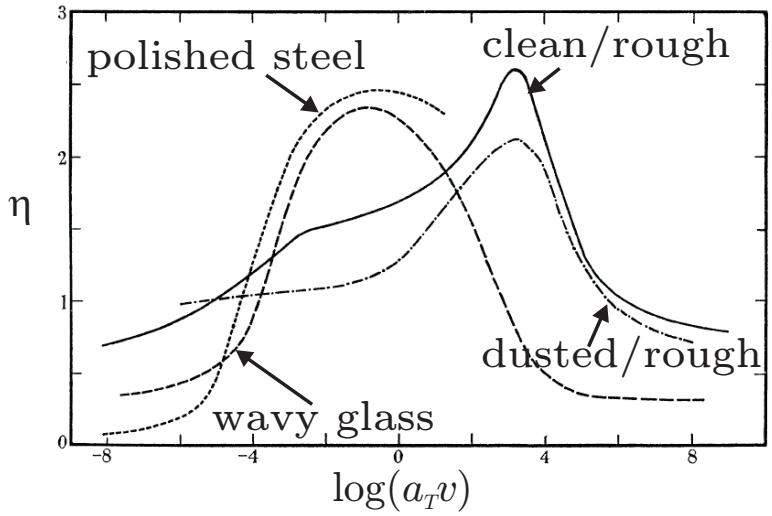

Figure 3.7: Master curve of the friction coefficient for acrylonitrile-butadiene rubber on four different surfaces at reference temperature $T = 20$ °C. The friction coefficient η is plotted as a function of $\log(a_T v)$, where $\log(a_T)$ is a temperature dependent parameter transforming data from the measurement to a reference temperature. Relabelled from Grosch, Ref. [38].

Whether the internal energy dissipation can contribute to the friction process is dependent on the glass transition temperature T_g. This is the temperature, where the viscosity of the polymer is 10^{12} Pas. If a polymer has a relatively high T_g, friction will be dominated of surface processes at room temperature, as the energy barrier for the polymers to flip between different conformation is too high. However, if the temperature increases bulk friction can also be significant for these materials, Ref [36].

Rubber friction: temperature and velocity dependence

The influence of temperature and velocity is not trivial, and according to data shown by Grosch [38] the friction coefficient shows a maximum with respect to velocity. Some of the results are shown in Fig. 3.7, which is a so-called called master curve. We will not go in detail with the theory due to its complexity, but we will just note that it can explain some general friction properties of different rubbers. Furthermore, Grosch describes a technique to perform measurements at low velocities and transform them to high velocity measurements by changing the temperature. High velocity measurements are in general difficult to interpret due to heat generation between the sliding surfaces. For more information on the master curve, a simplified explanation is given in Ref. [39].

Due to heat generation in the interface for high sliding velocities, the velocity for maximum friction is shifted to lower velocities than predicted by low velocity measurements, which subsequently has been transformed to high velocity measurements. Calculations including this so-called flash temperature is in better agreement with direct measurements of the friction, as described in Ref. [36].

Rubber friction: nominal area, area of real contact, friction at zero load
The friction coefficient is almost independent of load [36]. Therefore the friction coefficient depends linearly on the normal force, as already stated in Eq. (3.8). This dependency is due to an increase in the area of real contact A_{rc}. In theory of friction it is necessary to distinguish between this area and the apparent nominal area A_{an}. The former is the area which we observe without magnification, and the area of real contact is the interface between asperities of the surfaces in contact. The dependency on area of real contact was investigated by Schallamach [40], and more detailed models have been applied later, but with approximately the same conclusion. These models are reviewed by Persson *et al.*[36]. There is an upper and lower limit for the linearity between normal force and friction. For very small loads, adhesional forces between the soft rubber and substrate is significant, and the friction does, therefore, not approach zero for at the zero-load limit. At the upper limit the area of real contact cannot exceed the apparent area [36], and the linearity cease to be valid.

Despite the fact that a model for quantitative calculations of the friction coefficient between rubber and a hard substrate exists [36], it is not a model we have utilized in this work. The model requires detailed knowledge on the surface roughness on all length scales, and viscoelastic properties of the rubber. Therefore, the model has been considered out of the scope for this thesis.

In this work we are interested in lowering the frictional forces, and we shall, therefore, take a closer look on such optimization possibilities.

Optimization by reduction of friction coefficient
On smooth surfaces the friction coefficient can be reduced by lowering the interfacial energy between the rubber and the hard substrate. This can for example be effectuated by magnesium powder at the interface, Ref. [38], or using a rubber mold which ensures molecules with a low interfacial energy at the contact surface. Molds with low surface energies allow molecules also with low surface energy at the surface. Analogous, molds with high surface energy (polar groups) results in a high concentration of nitrile groups at the surface, and they have a higher surface energy. In the example reviewed by Persson [39], the friction coefficient is reduced a factor of 4. This reduction is obtained, if we go from a system where rubber with a high surface energy is sliding on aluminum to a system where rubber with a low surface energy is sliding on teflon. Here, a second effect is that teflon has a lower surface energy than aluminum.

It was also noticed that the friction coefficient had a maximum with respect to velocity and temperature. As an example, the data on friction coefficients presented by Grosch [38] show a factor of ten as the maximum difference between minimum and maximum values for sliding on a smooth surface. If we consider rough surfaces, the friction coefficient is generally a little smaller. To get an impression of the variations of the friction coefficient for a test between a specific rubber and a smooth surface, the maximum difference is a factor five, where only temperature (or equivalent velocity) has been varied.

As friction is due to viscous losses in the bulk material, the choice of rubber compound, and contamination with different particles, could have an effect by either reducing the friction coefficient or moving the peak observed in the master curve.

For friction between hard substrates, lubrication is often used to minimize the energy to slide. For rubber friction this will have a minor effect, as it is not a surface process. However, if the lubricant can change the interfacial energy, as in the case of the magnesium powder, some effect may be observed.

Optimization by reduction of normal force
In a first approach, we expect that optimization is easier to obtain by decreasing the normal force by decreasing the system, than by decreasing the friction coefficient. In that way we keep a constant contact pressure, and that is important when we for example are optimizing a seal, which should sustain a certain liquid pressure. Reduction of the friction coefficient is a second possibility, which can be considered, if down scaling of the system is insufficient or impossible.

3.4 Summary

We have in this chapter discussed some basic equations and measures to analyze and characterize a fluid flow, in a given flow geometry. In addition, we have presented results where the flow velocity field is measured directly using μPIV. In particular, this can be a valuable tool in studies of complex geometries or fluids. As a last topic, we have briefly reviewed the nature of friction, why we obtain energy savings by down-scaling, and how friction can be reduced by reducing the friction coefficient. In the next chapter we will proceed with the establishment of two models to study sealing properties and sliding friction in silicone based microchannels. These models will later be used for characterization of the turning valves.

Chapter 4

Modeling of sealing and friction

In this chapter we shall be concerned with the basic properties of a valve, where the switching between open and closed state involves friction between rubber and a smooth hard surface. These properties are the ability to sustain the liquid pressure, and the ability to easily slide between open and closed states. Therefore we need to study the basics of sealing and friction properties. In this particular case we will investigate the properties of an elastic silicone rubber, and a rigid smooth steel surface.

Friction forces determines how much energy we will need to operate or actuate the valve, and it is our desire to minimize the actuation energy. Like sealing properties, friction forces are dependent on the contact pressure, and there appears to be a conflict in obtaining an energy efficient valve with good sealing properties, which is our goal. In other words, we desire a valve with a high contact pressure to sustain high pressures in the liquid, and a low friction force to minimize the actuation energy.

The most important property of a seal is the threshold pressure, which is the maximum pressure before leakage. The strength of the seal will depend on the contact pressure between the elastic and rigid material, but also on how the contact pressure distributes when the liquid pressure increases. We shall in the following study and model a simple plug-seal consisting of a rigid plug confined by a flexible tube. This will be referred to as the plug-sealing model, and in Chapter 5 we will compare the results with measurements utilizing the so-called plug-sealing geometry. We will use the model to study the threshold pressure and the relation between pressure and leakage flow rate.

After the sealing study we continue to study the scaling of friction. How does friction depend on contact forces, contact area, and sliding velocity. We shall use the so-called torque model to study the friction forces dependency on contact forces and area. The models will be explained in detail in this chapter, and will be compared to measurements in Chapter 5. The special developed test geometries are similarly referred to as the torque geometries.

As we in Chapter 5 shall be concerned with tubes and membranes with specific geometries, we will use their parameters for numerical calculations in this chapter. In this way we

estimate the feasibility of approximations, which to a higher degree reveals the importance of different parameters. Parameters for tubes and membranes are listed in Table 4.1.

Geometry	Inner diameter [μm]	Outer diameter [μm]	Young's modulus E [MPa]
Small bore tube	260	2090	2.4
Large bore tube	520	3720	2.4
Small memb. hole	320	10^4	3.7
Large memb. hole	640	10^4	3.7

Table 4.1: Parameters of tubes and membranes for numerical calculations. Poisson's ratio $\sigma = 0.49$ as rubber is incompressible. The parameters corresponds to geometries in Chapter 5, but are also included here for the readability of the thesis.

4.1 Sealing and threshold pressure

As mentioned, we will establish a simple model to study sealing properties using the plug-sealing model. Fig. 4.1 is a sketch of the processes in creating and breaking a seal. In panel (a) we have an elastic tube with inner and outer radius r_1 and r_2, respectively. In panel (b) a plug with radius R_1 is inserted in the region between z_1 and z_2. As $R_1 > r_1$ the plug exerts a uniform pressure on the tube, and the inner wall is displaced with u_1. In panel (c) the inlet pressure Δp increases and breaks the seal, and this pressure will be referred to as the threshold pressure p_{th}. We shall derive a simple expression to estimate p_{th}, and how it depends on the deformation u_1/r_1 and the rod length ℓ_1.

Classical theory of elasticity involving the pressure induced expansion of a tube, predicts that the radial displacement u_r is given by

$$u_r = C_1 r + \frac{C_2}{r}, \tag{4.1}$$

see Ref. [41]. For the boundary conditions

$$\sigma_{rr}(r_1) = -p, \tag{4.2a}$$
$$\sigma_{rr}(r_2) = 0 \tag{4.2b}$$

we get the integration constants

$$C_1 = \frac{p r_1^2}{2(\lambda_1 + \lambda_2)(r_2^2 - r_1^2)}, \tag{4.3a}$$
$$C_2 = \frac{p r_1^2 r_2^2}{2\lambda_2 (r_2^2 - r_1^2)}. \tag{4.3b}$$

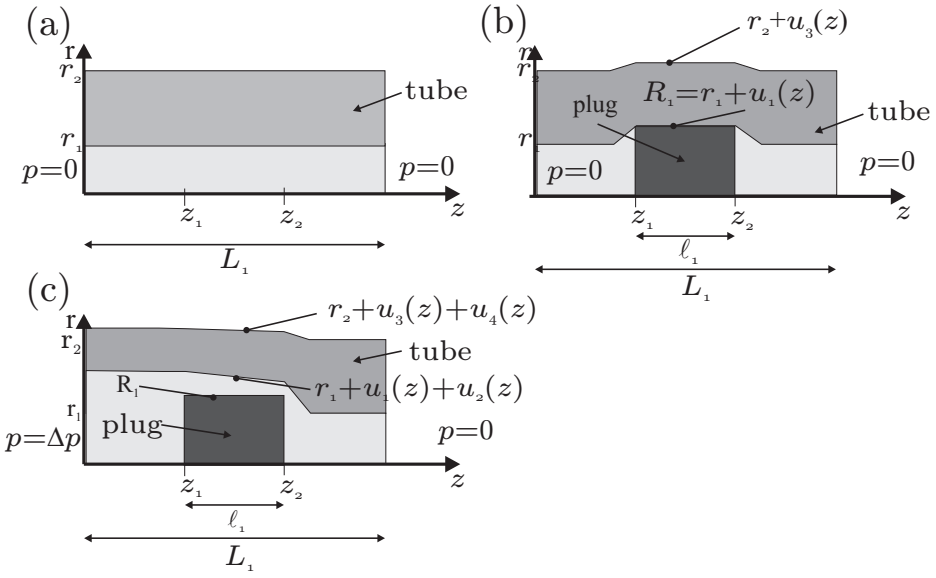

Figure 4.1: Sketch of plug-sealing model, dimensions are not to scale. (a) An elastic silicone tube with length L. The inner and outer radius is denoted with r_1 and r_2, respectively. The pressure p is zero at inlet and outlet of the tube. (b) A plug is inserted with length ℓ_1 and radius R_1. z_1 and z_2 indicates right and left plug edge. When the plug is inserted, the inner tube wall is displaced with $u_1(z)$, and the outer tube wall is displaced with $u_3(z)$. (c) The inlet pressure is increased and deforms the tube. The inner and outer walls are additionally displaced with $u_2(z)$ and u_4, respectively. In panel (c) the pressure drop Δp, has exceeded the threshold pressure, and the seal is leaking.

The material constants are given by

$$\lambda_1 = \frac{\sigma E}{(1+\sigma)(1-2\sigma)}, \tag{4.4a}$$

$$\lambda_2 = \frac{E}{2(1+\sigma)}, \tag{4.4b}$$

where E and σ are Young's modulus, and Poisson's ratio, respectively. Using Eq. (4.1) with the integration constants Eqs. (4.3a) and (4.3b) at $u_r = u_1$ we get

$$p = \frac{2\lambda_2(\lambda_1+\lambda_2)(r_2^2-r_1^2)}{r_1^2\lambda_2 + r_2^2(\lambda_1+\lambda_2)} \frac{u_1}{r_1}. \tag{4.5}$$

or

$$p = k_e \frac{u_1}{r_1}, \text{ with the spring constant or elastic modulus} \tag{4.6a}$$

$$k_e = \frac{2\lambda_2(\lambda_1+\lambda_2)(r_2^2-r_1^2)}{r_1^2\lambda_2 + r_2^2(\lambda_1+\lambda_2)}. \tag{4.6b}$$

If liquid shall pass the seal, the liquid pressure Δp has to exceed the pressure between the elastic and rigid material $\Delta p > p$, i.e., for a system where the sealing pressure depends

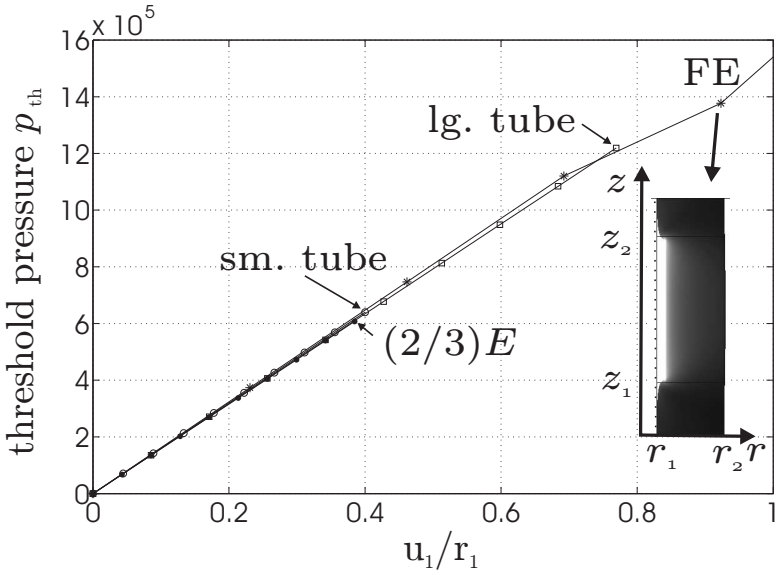

Figure 4.2: Modelled threshold pressure. "$\circ$" small bore tube analytical solution, "$\square$" large bore tube analytical solution, "$*$" small bore tube finite element (FE) solution, "$\bullet$" the $k_e = (2/3)\,E$ approximation. For both tubes the the deviation from the approximation is less than 1%. The analytical and the FE-simulation are coinciding, and confirms the validity of the analytical solution. Small bore tube: $E = 2.4$ MPa, $r_1 = 130$ μm, $r_2 = 1045$ μm. Large bore tube: $E = 2.4$ MPa, $r_1 = 260$ μm, $r_2 = 1860$ μm. Parameters are also listed in Table 4.1.

elastic deformation only, the threshold pressure p_{th} is defined as Eq. (4.6a) with

$$p_{\text{th}} = p. \tag{4.7}$$

For incompressible rubber tubes, where the relative width $(r_2 - r_1)/r_1$ is large, it can be shown that $k_e = (2/3)\,E$. See Ref. [41] for a more detailed discussion of approximations to the solution.

Fig. 4.2 shows the variation of threshold pressure for the tubes in Table 4.1, which is dependent on the deformation u_1, and the two radii r_1 and r_2. The figure shows the threshold pressure as a function of the relative displacement u_1/r_1. For the chosen example the result approaches the $k_e = (2/3)\,E$-limit. On the figure is also shown a finite element simulation on the small bore tube, which coincides with the analytical solution. The deviation from the $k_e = (2/3)E$-approximation is 1%. As we shall see in Chapter 5, the simple analytical solution Eq. (4.6a) does not fit exactly, and we shall, therefore, apply the empirical expression

$$p_{\text{th}} = k_c\, k_e \frac{u_1}{r_1} + p_0, \tag{4.8}$$

where k_c is a correction factor and p_0 is the residual pressure, when the deformation related pressure is zero. The residual pressure has its origin in adhesional forces and boundary uncertainties.

4.2 Sealing and leakage

When the liquid pressure Δp exceeds p_{th}, the tube is displaced with $u_2(z)$, and a leakage is induced around the plug. We will now establish a model to describe this phenomenon, by coupling the mechanical equations for deflection of the tube wall and the hydrodynamic equations for the liquid flow. Due to a viscous pressure loss the pressure will decrease in the flow direction, and we have a z-dependent pressure given by

$$p = k_c\, k_e \left(\frac{u_1 + u_2(z)}{r_1} \right) + p_0, \tag{4.9}$$

which on a differential form reduces to

$$dp(z) = \frac{k_c\, k_e}{r_1}\, du_2(z). \tag{4.10}$$

For a slit flow in the axial direction, and with the width corresponding to the circumference of the plug, we can write the differential hydraulic equation

$$dp(z) = -\frac{6\mu dz}{\pi R_1 u_2^3} Q, \tag{4.11}$$

where Q is the unknown flow rate. This is a valid approximation, when we have small Reynolds numbers, and if the change of channel height $du_2(z)/dz$ is moderate. This is the so-called lubrication approximation, and a detailed description can be found in [42]. From Eqs. (4.10) and (4.11) and a separation of the variables we get the expression

$$u_2 = (-\alpha z + \beta)^{\frac{1}{4}} \quad \text{, with} \tag{4.12a}$$

$$\alpha = -\frac{24\mu Q}{\pi R_1 r_1^3 k_c\, k_e} \tag{4.12b}$$

where β is an integration constant. Q and, thereby, α is also unknown, and we, therefore, require two boundary conditions

$$\Delta p = k_c\, k_e \left(\frac{u_1 + u_2(z_1)}{r_1} \right) + p_0 \quad \text{for } z = z_1, \text{ and} \tag{4.13a}$$

$$\epsilon \Delta p = k_c\, k_e \left(\frac{u_1 + u_2(z_2)}{r_1} \right) + p_0 \quad \text{for } z = z_2 \tag{4.13b}$$

to solve the equations. As the deflection $u_2(z_1) > u_2(z_2)$, we must require $0 < \epsilon < 1$. Solving Eq. (4.12a) with the boundary conditions Eqs. (4.13a) and (4.13b), we find

$$\beta = \left(\frac{\Delta p - p_0}{k_c\, k_e} - \frac{u_1}{r_1} \right)^4 + \alpha z_1 \quad \text{, and} \tag{4.14a}$$

$$\alpha = \frac{1}{z_2 - z_1} \left[\left(\frac{\Delta p - p_0}{k_c\, k_e} - \frac{u_1}{r_1} \right)^4 - \left(\frac{\epsilon \Delta p - p_0}{k_c\, k_e} - \frac{u_1}{r_1} \right)^4 \right] \tag{4.14b}$$

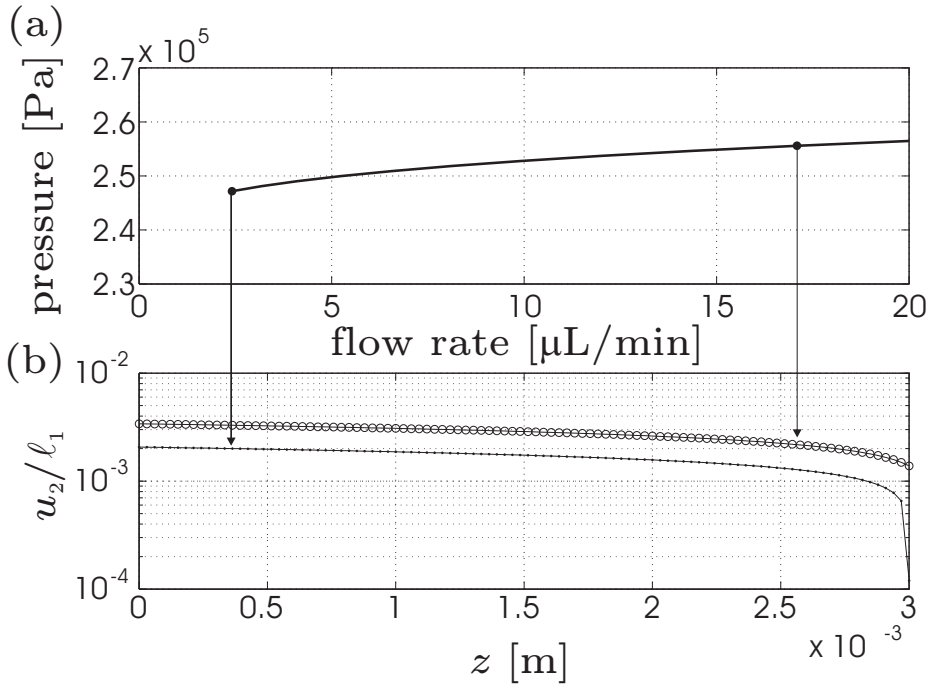

Figure 4.3: Leakage results from plug-sealing model. (a) pressure vs flowrate using Eq. (4.15). "•" indicate data points where $u_2(z)$ has been evaluated. These profiles are represented in (b). (b) u_2/ℓ_1 vs z calculated using Eq. (4.12a), Eqs. (4.14a) and (4.14b). For the lubrication approximation to be valid the change of u_2 compared to the change of z must be small. It is noticed that the approximation is becoming more questionable at small pressures, and in the proximity of the right boundary (there appears to be large changes in u_2). However, u_2 is small compared to ℓ_1, and the approximation is therefore reasonable. Parameters: $r_1 = 260$ μm, $R_1 = 295$ μm, $k_c k_e = 0.55$ MPa, $p_0 = 0.16$ MPa, $\ell_1 = 3$ mm, $\mu = 1$ mPa s, $\epsilon = 0.95$.

We can now calculate the flow Q from Eq. (4.12b)

$$Q = \frac{\pi}{24\mu}\frac{u_1 r_1^3 k_c\, k_e}{z_2 - z_1}\left[\left(\frac{\Delta p - p_0}{k_c\, k_e} - \frac{u_1}{r_1}\right)^4 - \left(\frac{\epsilon\Delta p - p_0}{k_c\, k_e} - \frac{u_1}{r_1}\right)^4\right]. \tag{4.15}$$

A second requirement for a positive flow rate is $u_2(z_2) > 0$, and consequently $\Delta p > (k_c\, k_e\, u_1)/(\epsilon\, r_1)$. This implies that we do not obtain zero flow rates, as we will see later when we evaluate Eq. (4.15).

Fig. 4.3 shows results from the sealing model. Panel (a) shows the pressure vs flow rate using Eq. (4.15). "•" represents data points where $u_2(z)$ has been evaluated, and this profile is represented in panel (b). The ϵ value represent the pressure drop along the plug, and in this case, with $\epsilon = 0.95$, 5% of the pressure is lost. The exact ϵ-value should be found by fitting to experimental data, as we will do later. Panel (b) shows u_2/ℓ_1 vs z, and the displacement is calculated using Eq. (4.12a), Eqs. (4.14a) and (4.14b). Note the semi-logarithmic scale. For the lubrication approximation to be valid the change of

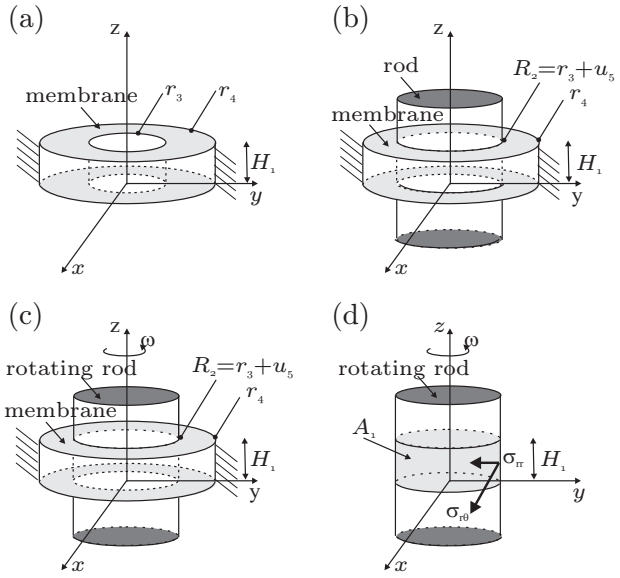

Figure 4.4: Sketch of torque model: the three steps to model the forces on a rotating rod, which is pierced through a rubber membrane hole. Dimensions are not to scale. (a) A membrane ring with height H_1, and inner and outer radius r_3 and r_4, respectively. The membrane is free to expand at the outer radius. (b) a rod is inserted and the inner ring wall is displaced with u_5. (c) The rod rotates with angular velocity ω. (d) Illustration of friction stress $\sigma_{r\theta}$, and normal pressure σ_{rr}. Light gray indicates the nominal contact area A_1 between silicone rubber and steel.

u_2 compared to the change of z must be small. It is noticed that the approximation is becoming more questionable at small pressures, and in the proximity of the right boundary. However, u_2 is small compared to ℓ_1, and the approximation is therefore reasonable. All parameters are listed in the figure caption.

4.3 Friction

In analogy to the sealing model, we establish a model describing the largest contributions to friction, and, thereby, the actuation energy. Friction is dependent on the product of the normal forces and a friction coefficient. The friction coefficient is an empiric parameter, which primarily is dependent on bulk properties of the rubber, surface roughness, and surface energy between the sliding objects. See the discussion in Section 3.3. The normal force is dependent on the deflection of the flexible membrane.

Fig. 4.4 is a sketch of the torque model. Panel (a) shows the membrane ring with height H_1, and inner and outer radius r_3 and r_4, respectively. In panel (b) a rigid rod with radius R_2 is inserted and induces the displacement u_5, and in panel (c) the rod rotates with an angular velocity ω and a torque τ. The torque is mainly determined by friction forces acting on the surface. Panel (d) shows the normal pressure σ_{rr}, and the friction stress $\sigma_{r\theta}$ acting on the contact area, the nominal contact area is indicated with light gray.

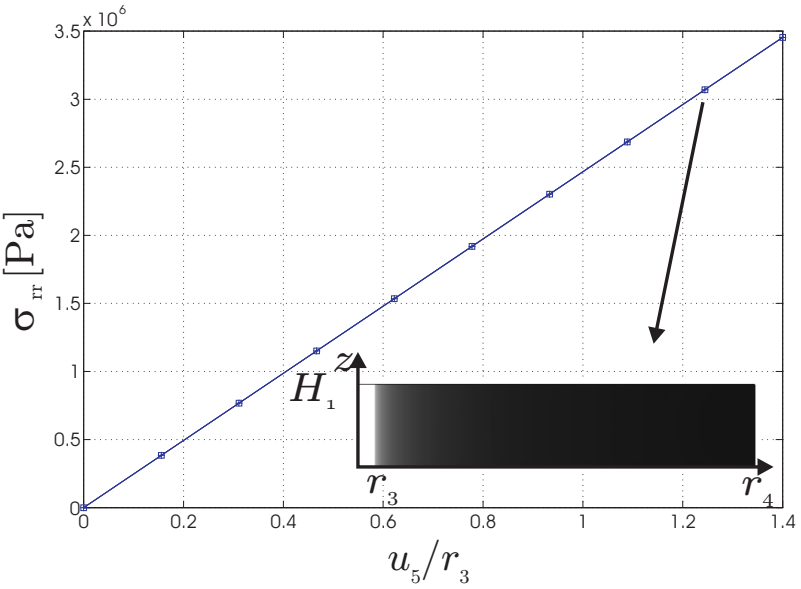

Figure 4.5: Contact pressure results from torque model. Finite element (FE) simulation of pressure σ_{rr} as a function of the displacement u_5/r_3. Two FE simulations are defined by "$\cdot$" $r_3 = 160$ μm, $r_4 = 5000$ mm; "$\circ$" $r_3 = 320$ μm, $r_4 = 5000$ mm. "$\square$" solution approximated with $k_e = 2/3\,E$. In all cases $E = 3.7$ Pa. The FE solution is seen to coincide with the approximate solution. The insert shows the solution of axisymmetric FE simulation of the total displacement for the small membrane hole. The result is corresponding to the data point indicated with an arrow. The solution shows that the main deformation is in the proximity of r_3, and boundary conditions on r_4 has little influence. Parameters are also listed in Table 4.1, and corresponds to membranes used in Chapter 5.

Fig. 4.5 shows two finite element solutions (FE) of the relation between σ_{rr} and u_5/r_3. The used membrane parameters are listed in Table 4.1. On the figure is also shown the $k_e = (2/3)\,E$ approximation, which coincides with the other solutions. In this case it is, therefore, very reasonable to use the approximate solution.

As for the plug model, we shall use an empirical equation to calculate the contact pressure σ_{rr}

$$\sigma_{rr} = k_c\, k_e \frac{u_5}{r_3} + p_0. \tag{4.16}$$

With the friction coefficient η we can calculate the friction stress $\sigma_{r\theta}$.

$$\sigma_{r\theta} = \eta\, \sigma_{rr}. \tag{4.17}$$

We have now investigated the plug-sealing model and the torque model, and verified some simple equations applying to the geometries (see, Table 4.1), which are to be used in Chapter 5. The plug-sealing model also allows us to analyze a plug-sealing geometry, after the seal has been broken.

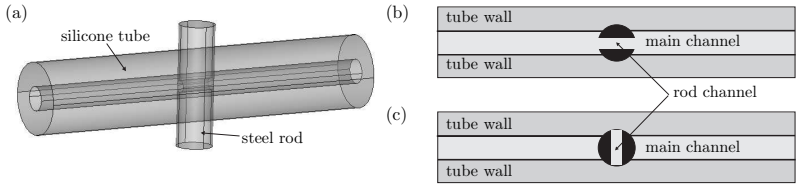

Figure 4.6: (a) Sketch of principles of a turning valve with silicone walls and a steel rod. (b) The open state: the rod channel is parallel to the main channel. (c) The closed state: the rod channel is perpendicular to the main channel.

4.4 Sealing and friction in a turning valve

The two simple models, will be used to characterize a turning valve constructed in a comparable way. The principles of such a turning valve is sketched in Fig. 4.6. The sealing effect in the turning valve is, as the plug-seal, dependent on the contact pressure. However, when a pressure increases for the valve in its closed state Fig. 4.6(c), the valve will to some degree be self-sealing, i.e., the liquid pressure increases the contact pressure on the down-stream contact surfaces. This geometrical effect is not featured by the plug-sealing model and we, therefore, have a minimum threshold pressure given by

$$p_{\text{th}}^{\min} = k_m \frac{u_1}{r_1} + p_0, \tag{4.18}$$

where r_1 corresponds to the radius of a channel seat containing the rod. The rod is slightly larger than the channel seat, and induces a displacement corresponding to u_1 of the plug-sealing geometry. k_m is an elastic module, but as the geometry is more complex, we have not derived an analytical expression. k_m is therefore an empirical module derived by comparison with measurements. Similar, an empiric equation for the contact pressure and the friction stress can be obtained

$$\sigma_{rr} = k_m \frac{u_5}{r_3} + p_0, \tag{4.19a}$$

$$\sigma_{r\theta} = \eta\, \sigma_{rr}. \tag{4.19b}$$

A benchmark value for a turning valve is the energy used to open and close the valve, we shall refer to this energy as the actuation energy

$$E_{\text{act}} = \pi\tau, \tag{4.20}$$

where τ is the dynamic frictional torque, and π is the turned angle in radians (the sum of two quarter-turns).

4.5 Summary

We have in this chapter discussed the plug-sealing model, which is to be used for studies of sealing properties in a plug-seal. In the same way, we established the torque model to show

sliding friction depends on contact area, and contact force. Due to the close similarity to how a turning valve works, the models serve as a basis for valve characterization. In the next chapter we conduct various experiments on sealing and friction. In particular, we study geometries corresponding to the established models.

Chapter 5

Experiments on sealing and friction

In this chapter we shall experimentally investigate results from Chapter 4, and investigate the properties of sealing and friction further.

We start out with the sealing experiments that are conducted with the so-called flow setup, wherein different flow components can be studied. A flow component is a unit which in some way conducts liquid, and in this chapter we shall be concerned with components to calibrate the setup, and components to test basic properties. These are referred to as standard components and test geometries. In Chapter 6 the flow components will be different types of turning valves, and we talk about test for characterization purposes, rather than tests to study basic properties.

For friction we have several setups, namely, the balance based torque setup, the motor based torque setup, the so-called tribo test setup, and the pull-force setup. The balance based torque setup is used for friction studies at low velocities, and enables the use of geometries which resemble the basic geometry in a turning rod valve. In analogy to the flow experiment, we refer to these mechanical components as geometries. In both torque setups, we use the so-called torque geometry, but the motor based torque setup utilizes studies at high velocities. Both setups are established especially for this project, as we did not find suitable commercial torque testers, with the ability to measure a torque below 1 mN m. The tribo test setup is a standard setup, to study friction coefficients between two solid materials. The method implies the rotation of a test specimen, for a given load, on a stationary surface. We refer to the test specimen as a ring geometry. The pull-force setup is a commercial tensile test bench, where the pull-force geometry, has been inserted. This test is performed to study the similarities between rotational and translational sliding friction.

List of setups and geometries

- Sealing test. A flow setup using the standard flow components, the plug-sealing geometries, and other flow components, e.g., valves.

- Low-speed torque test. A balance based torque setup using the torque geometries
- High-speed torque test. A motor based torque setup using the the torque geometries
- Tribo test. A tribo test setup using the ring geometries
- Pull-force test. A pull-force setup using the pull-force geometries

5.1 Equipment

The following is a compact list of equipment, used in the experimental work. The list does not contain all the used equipment, as some of it is described on more appropriate places in the report. However, the list contains some details that have relevance to understand how the results are obtained, and to calculate various flow properties.

Pressure transducer
Honneywell pressure transducer 40PC0100G1A. Pressure range: 0 to 100 psi (6.9×10^5 Pa).

Syringe pump
KDScifentific syringe pump (KDS200). Nominal linear force: 40lb (178 N). With an 14.6 mm syringe the maximum pressure is 1.2 MPa. RS232 communication port. Flow rate 0.001 μL h^{-1} to 20.91 mL min^{-1}, depending on syringe.

Balance
Mettler Toledo balance (Ax105 DeltaRange). Readability 0.01 mg. RS232 communication port.

PC
IBM Thinkpad T41 with a PCMCIA slot and three serial ports for RS232 communication. LabView program to control the pump and data acquisition.

Data acquisition
PCMCIA-card (DAQCard-6062E).

Syringe, inlet and outlet tubing
Kloehn [43] glass syringe: volume 10 mL, piston diameter 14.6 mm. All tubings are in polyetheretherketone (PEEK). Inlet tubing before pressure sensor: length 51 mm, diameter 1.0 mm. Inlet tubing after pressure sensor: length 85 mm, diameter 1.0 mm. Outlet tubing: length 306 mm, diameter 1 mm. Pressure sensor unit, swept volume: length 15 mm, diameter 0.5 mm. Pressure sensor unit, dead volume: length 25 mm, diameter 1 mm. The flow units are connected with different low pressure fittings from Upchurch [44].

LabView program for flow setup
A LabView program was programmed to control the pump and acquire data. Acquired

data: sample rate, pressure, mass on balance, and pumped flow rate, . In general, a LabView program consists of a front panel and a block diagram. The front panel corresponds to the instrument panel, whereas the block diagram is the actual program code. In the front panel of this program the user specifies the desired flow rate, and a filename where the acquired data is stored. The flow rate can be adjusted during a measurement.

LabView program for torque setup
The LabView program for the Torque setup consisted of data acquisition only. Acquired data: sample rate, mass on balance.

Motors, gears, and control electronics
Fast motor with small torque, and encoder to enable PID-regulation: Maxon DC motor, RE 13, diameter 13 mm, graphite brushes, 3 Watt, max. continuous torque 3.13 mN m, max. permissible speed 1.6×10^4 rpm, order number 118621. Encoder: Digital MR encoder, order number 228444.

Motor with reduction gear to provide low speed, and encoder to enable PID-control: Maxon DC motor, A-max 16, diameter 16 mm, precious metalbrushes CLL, 1.2 Watt, max. continuous torque 2.24 mN m, max. permissible speed 7.6×10^3 rpm, order number 110057. Gear: Spur gearhead GS 16 K, reduction 3101, max. efficiency 48 %, order number 201473. This combination of gear and motor provide a max. continuous torque of 3.3 N m, and a max. permissible speed 2.4 rpm. Encoder: Digital MR encoder, order number 228182. Control electronics: For both motors were used an EPOS 24/1 for DC motors (Maxon) with and RS232 interface, the application software allowed torque, velocity, and position control. A small memory buffer on the control unit allowed data acquisition with a high sample rate.

Silicone material and stainless steel
Plug-sealing geometry: Measured parameters for silicone tubes and steel plugs are listed in Tables 5.3 and 5.4. Torque geometry: Measured parameters for silicone membranes and steel rods are listed in Tables 5.5 and 5.6. Tribo test with rubber ring geometry: Measured parameters for rubber rings and steel surfaces are seen in Table A.2. Pull-force geometry: Measured parameters on silicone tubes and steel rods are seen in Table 5.8. Measurements of the mechanical properties of the different rubbers are listed in Table A.1.

5.2 Flow setup

First, we will describe and verify performance of the flow setup. To conduct flow measurements the described equipment, were arranged according to the sketch shown in Fig. 5.1. A syringe pump forces liquid into the system at a constant flow rate, and a pressure sensor measures the dynamic pressure upstream to the flow component. Inlet flow rates are given by the pump, and the outlet flow rates are measured on the balance, and, for steady state measurements without leakage, the two properties should be equal.

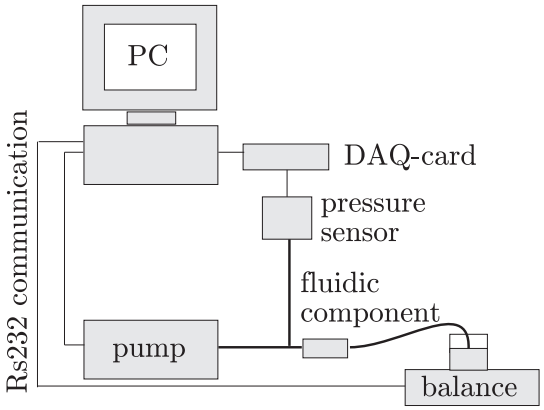

Figure 5.1: Sketch of flow setup. On the PC it is possible to set the flow rate, while primary data is collected via the RS232 interface. This setup was used for all flow measurements involving plug-sealing test-geometries, and characterization of valves.

LabView program
Fig. 5.2 shows a flow chart of the LabView program that controls the experiment. As a fairly large sampling period is allowed for steady state measurements, the pump control and data acquisition is executed in a sequential manner, and communication is enabled via the RS232 interface. At the end of each acquisition loop, data is written to a data file. The measured data mass on balance m_{bal} and pressure p are sampled within the *while loop*. The time t_0 is used to calculate the sample period, which is approximately 5 s. Intermediate times t_1, t_2, and t_3, provides information on the duration between different acquisitions, for example the time between read-out from the balance and the pressure sensor.

Hydraulic resistance of connecting tubes and standard components
To measure hydraulic resistance of a flow component, we need to consider the dimensions of the connecting tubing. Table 5.1 shows some important properties for this setup. It is necessary that the hydraulic resistance of the inlet and outlet tubes are magnitudes smaller than the flow component to be measured. Therefore, the expected hydraulic resistance of a flow component should be compared with values in this table, before any experiment. Another practical measure is the fill time, as it indicates, when we can expect the system to be primed at a given flow rate.

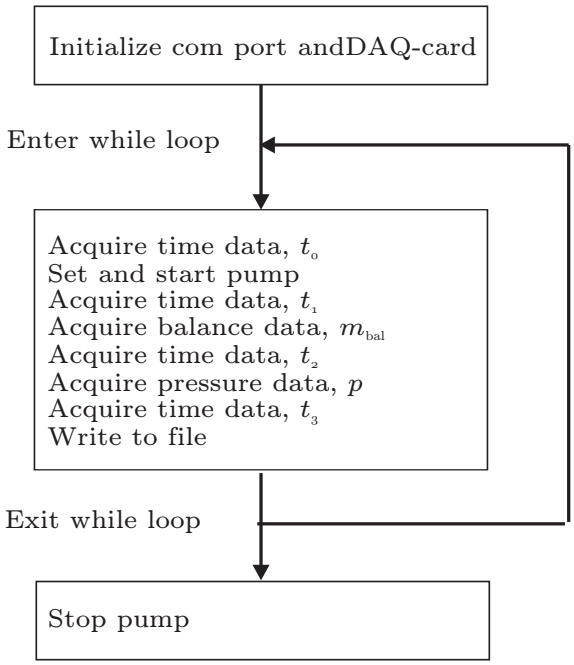

Figure 5.2: Flow chart to illustrate execution of LabView program used in flow setup.

Unit	Hydraulic resistance, swept volume Pa s m^{-3}	Swept volume m^3	Dead volume m^3	Fill time, swept volume min
Syringe	1.7×10^5	10^{-5}	0	2000*
Inlet before sensor unit	6.5×10^9	4.0×10^{-8}	0	8
Sensor unit	3.1×10^{10}	3.0×10^{-9}	2.0×10^{-8}	0.6
Inlet after senor unit	1.1×10^{10}	6.7×10^{-8}	0	13.4
Outlet	3.9×10^{10}	2.4×10^{-7}	0	48.1

Table 5.1: Time scales and hydraulic resistances in the flow setup. For calculation of fill time is used $Q_{\text{pump}} = 5\ \mu\text{L min}^{-1}$, which is a flow rate for a typical experiment. The fill time is a measure used during measurements, as it is necessary to know when the different components are primed. Hydraulic resistances in the connecting tubing must be magnitudes smaller than the tested flow component. * time to empty syringe.

To calibrate the flow setup, we used cylindrical PEEK tubes with a well defined geometry. The dimensions of the components are listed in Table 5.2, and are named Std. 1, Std. 2, and Std 3. Their hydraulic resistance increases with the label number, and are three order of magnitudes larger than corresponding values of the connecting tubes.

Component	Inner diameter 10^{-6} m	Length 10^{-3} m	Hydraulic resistance 10^{13} Pa s m^{-3}
Std. 1	101.6 ± 10	91.2 ± 0.2	3
Std. 2	101.6 ± 10	175.6 ± 0.2	6
Std. 3	63.5 ± 10	53.2 ± 0.2	13

Table 5.2: Parameters and uncertainties for cylindrical PEEK tubes used as standard components. The well defined hydraulic resistance enables a calibration of the flow setup at different flow rates and dynamic pressures.

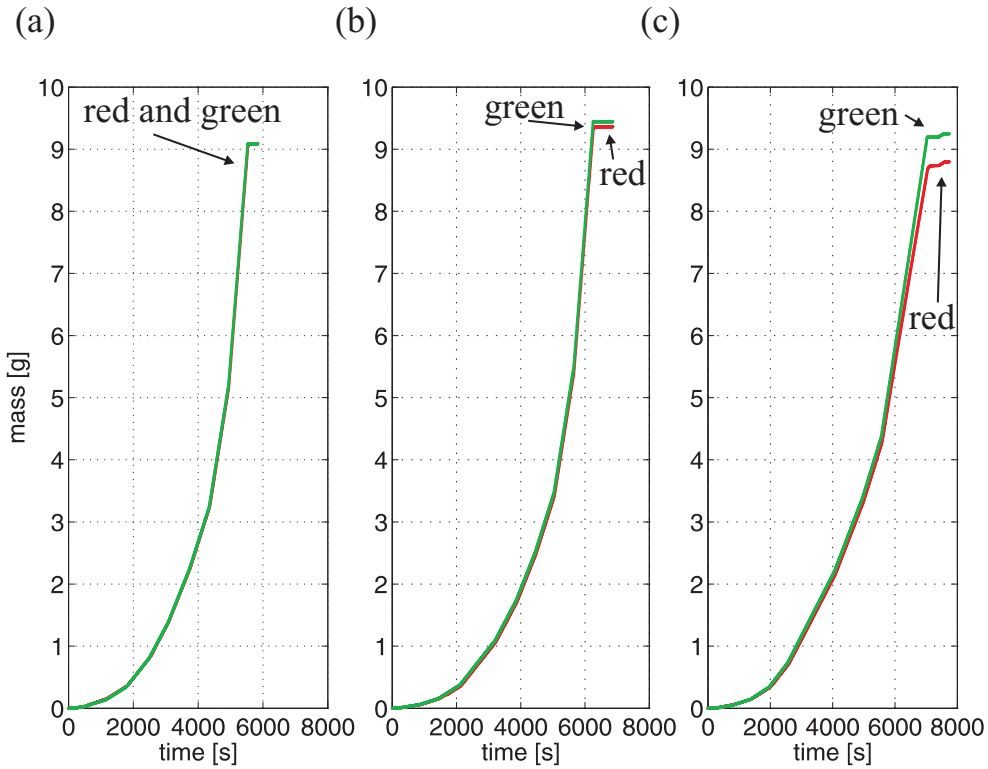

Figure 5.3: Measurements with flow setup: mass conservation. Measurements of mass conservation using the Flow setup Fig. 5.1 and Standard components Table 5.2. Panels (a), (b) and (c) are the standard components Std. 1, Std. 2, and Std. 3, respectively. The red lines show the mass pumped into the fluidic network, and the green lines show the mass accumulating on the balance. In all three cases mass is lost during the experiment. The largest loss is observed on Std. 3, where the largest pumping pressure were used. At high pressures a small leakage were observed between the seal of the syringe piston and the glass cylinder. The loss of mass is, therefore, nonlinearly related to the pressure. This problem is illustrated in Fig. 5.4.

Verification of flow setup: mass conservation

Fig. 5.3 shows a measurement of mass conservation, where the three different standard

components have been inserted, in order to test the performance at different back pressures. Std. 1, Std. 2, and Std. 3 are displayed in panel (a), (b) and (c), respectively. The red lines show the mass pumped into the system, and green lines shows the mass entering the balance. As stated earlier, these have to be equal for a system without leakage to the surroundings. In all three cases mass is lost during the experiment, and the largest loss is seen in panel (c), which indicates that the loss is pressure related. A small leakage was observed in the piston seal at high pressures, and this is considered as an explanation of the lost mass.

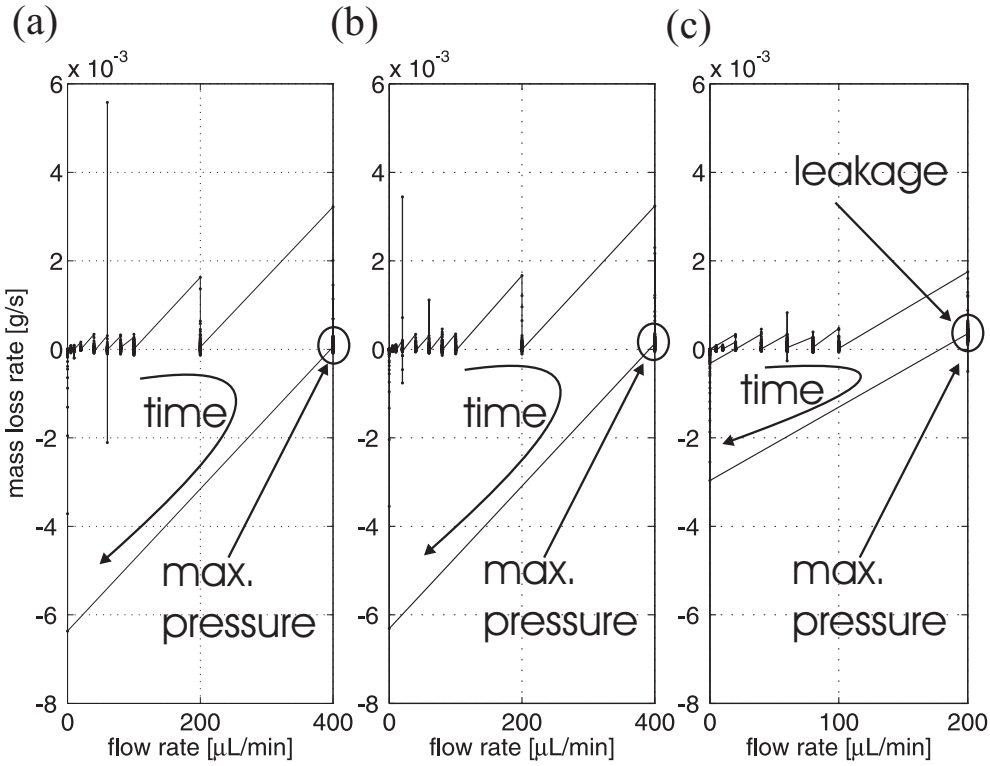

Figure 5.4: Measurements with flow setup: loss of mass rate. The experiment proceeds in the loop indicated with a time arrow. At the beginning and in the end of the experiment the loss rate is zero. Each time the flow rate is increased there is a transient loss, which reaches a steady state within half a minute. A positive loss rate corresponds to leakage or accumulation in the system, i.e., loss of mass is the difference between pumped mass and mass entering the balance. Panel (a), (b) and (c) shows the characteristics for Std. 1, Std. 2 and Std. 3, respectively. The maximum pressure in (a) and (b) is below 3.7×10^5 Pa, and the loss rate appears constant for a given flow rate. More precise, the loss is less than 2×10^{-4} g s^{-1} or 12 μL min^{-1}. At pressures above 6×10^5 Pa, the maximum pressure in (c), the loss rate is permanent and indicates a leakage. The leakage is smaller than 4×10^{-4} g s^{-1} or 24 μL min^{-1}. At the point indicated with max. pressure, the pump is stopped and accumulated mass is expelled onto the balance reservoir. This is observed as a negative loss rate.

Verification of flow setup: transient and permanent loss of mass rate
In Fig. 5.4 the relation between loss of mass rate, and flow rate at different pressures is investigated further. Panel (a), (b) and (c) is a different representation of the data in Fig. 5.3. In each panel an arrow is indicating the evolution of time, and each experiment is started with zero flow rate. Flow rate is indicated on the x-axis, and the loss of mass rate on the y-axis. Loss of mass indicates an accumulation or leakage and is the difference between pumped mass and mass entering the balance. Each time the flow rate is increased, there is a transient loss of mass (accumulation), which eventually reaches zero. In panel (c), however, where we pump against a maximum back pressure of 6×10^5 Pa, we notice that there is a permanent loss of mass rate (leakage). As we in panel (a), and (c) pumped below pressures of 3.7×10^5 Pa, we shall use this as a first limit for conservation of mass.

Verification of flow setup: flow rates and dynamic pressure
Another measured property is the dynamic pressure p. As the flow in the standard components is laminar, we can use the Hagen-Poiseuilles equation Eq. (5.1), to calculate the corresponding flow rate Q_p. The pressure is given by

$$\Delta p = \frac{8}{\pi}\frac{\mu L}{a^4} Q_p, \tag{5.1}$$

where L and a are the tube length and radius, respectively. Fig. 5.5 shows a comparison of the pumped flow rate Q_{pump}, the flow rate onto balance Q_{bal}, and the pressure derived flow rate Q_p for a temperature at 20 °C. The figure is a different representation of the data in Fig. 5.3 and Fig. 5.4. For the low pressure experiments on the large diameter standard components represented in panel (a) and (b), the pressure derived flow rate is systematically too small. On the small diameter tube, the pressure increases suddenly, and this incident is still unexplained. If it was due to a partly blocking of the channel, we should not observe the too low Q_p measurement, at the end of the experiment. Although the problem is unexplained, we expect the incidence to be related too small diameter tubes, and for such experiments extra attention and thoroughness should be paid.

Fig. 5.6 is yet another presentation of the data. The figure illustrates that Q_p in general is 20% too low, but as we have encountered problems in keeping a constant temperature, we shall not recalibrate the measurement. It was observed that the temperature during an experiment could increase from 20 to 24 °C due to heat radiation from the pump. Such a temperature increase results in a 10% decrease of the viscosity, and, consequently, a 10 % increase in Q_p.

Retrospectively, the pressure transducer should have been calibrated against a constant and well defined static pressure, and data should be recalculated. However, such a calibration was not performed, and we shall keep in mind that the measured pressure is between 10 and 20% too low, when we interpret our results.

Verification of flow setup: compliance and leakage
Compliance is an important valve parameter, as it defines how fast the pressure will rise,

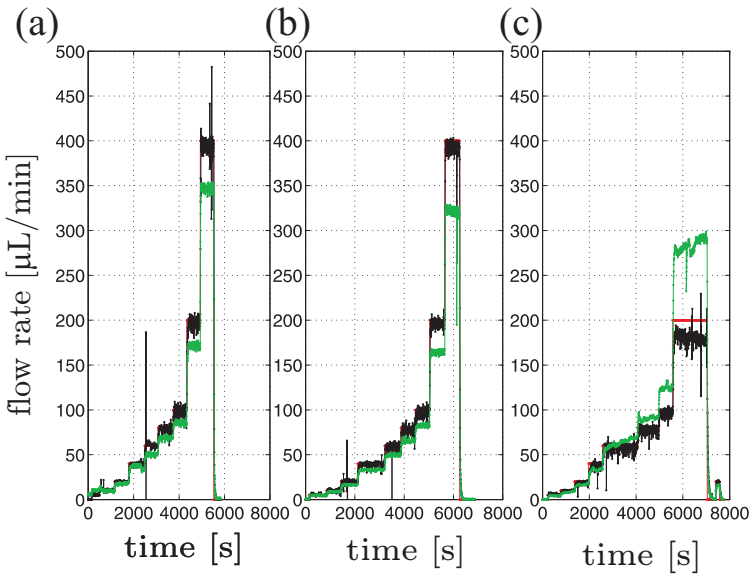

Figure 5.5: Measurements with flow setup: flow rates. Measurements of flow rates on standard components (colors in online version). Panel (a), (b), and (c), show the flow characteristics for Std. 1, Std. 2, and Std. 3, respectively. Red lines illustrate the pumped flow rate Q_{pump}, black lines the flow rate onto the balance Q_{bal}, and green lines the pressure derived flow rate Q_p. The red line is only visible on (c), on (a) and (b) it coincides with the black. For Std. 1, and Std. 2 the pressure derived flow rate is systematically too small, this can be due to an insufficient calibration. For the small diameter standard component, Std. 3, the pressure derived flow rate increases during the period with a pumped flow rate at 60 μL min^{-1}. The syringe leakage discussed in Fig. 5.4, would result in a pressure drop, and consequently a smaller Q_p. Therefore, the observed pressure increase could be related to a partly blocking of the flow channel However, at the end of the experiment the flow rate is decreased to 5 μL min^{-1} and the pressure related flow rate is again smaller than the pumped flow rate. In conclusion, Q_{bal}, and Q_{pump} are properly calibrated for pressures below 3.7×10^5 Pa, as seen in Fig. 5.4, and Q_p is 20 % too small. Although the ambient temperature was 20 °C, the pump engine heated the liquid in the container. The temperature can, therefore, be between 20 and 24 °C. Such an increase will result in an almost 10 % increase of the derived flow rate Q_p, therefore data are not calibrated, and we should keep in mind that the measured pressure may be between 10 and 20 % too small.

when fluid is pumped into a closed valve. If we want to use the setup to measure this quantity, we need a flow setup with a small compliance. Fig. 5.7(a) shows the pressure as a function of time for different flow rates. The measurements are obtained in a setup where the flow components has been replaced with a rigid plug, and we, therefore, measure the system's compliance. At the peak point the pump is stopped, and the pressure decreases. This indicates a leakage.

If we denote the accumulating flow rate Q_{acc}, and notice that Q_{acc} before and after the peak is of same magnitude, but with a different sign, we can (before the peak point) write $Q_{\text{pump}} - Q_{\text{leak}} = Q_{\text{acc}}$, where Q_{leak} is leakage to the surroundings. After the peak point, where the pump is stopped, we have $-Q_{\text{leak}} = -Q_{\text{acc}}$, and can, therefore,

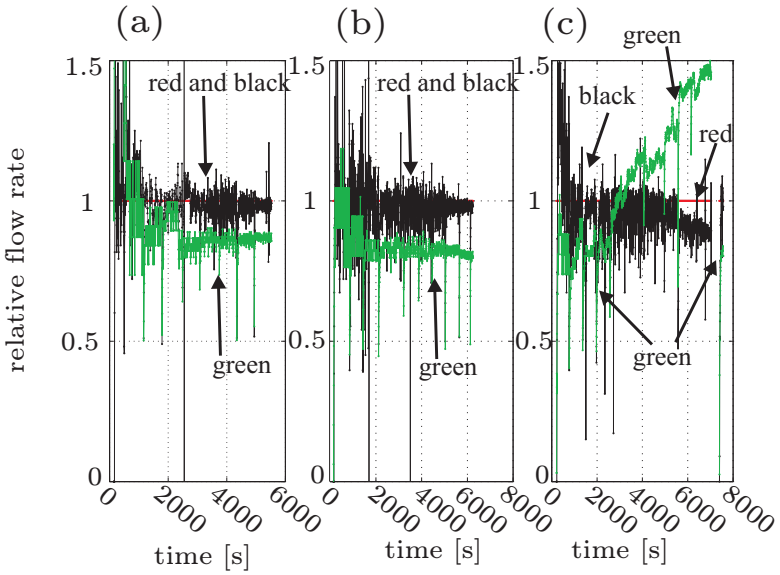

Figure 5.6: Measurements with flow setup: relative flow rates. Measurements of the relative flow rates $Q\,Q_{\text{pump}}^{-1}$ on the standard components (colors in online version). Panel (a), (b), and (c), show the flow characteristics for Std. 1, Std. 2, and Std. 3, respectively. The measurements are a different representation of Fig. 5.5. For flow components with a channel diameter larger than 100 μm, the pressure related flow rate is 20 pct to low. This is also true for smaller diameters, but there appears to be a larger risk for partly blocking.

express the leakage in terms of the pumping flow rate $Q_{\text{leak}} = Q_{\text{pump}}/2$. This leakage flow rate is comparable (within a factor 3) with the leakage found in experiments with a standard component instead of a blocked tube, Fig. 5.4. From Fig. 5.7(a) we have: $p = 0.4 - 0.45$ MPa, $Q_{\text{pump}} = 20\ \mu\text{L}\,\text{min}^{-1}$, $Q_{\text{leak}} = 10\ \mu\text{L}\,\text{min}^{-1}$; $p = 0.2$ MPa, $Q_{\text{pump}} = 5\ \mu\text{L}\,\text{min}^{-1}$, $Q_{\text{leak}} = 2.5$. From Fig. 5.4(a) and (b) we have: $p < 0.37$ MPa and $Q_{\text{leak}} = 12\ \mu\text{L}\,\text{min}^{-1}$. From Fig. 5.4(c) we have $p = 0.6$ MPa and $Q_{\text{leak}} = 24\ \mu\text{L}\,\text{min}^{-1}$. Fitting these four points with a linear regression line, would give

$$p = R_{\text{leak}} Q_{\text{leak}} + p_{\text{leak}}^0, \tag{5.2}$$

with $R_{\text{leak}} = 10^{15}\ \text{Pa}\,\text{s}\,\text{m}^{-3}$ and $p_{\text{leak}}^0 = 0.18$ MPa is the threshold pressure for the setup. These results indicate that leakage starts at $p = 0.18$ MPa, and that the hydraulic resistance of the leakage flow is around $10^{15}\ \text{Pa}\,\text{s}\,\text{m}^{-3}$. The significance of the regression line is $R^2_{\text{regression}} = 0.96$. This is a low statistical significance, and the result can therefore only be used as an indication.

Fig. 5.7(b) shows the pumped mass at different flow rates as a function of pressure, and in such a diagram the slope would be the compliance in analogy to the capacitance of a capacitor. At a pump flow rate at 5 μL min^{-1} the compliance of the system is 0.33 $\mu\text{L}\,\text{Pa}^{-1}$. Due to the leakage, compliance measurements above 0.1 MPa should not be conducted.

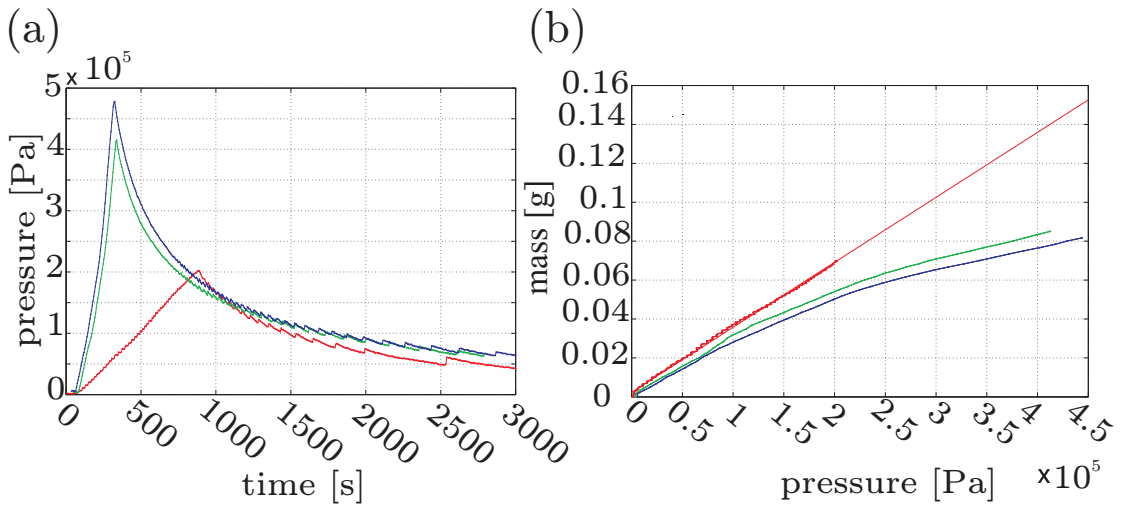

Figure 5.7: Measurements with flow setup: compliance. Measurements of pressure at a constant flow rate for a blocked fluidic system, where the fluidic system consists of the inlet tubing and the pressure sensor. In that way we measure system compliance. At the peak point, the pump is stopped and it is noted that the pressure decreases, which indicates a leakage. (a): The green and blue graph show how the pressure increase for a pumped flow rate of 20 μL min^{-1}, and the red graph for 5 μL min^{-1}. (b): The colors represent the same parameters as for the experiments in (a). The graphs show the pumped mass as a function of pressure. Compliance in the system appears to be time dependent as there is a significant difference between the characteristics for a 5 and 20 μL min^{-1} flow rate. At a pump flow rate at 5 μL min^{-1} the compliance of the system is 0.33 μL Pa^{-1}.

5.3 Sealing

With the plug-sealing geometry, we study different aspects of pressure seals in order to establish general design rules. What we would like to achieve is the ability to estimate the threshold pressure, and an understanding of the interaction between the fluid and solid structure after the seal has broken.

5.3.1 Plug-sealing test

Exp. no.	Channel in. diam. 10^{-4} m	Channel out. diam 10^{-3} m	Plug ID	Plug diam. 10^{-4} m	Rod length 10^{-3} m	Threshold pressure 10^5 Pa
1	2.6 ± 0.1	1.2 ± 0.1	2	2.5 ± 0.1	1.4 ± 0.2	1.5 ± 0.1
2	2.6 ± 0.1	1.2 ± 0.1	2	2.5 ± 0.1	1.4 ± 0.2	1.3 ± 0.1
3	2.6 ± 0.1	1.2 ± 0.1	3	2.5 ± 0.1	1.8 ± 0.2	1.2 ± 0.1
4	2.6 ± 0.1	1.2 ± 0.1	5	2.5 ± 0.1	6.2 ± 0.2	1.5 ± 0.1
5	2.6 ± 0.1	1.2 ± 0.1	6	3.9 ± 0.1	1.2 ± 0.2	4.3 ± 0.1

Table 5.3: Measured parameters plug-sealing geometry: small bore tubes. The threshold pressure is defined as the pressure, where the flow rate onto the balance exceeds 2 μL min^{-1}. Exp. 1 to 4 are represented in Fig. 5.9(a) and Fig. 5.10. The geometries are referred to as flow test geometries with small bore tubes and small diameter plugs. Exp. 5 is represented in Fig. 5.11, and is referred to as a test geometry with a small bore tube and a large diameter plug.

Exp. no.	Channel in. diam. 10^{-4} m	Channel out. diam 10^{-3} m	Plug ID	Plug diam. 10^{-4} m	Rod length 10^{-3} m	Threshold pressure 10^5 Pa
6	5.2 ± 0.1	3.7 ± 0.1	10	4.9 ± 0.1	1.0 ± 0.2	0.03 ± 0.01
7	5.2 ± 0.1	3.7 ± 0.1	11	4.9 ± 0.1	1.7 ± 0.2	0.01 ± 0.01
8	5.2 ± 0.1	3.7 ± 0.1	12	4.9 ± 0.1	1.8 ± 0.2	0.03 ± 0.01
9	5.2 ± 0.1	3.7 ± 0.1	13	4.9 ± 0.1	5.4 ± 0.2	0.05 ± 0.01
10	5.2 ± 0.1	3.7 ± 0.1	18	5.9 ± 0.1	2.0 ± 0.2	2.5 ± 0.1
11	5.2 ± 0.1	3.7 ± 0.1	20	5.9 ± 0.1	4.0 ± 0.2	2.4 ± 0.1

Table 5.4: Measured parameters plug-sealing geometry: large bore tubes. The threshold pressure is defined as the pressure, where the flow rate onto the balance exceeds 2 μL min^{-1}. Due to the poor sealing quality in Exp. 6 to 9, the threshold pressure corresponds to the steady state dynamic pressure. Exp. 6 to 9 are shown in Fig. 5.9(b) and Fig. 5.12, and the used geometries are large bore tube with small diameter plugs. Exp. 10 and 11 are represented in Fig. 5.13, and the used geometries are referred to as large bore tubes with large diameter plugs.

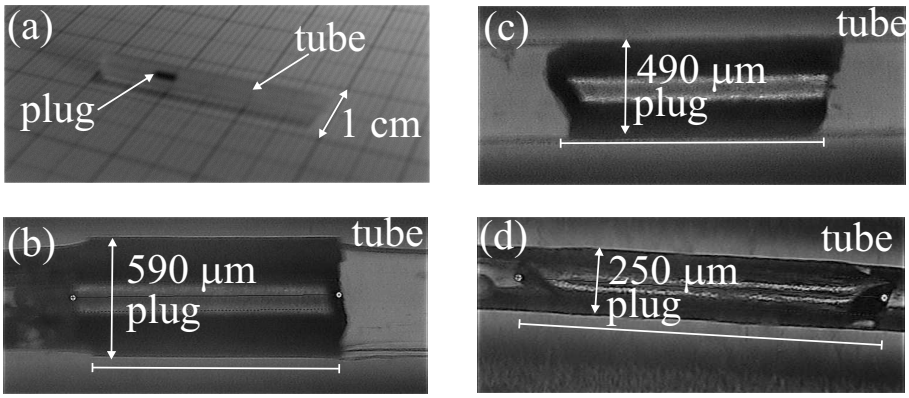

Figure 5.8: Plug sealing test geometries. (a): The plug sealing test geometry, which essentially is a steel plug in a silicone tube. (b), (c) and (d) shows microscope pictures of three different geometries. White bar aligned with channel indicates the approximate plug length. (b): Channel diameter 520 μm, plug diameter 590 μm. (c): Channel diameter 520 μm, plug diameter 490 μm. (d): Channel diameter 260 μm, plug diameter 250 μm. In (d), it is difficult to see that the rod diameter is smaller than the channel diameter, and deviations on dimensions, may actually result in local overlap.

We have conducted 11 experiments with the plug-sealing geometry, and parameters are seen in Tables 5.3 and 5.4. The test geometry is basically a silicon tube, as seen in Fig. 5.8(a), where a steel plug has been inserted in the channel, and the parameters we can vary are the tube bore, the plug diameter, and the plug length. The geometries can be divided into four categories:

- small bore tube with small diameter plugs
- small bore tubes with large diameter plugs
- large bore tubes with small diameter plugs
- large bore tubes with large diameter plugs

Whether a plug diameter is large or small, is a matter of size compared to the bore of the tube, i.e., if the diameter-to-bore ratio is larger than one, the plug is large.

The strength of the pressure seal is dependent on the magnitude of the contact pressure between the silicone rubber and the plug. We shall consider two types of forces which contribute to the pressure, namely, the compression forces and adhesive forces. The latter is rarely observed for dry rigid systems, but for soft materials it can have an influence, as discussed in Chapter 3. Compression forces appear in test geometries with large diameter plugs, and adhesive forces are observed in some test geometries with small diameters. However, if the diameter is too small compared to the bore, the adhesive forces are negligible, and we cannot observe a threshold pressure. Even though results on threshold and leakage are obtained in the same experiment, we will first present results of threshold

measurements, and proceed afterwards to the leakage measurements.

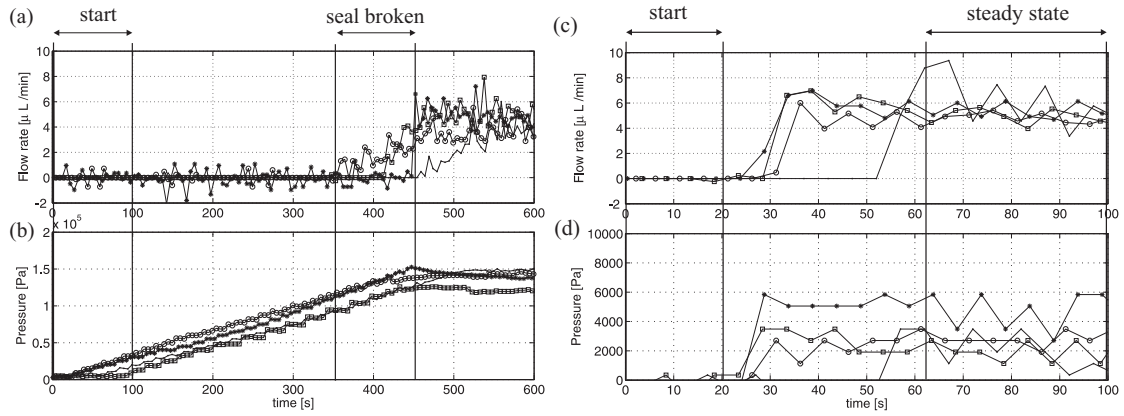

Figure 5.9: Measured threshold pressure: plug-sealing geometry. Measurements of the threshold pressure in plug-sealing geometries, based on experiments listed in Tables 5.3 and 5.4. (a) and (c) shows the flow rate onto the balance, for a pumped flow rate $Q_{\text{pump}} = 5\ \mu\text{L min}^{-1}$, and (b) and (d) show the corresponding pressure. (a) and (b): Points " $\cdot$ " , " $\circ$ ", "$\square$", " $*$ " refer to Exp. 1, Exp. 2, Exp. 3 and Exp. 4, respectively. The experiments are started between 10 and 100 s, and the seals are broken between 350 and 450 s. The threshold pressures are between 1.2 and 1.5×10^5 Pa. (d) and (c): Points " $\cdot$ " , " $\circ$ ", "$\square$", " $*$ " refer to Exp. 6, Exp. 7, Exp. 8 and Exp. 9, respectively. The experiments are started between 0 and 20 s, and the seal is broken between 350 and 450 s. The threshold pressure seal, if any, is too small to be detected. The steady state regime is indicated on the figure, and these measurements can be used to characterize the flow restriction.

Threshold pressure

Fig. 5.9 shows the measurements of the threshold pressure for the small plug test geometries. Panel (a) shows the results for the small bore tubes, and p_{th} is on the order of 10^5 Pa, which is surprisingly large. The experiments are conducted in the following way: the flow rate is increased from 0 to 5 μL min^{-1} in the indicated start interval. As the plug obstructs the flow channel, the pressure increases, and the elastic tube expands. In the indicated *seal broken* interval, the pressure exceeds the contact pressure in the seal and liquid flows onto the balance with 5 μL min^{-1}. For clarity, the balance flow rate is not shown on the graph. According to parameter measurements the plug diameter should be 10 μm smaller than the tube bore. However, a strong pressure seal is observed, and it is expected that the contact pressure is governed by adhesive forces. Furthermore, due to parameter uncertainties we cannot exclude local deformation of the tube. It is noted that p_{th} is almost unaffected by the plug length.

Fig. 5.9(b) shows similar experiments for the large bore tube, small diameter plug geometries. The experiments are conducted in the same way, but due to the large gap between plug and inner tube wall (30 μm), we do not observe a threshold pressure. On the figure is indicated a start interval, where the pump is turned on, and an interval where we have reached a steady state, with a slightly elevated pressure on 10^3 Pa.

Similar experiments are conducted to obtain the measured threshold pressure of Exp.5

in Table 5.3, Exp.10 and Exp.11 in Table 5.4.

Leakage: Small bore tubes
It may be argued that the threshold pressure is the most important property. However, we shall also take a look on the behavior, after the seal has been broken. In seals for practical purposes, the outer wall is supported by a rigid matrix, which decreases the tubes ability to expand. Due to the incompressible nature of rubber, the material will, when we apply a local pressure on one surface, expand in other regions where the surface pressure is smaller, and ideally the contact pressure should increase where a seal is desired. The objective is to be able to model this phenomenon, in order to create better or more intelligent designs. However, it should be mentioned that this phenomenon is well known from sealing with O-rings, but a better understanding of the basics, will aid a better control of the sealing processes, and an ability to design a given threshold pressure. Moreover, for the small dimensions that we desire, better control of the parameters is essential. We study the deformation in a seal without any support, as it decreases the complexity. When we can model the simple geometry, it should be relatively easy to change the boundary conditions, in order to study effects due to the incompressibility.

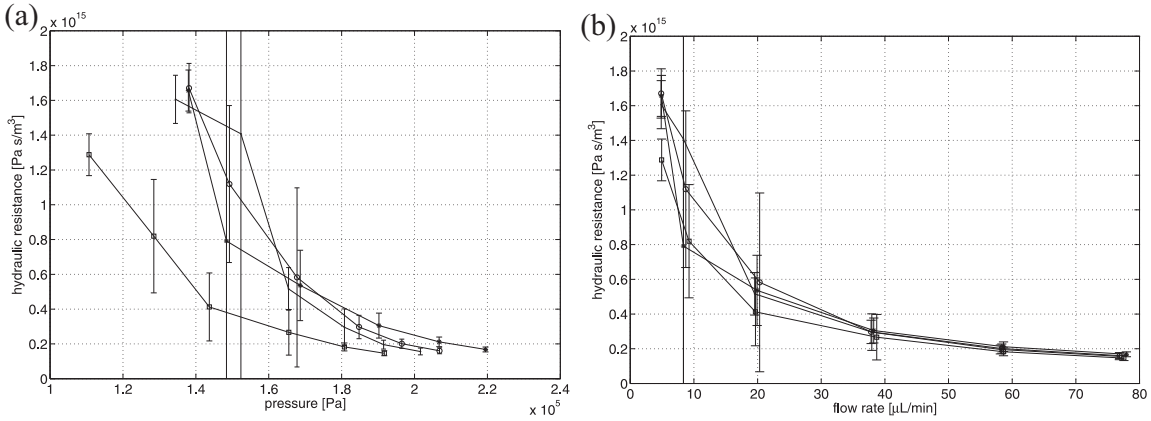

Figure 5.10: Measured hydraulic resistance. Plug-sealing geometry: small bore tubes, and small diameter plugs. Errorbars indicate standard deviations. Details of the measurements are seen in Table 5.3. Points: " $\cdot$ ", " $\circ$ ", "$\square$", " $*$ " refer to Exp. 1, Exp. 2, Exp. 3, and Exp. 4, respectively. (a): Hydraulic resistance as a function of the the steady state pressure. (b): Hydraulic resistance as a function of the stationary flow rate onto the balance. The experiments show characteristics of the seal, when it is broken, and the results can be used to develop knowledge on how to support the flexible walls in order to improve the seal quality. If we understand and are able to model the behavior of a simple plug-seal, it will be easier to estimate the effect of different support possibilities. However, this last step requires extended modelling using a finite element solver.

Fig. 5.10 shows the results from the small bore tube and small diameter plugs, after the seal has been broken, and a steady state is obtained. Panel (a) shows the hydraulic resistance $R_{\mathrm{hyd}} = p/Q_{\mathrm{bal}}$. It is noticed that the hydraulic resistance is decreasing with pressure, which is a consequence of the expanding tube wall. The corresponding flow rates

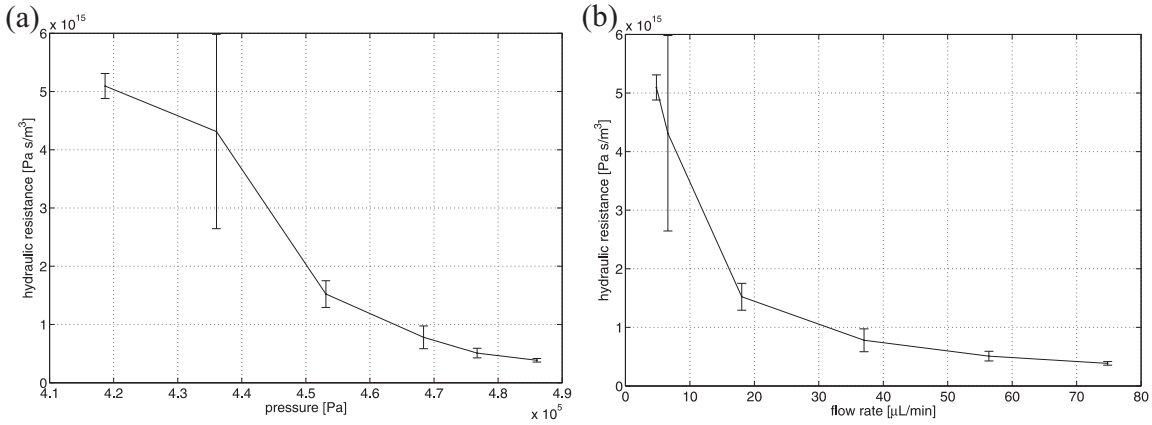

Figure 5.11: Measured hydraulic resistance. Plug-sealing geometry: small bore tubes, and large diameter plugs. Parameters are shown in Table 5.3. Points: " · " refer to Exp. 5. (a): Hydraulic resistance as a function of the the steady state pressure. (b). Hydraulic resistance as a function of the stationary flow rate onto the balance Q_{bal}.

Q_{pump} are in the range of 5 to 80 μL min^{-1}. Fig. 5.10(b) shows hydraulic resistance as a function of Q_{bal}. Q_{bal} is at high flow rates a few percent smaller than Q_{pump}, which indicates a leakage. For $Q_{\mathrm{pump}} = 80$ μL min^{-1}, we have approximately $Q_{\mathrm{bal}} = 77$ μL min^{-1}, and a leakage of 3 μL min^{-1}. Using Eq. (5.2), for the pressure $p = 0.22$ MPa we have $Q_{\mathrm{leak}} = 1.2$ μL min^{-1}. It appears that the setup containing a plug-sealing geometry is slightly more leaky, which probably is a result of an insufficient fitting between the silicone and the connecting tube.

Fig. 5.11 shows the results for the small bore tube with large diameter plugs. Compared too small bore tubes with small diameter rods (see Fig. 5.10), the trend is the same, but the pressures are much higher.

Leakage: large bore tubes

Fig. 5.12 shows hydraulic resistance as a function of pressure and flow rate, for steady state measurements on the the large bore tube, small diameter plugs geometries. The hydraulic resistance decreases with the pressure, but due the gap between plug and tube, the flow resistance is relatively low. Fig. 5.13 shows the results for the large bore tube with large diameter plugs. Again, the hydraulic resistance decreases with the pressure. However, the resistance was, as expected, much larger than for tests using small diameter plugs.

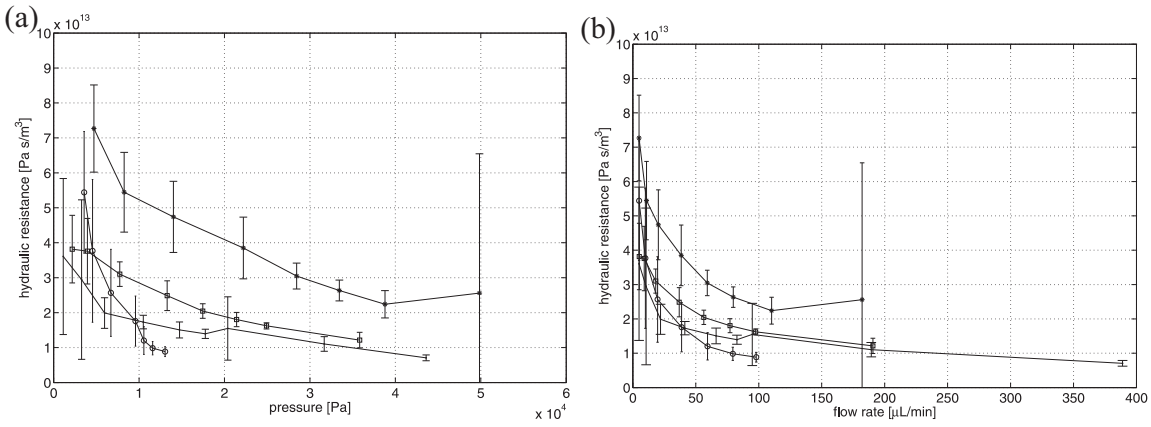

Figure 5.12: Measured hydraulic resistance. Plug-sealing geometry: large bore tubes, and small diameter plugs Table 5.4. Errorbars indicate standard deviations. Points: " · ", " ∘ ", "□", " ∗ " refer to Exp. 6, Exp. 7, Exp. 8, and Exp. 9. (a): Hydraulic resistance as a function of the the steady state pressure. (b): Hydraulic resistance as a function of the stationary flow rate onto the balance Q_{bal}.

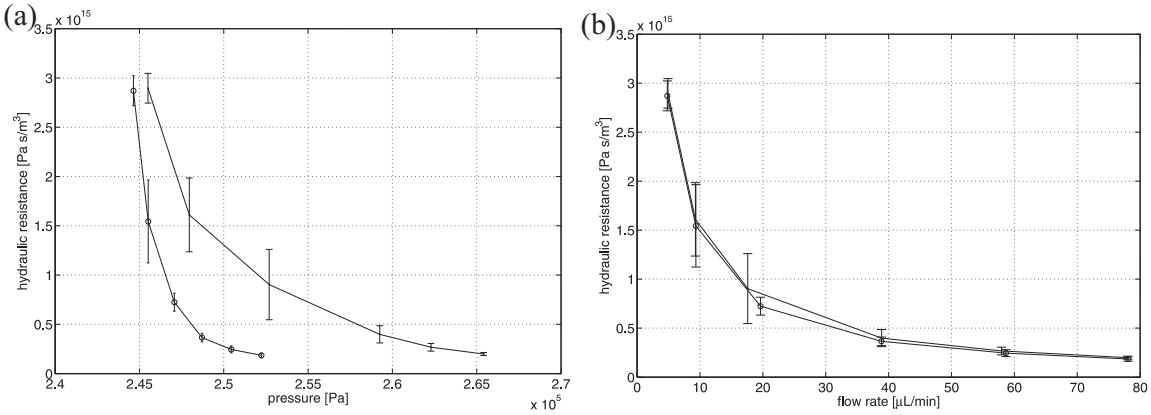

Figure 5.13: Measured hydraulic resistance. Plug-sealing geometry: large bore tubes, and small diameter plugs. Geometry parameters are listed in Table 5.4. Points: " ·", " ∘" refer to Exp. 10 and Exp. 11. (a): Hydraulic resistance as a function of the the steady state pressure. (b). Hydraulic resistance as a function of the stationary flow rate onto the balance Q_{bal}.

5.4 Friction

We shall now study the different parameters of friction, and, in analogy to the sealing property, the aim is to establish some general rules, which will aid the engineering of better seals. The parameters we will investigate is contact pressure, velocity, surface roughness, and influence of water on the surface.

5.4.1 Torque test

The first experiments we will describe are conducted with the balance based and the motor based torque setup. In both setups, we use the rotating torque geometry, which resembles the turning valve to a high degree.

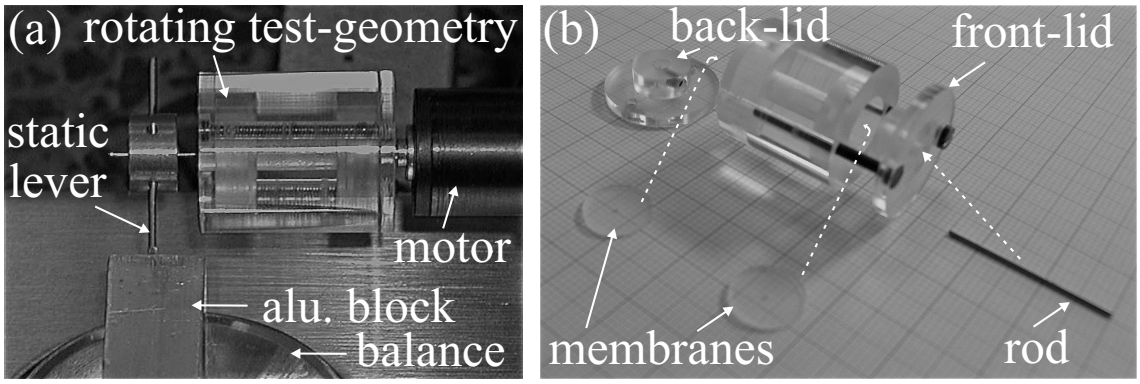

Figure 5.14: The balance based torque setup and details on torque geometry. (a): The torque geometry is fixed on the motor axle and rotates with a given speed. A rod is hanging in two membranes inside the geometry. On the rod is mounted a lever that rests on an aluminum block, which again rests on a balance. When the membranes rotate, friction induces a torque on the rod, and, consequently, a force is acting on the aluminum block. This force is measured on the balance. (b): Details of the PMMA torque geometry. The torque geometry consists of a middle-part, two membranes, a back lid, a front lid, and a rod. The parts are assembled as indicated with dashed arrows on the figure. All PMMA-parts are turned, with the result of high symmetry, which is necessary to make stable measurements. Membranes are punched out of a silicone sheet, and their symmetry is likewise essential.

The balance based torque setup
The balance based torque setup is seen in Fig. 5.14(a), and details of the geometry is seen in panel (b). The torque geometry is mounted on a motor that rotates with a given PID-regulated speed. A lever is mounted to a rod, which is hanging in two membranes fixed in the geometry. When the geometry rotates a friction torque is induced in the rod. Consequently, the lever is pushed onto the aluminum block (this is registered on the balance), and we will later describe how the balance measurement is related to the friction stress. The motor based torque setup is suitable for motor speeds below 2 rpm, and enables the measurement of very small torques. For example a 1 cm lever will theoretically enable us to measure torques in the nN m-range. However, as the lowest torques were in the

μN m-range, this is so far the lowest measured torque with this setup. Although the setup performs best at low speeds, short measurements are possible for speeds up to 100 rpm. The geometry showed in panel (b) is fabricated by drilling and milling.

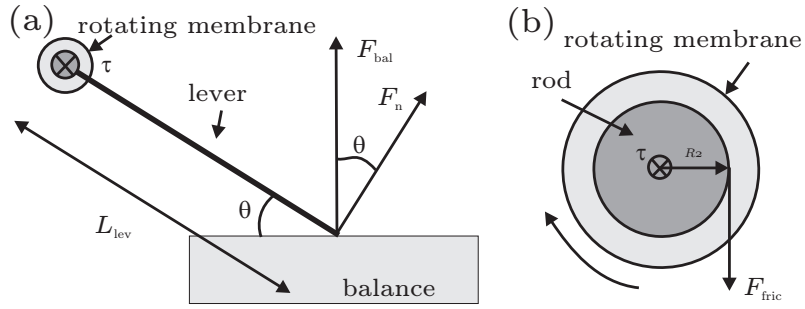

Figure 5.15: (a) Principles of balance based torque setup. Friction between a rotating membrane and a rod induces the friction torque τ. A lever, which is attached to the rod, rests on the balance. F_n is the force normal to the lever, and F_{bal} is the force component measured with the balance. L_{lev} is the length of the lever, and θ is the angle between balance and lever. The torque is given by Eq. (5.4). (b) Magnification on cross section of rod and rotating membrane, and illustration of forces on the rod. Friction from the silicone membrane induces the torque $\tau = R_2 F_{\text{fric}}$.

Fig. 5.15(a) illustrates the principles in the balance based torque setup. The friction induced torque vector τ is pointing into the plane, and F_n is the normal force from contact with the balance. F_{bal} is the force component measured on the balance, L_{lev} is the length of the lever, θ is the angle between the lever and the balance surface. In the experiments, θ was close to 90°. In that way we measure the friction located in the valve seat as sketched in Fig. 5.15(b). As the lever rests on the balance, the inertial forces are zero, and we can write the following mechanical equations

$$\tau = L_{\text{lev}} F_n, \tag{5.3a}$$

$$F_n = F_{\text{bal}} \cos(\theta), \tag{5.3b}$$

$$F_{\text{bal}} = m_{\text{bal}} g, \tag{5.3c}$$

where g is the gravitational acceleration and m_{bal} is the mass measured on the balance. Eq. (5.3a) to Eq. (5.3c) are combined to

$$\tau = L_{\text{lev}} m_{\text{bal}} g \cos(\theta), \tag{5.4}$$

which is the expression for the measured torque. The friction stress, $\sigma_{r\theta} = F_{\text{fric}}/A_1$, is then given by

$$\sigma_{r\theta} = \frac{L_{\text{lev}} F_n}{A_1 R_2}, \tag{5.5}$$

where A_1, R_2 is the contact area and rod radius, respectively. The parameters are defined in Figs. 4.4 and 5.15 (b).

Details on the torque geometry
To obtain stable measurements it is important with a high degree of symmetry, and this requirement increases with motor speed. The membranes and membrane holes are punched out of a silicone sheet, and assembled with the other parts afterwards.

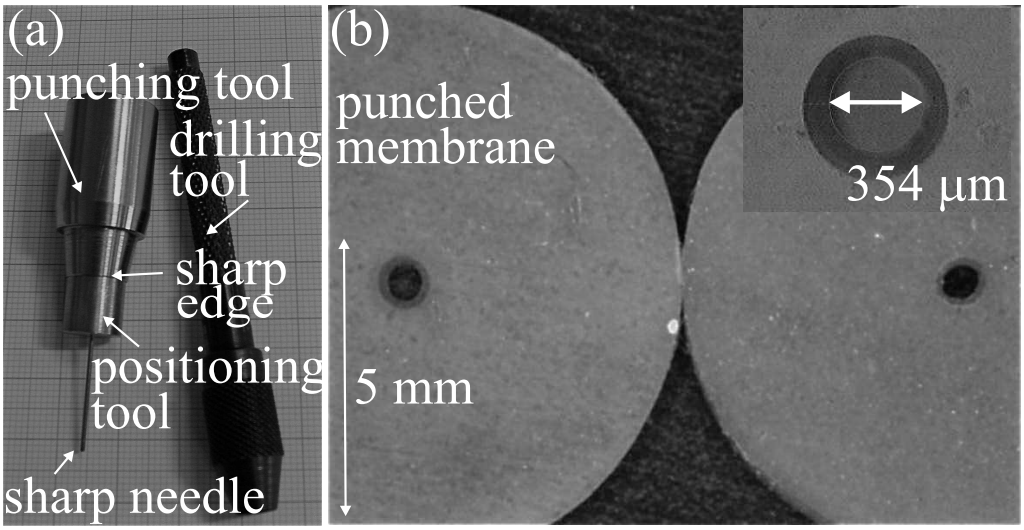

Figure 5.16: Preparation of membranes for torque geometry. (a) The tools to create a membrane ring with an outer diameter defined by the sharp edge on the punching tool, and an inner diameter defined by the sharp needle edge. The positioning tool ensures perfect centering of the membrane hole. The needle is mounted in the drilling tool, before punching. (b) Punched membranes. The membrane are ring-shaped and produced with a high degree of symmetry. The insert shows a magnification of one of the smallest membrane holes.

Fig. 5.16 shows how the membranes for the setup are produced with a special punching tool, in order to properly center the membrane holes. Panel (a) shows the punching tools and examples of the produced membranes are seen in panel (b).

Tables 5.5 and 5.6 show the different membrane and rod parameters. Membrane rings M1 and M2 can be combined with the different rods R1 to R6, and thereby create different friction levels. As we have two different membranes, we have measurements with small and large membrane holes, and we will use this as a categorization.

Membrane type	Min. hole diameter $\times 10^{-4}$ m	Max. hole diameter $\times 10^{-4}$ m	Avg. hole diameter $\times 10^{-4}$ m
M1	3.2 ± 0.1	5.0 ± 0.1	4.2 ± 0.9
M2	6.4 ± 0.1	8.6 ± 0.1	7.4 ± 1.3

Table 5.5: Measured parameters for membranes: torque geometry.

Rod type	R1	R2	R3	R4	R5	R6
Diameter 10^{-4}m	2.5 ± 0.1	3.9 ± 0.1	4.9 ± 0.1	5.9 ± 0.1	7.4 ± 0.1	9.9 ± 0.1

Table 5.6: Measured parameters for rods: torque geometry.

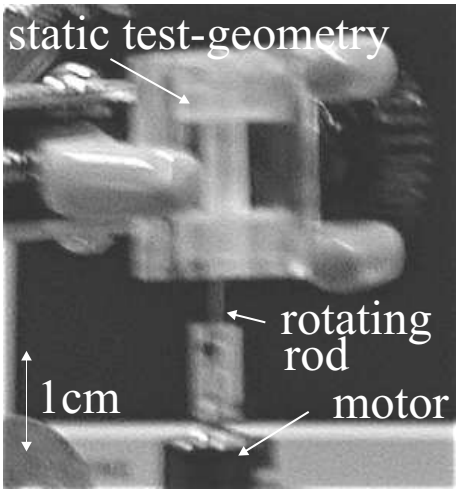

Figure 5.17: The motor based torque setup. The torque test-geometry is fixed, and the rod, mounted on the motor, rotates. The friction torque induced by the sliding process is monitored as an increased motor current.

The motor based torque setup
Fig. 5.17 shows the motor based torque setup, where the torque geometry is fixed and the rod is rotating. Compared to the balance based setup, this enables measurements at higher velocities. As the mechanical power is proportional to the motor current, we can measure the torque directly with the application software.

In a range between 50 and 100 rpm, we can use both setups. Fig. 5.18 shows a comparison of the two methods. Panel (a) shows data obtained at 10 rpm, which is to low to give stable measurements. In panel (b) are shown the measurements for 50 and 100 rpm, and the linearity is 1.4. The experiment indicates that torques measured with the motor is 40 % higher. Due to the small statistical data set, it has been chosen not to recalibrate the torques measured with the motor, and the deviation should, therefore, be considered, when such data are interpreted.

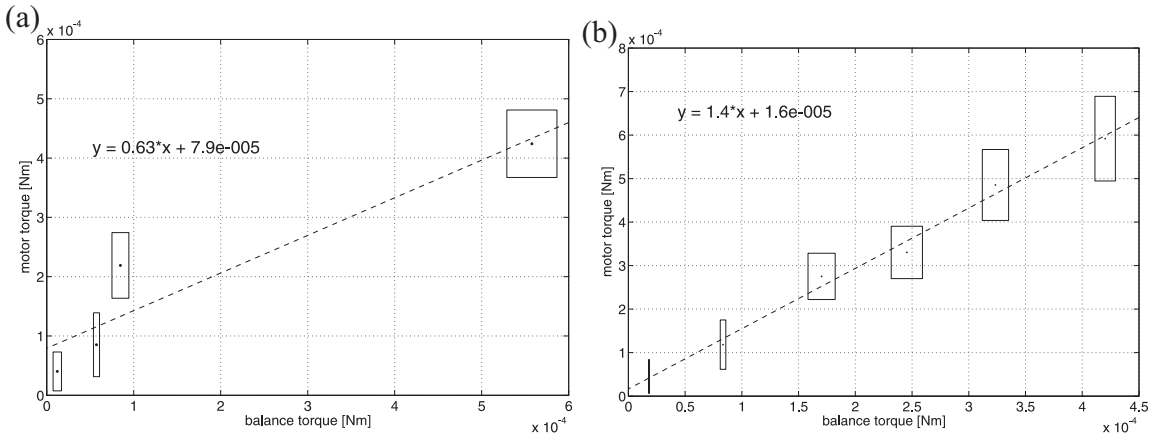

Figure 5.18: Calibration of the mechanical torque delivered by the motor, around each measurement point a box indicates the standard deviation in two coordinates. (a): the torque delivered by the motor at 10 rpm, as a function of the torque measured on the balance. The slope is 0.63 instead of the required 1.0 for correct calibration. However, at this low speed the motor is not expected to deliver a constant torque, and low speed measurements with the motor are not feasible. (b): the torque delivered at 50 and 100 rpm, the slope is 1.4, which means that the actuation energy based on a measurement of the motor current is 40 % to high.

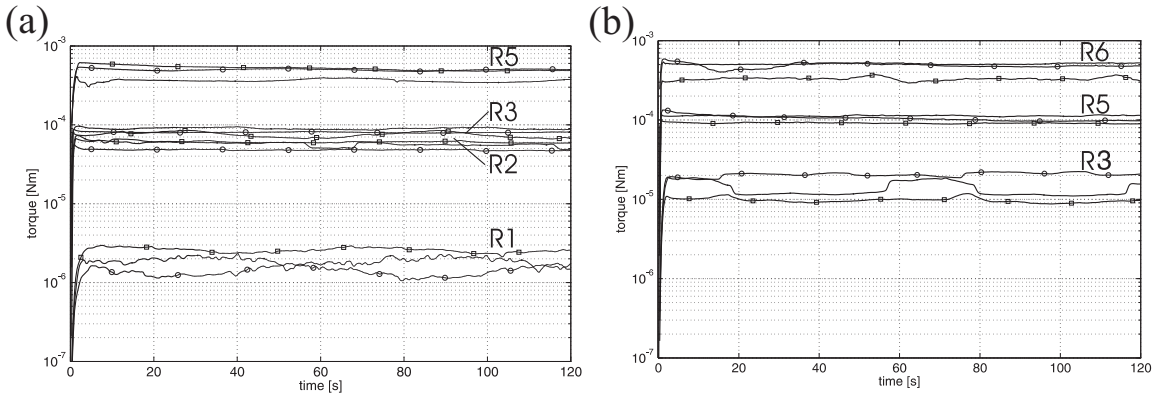

Figure 5.19: Measurements torque: torque geometry. The speed is 1 rpm, and the measurements represent two revolutions. Each combination of membrane hole and rod diameter gives a different pressure level. At each level we conducted three experiments by the combination of three different membrane sets of the type M1 or M2, and one rod of the type indicated on the figure, i.e., difference between measurements on same pressure level is due to variations in the construction of membrane holes. Hole dimension for the membranes are listed in Table 5.5. Rod parameters are listed in Table 5.6. (a): Measurements with small membrane hole (M1). The used rods R1, R2, R3, and R5 are indicated on the figure. (b): Measurements with large membrane hole (M2). The used rods R3, R5, and R6 are indicated on the figure.

Description of torque measurements

Fig. 5.19 shows the results for measurements on small and large membrane holes. At each

pressure level we have investigated the set-to-set variation between membranes, where holes were fabricated to be equal. Compared to the distance between pressure levels, the set-to-set variation is reasonably small. When the experiment is started the static friction is increasing, which is observed as an increased torque. When the static friction exceeds the maximum static friction, the torque decreases slightly and reaches a dynamic level. However, we have never observed torques more than approximately 10 % larger than the dynamic torque, and in some cases the maximum static and the dynamic pressure levels were equal. It should be mentioned that the rods where not cleaned with alcohol before the experiments, which could be an explanation on the small static-to-dynamic friction factor. Although, friction is considered as a bulk instead of a surface process contaminants could probably affect the adhesional forces. In the experiments there is a clear torque increase, when the rod-to-hole ratio increases, and we will return to this issue later.

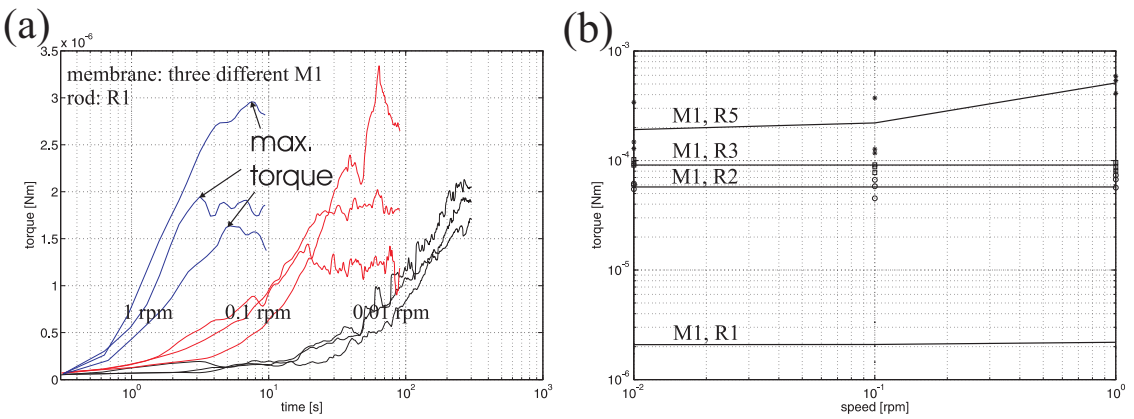

Figure 5.20: Measurements of torque at low speed levels using the torque geometry. At each speed level we conducted three experiments for the combinations of three different membrane sets and one rod. The used membrane and rod types are indicated on the figure, and their dimensions are seen in Tables 5.5 and 5.6. (a): Torque as a function of time at three different speed levels. The measurements are conducted with the combination of membrane type M1 and rod type R1. The maximum torque is indicated for the measurements at 1 rpm, and these values are used in the torque speed diagram in (b). (b): The maximum torque as a function of speed for the different pressure levels. Points " $\cdot$ ", " $\circ$ ", "$\square$", and " $*$ " refer to the combinations with membrane M1 and rod R1, R2, R3, and R5, respectively. Solid lines indicate the connection between different data sets. It is noted that the rod-to-channel ratio is the most important parameter for understanding the contributions the friction torque. The influence of speed is most pronounced at high pressure levels.

Low-speed dependence

We shall now investigate the speed dependence. Fig. 5.20 shows the low-speed dependence in the range from 0.01 to 1 rpm, using the balance based torque setup. Fig. 5.20(a) shows the sequence of an experiment where the static friction builds up and reaches a maximum. The figure illustrate three measurements on one pressure level (combination of M1 and R1), at three different speeds. If there should be a large static friction peak, it would

be better resolved at low speeds, as the sampling rate of approximately 3 Hz is constant. Note that the time-axis is logarithmic. Panel (b) shows the maximum torque as a function of motor speed, for different pressure levels. The combination of membrane and rod is indicated on the figure, and it appears that the influence of speed is small compared to the distance between compression levels. The measurement with the combinations of membrane M1 and rod R5, shows a little speed dependency, but the data set is too small to be significant. Note that both axes are logarithmic.

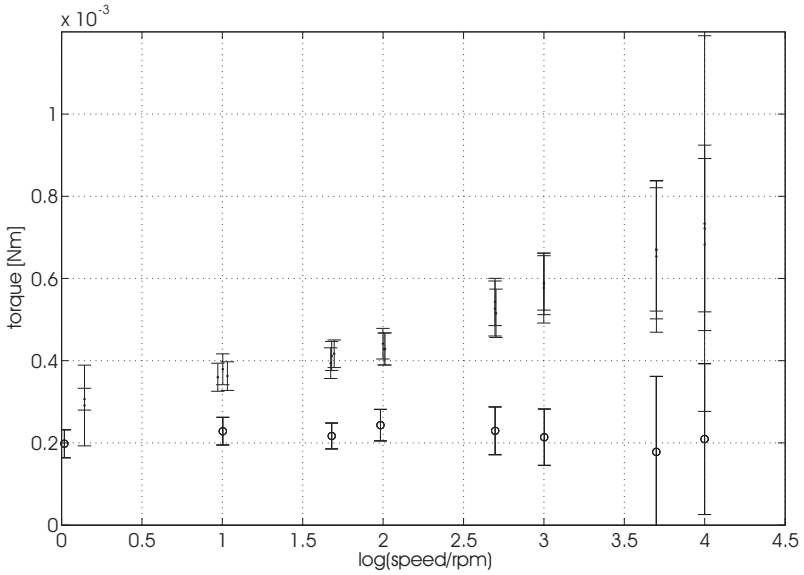

Figure 5.21: Measurements of torque at high speed levels using the motor based torque setup. Errorbars indicate standard deviations. At each speed level we conducted three experiments for the combination of three different membrane sets and one rod. The used membrane and rod types are M1 and R3, and their parameters are listed in Tables 5.5 and 5.6. Points: " $\cdot$ ", and " $\circ$ " refer to measurement with and without load, respectively. Measurements without load are reference measurement, and there is only conducted one for each speed level. The reference measurements are independent of speed. In the range from 1 to 1000 rpm the torque is more than doubled from 2 to approximately 5×10^{-4} N m.

High-speed dependence

Fig. 5.21 shows mean values and standard deviations of the torque as a function of the motor speed. The measurements were performed with the motor based torque setup, which enables measurements in the high-speed range, but due to the small memory buffer we could only acquire relatively small data-set, and the standard deviations are rather large. The graph illustrates four measurement series: one series without load, and three series with a load obtained by combining membrane M1 and rod R3. In contrast to the low speed measurements we now observe a more pronounced velocity dependence, and in the range from 1 to 1000 rpm the torque is more than doubled from 2 to approximately 5×10^{-4} N m. However, the low-speed and high-speed measurements are not directly comparable. For the low-speed measurements, we have studied maximum static friction,

and dynamic friction was used for high-speed measurements. On this basis we conclude that friction increases with velocity in a range from 1 to 10^4 rpm, corresponding to a sliding velocity of 6×10^{-4} to 6 $\mathrm{m\,s^{-1}}$. For high speed measurements, we may expect a temperature increase on the contact surface, but we have not performed any temperature measurements.

5.4.2 Tribo-test

An other important parameter for sliding friction between rubber and a hard substrate may be surface roughness, which we have tested in a roughness range which we expect to be comparable to the rods used for the torque geometry and later the turning valves.

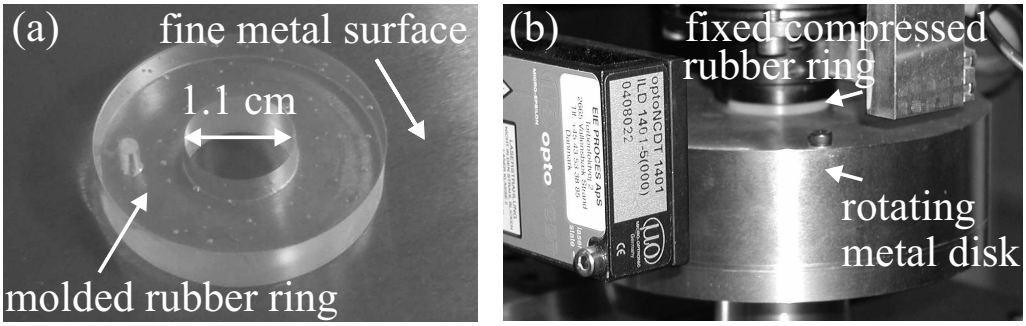

Figure 5.22: The Tribo test setup and rubber ring geometry. (a) The fine steel surface and a molded rubber ring, which is inserted in the Tribo test setup showed in (b). In this setup the silicone ring is fixed, while the metal disk is rotating. In this way we can measure the friction coefficient between rubber and two different steel surfaces. The rotation speed could also be varied, but due to the soft nature of rubber measurements above 10 rpm became unstable.

Fig. 5.22 shows a picture of the tribotest setup. Panel (a) shows the molded silicone ring, and panel (b) shows how the measurements are performed. The inner and outer diameter of the rubber ring was 1.1 and 2.85 cm, respectively. This gives a contact area of 543 $\mu\mathrm{m}^2$. Parameters for the two different surfaces and the rubber ring are collected in Table A.2.

Fig. 5.23 shows an overview of the conducted roughness experiments. Two experiments are performed with the fine surface roughness shown in panel (a) and (b), and four on the rough surface shown in panel (c), (d), (e), and (f). Each figure shows a series of measurements with one ring, and no significant difference was observed between the first and the following measurement. The rubber ring is changed between different measurements series (one series represented in each figure), and it would, therefore, be revealed, if the measurements were sensitive to the molding process. However, this influence appeared to be insignificant.

As the valve should function with the presence of water we will also investigate this factor with the tribo tester, and a last parameter of interest is the normal force.

Table 5.7 shows the friction coefficient from the tribo test experiments, which all

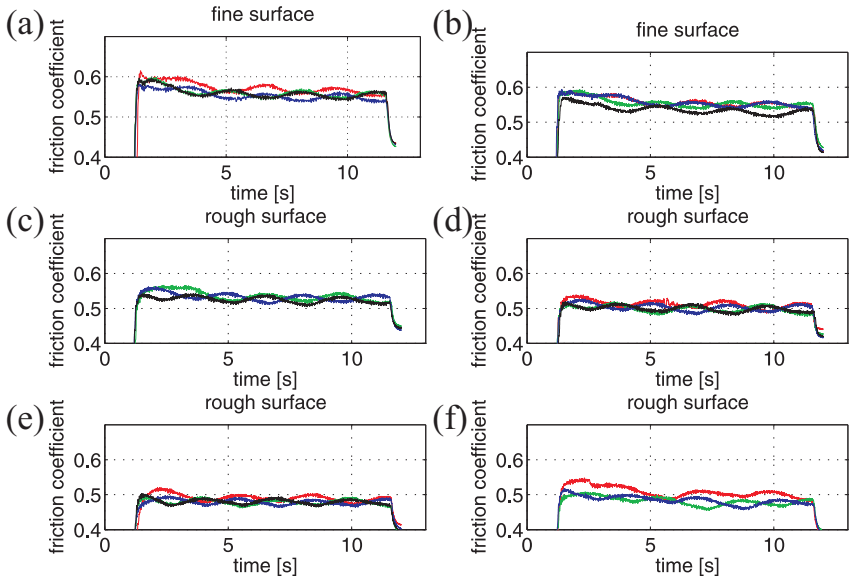

Figure 5.23: Measurements of friction coefficients with tribo-tester and rubber ring geometry. Parameters for geometries in the tribo-test setup is seen in Table A.2. (a) and (b): four measurements of the friction coefficient with two different rubber rings on a fine metal surface. Figure (c), (d), (e), and (f): measurements with four different rings on a rough metal surface. All results from the tribo-test are seen in Table 5.7

Exp. no.	Surface roughness	Water on surface	Normal force 38 N	Normal force 55 N	Normal force 75 N
1	fine	no	0.5 ± 0.1	0.5 ± 0.1	0.5 ± 0.1
2	fine	yes	0.5 ± 0.1	0.5 ± 0.1	0.4 ± 0.1
3	rough	no	0.49 ± 0.07	0.46 ± 0.08	0.46 ± 0.07
4	rough	yes	0.4 ± 0.1	0.4 ± 0.2	0.38 ± 0.07

Table 5.7: Measured friction coefficients: tribo tester, rubber ring geometry. Friction coefficient between rubber and a metal surface. The friction coefficient is tested for the influence of roughness and the presence of water. High contact pressure and, large roughness, and water on the surface yields the smallest of the measured friction coefficients.

were conducted with a speed of 10 rpm. There seems to be little effect of all the tested parameters. However, the combination of high pressure, large roughness, and presence of water appeared to give a smaller friction coefficient. We will for future calculations in this work use a friction coefficient of 0.5 ± 0.1.

5.4.3 Pull-force test

A valve could also be realized as a gate valve, where the rod was switched with a translational instead of a turning movement. Also the pull-force geometry combined with the plug-sealing geometry, can provide important information of sealing and actuation energy of a piston sliding in a rubber pump chamber. The friction coefficient should, however, be independent of the type of movement, but in switching a rod back and forth there may be other considerations to the actuation energy than friction. If the rod, for example, is a little misaligned with the channel it may cut into the sides of the channel, and obstruct the movement.

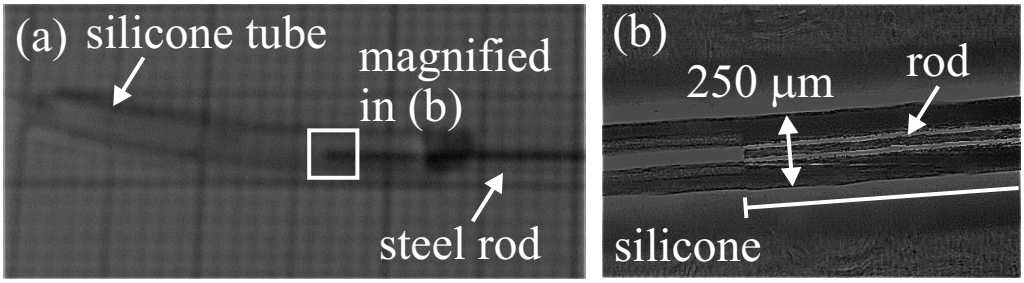

Figure 5.24: Pull-force geometry. (a) The pull-force geometry consisting of a rod inside a silicone tube. The white rectangle indicates the frame which is enlarged in (b). The rod diameter is 250 μm and the channel diameter is 260 μm. There may be local overlap, but no deformation can be observed on this picture.

Exp. no.	Rod diam. [μm]	Channel bore [μm]	Init. contact length [mm]	Final contact length [mm]	Friction stress [MPa]
1	250 ± 10	260 ± 10	9.1 ± 0.1	2.2 ± 0.1	0.328 ± 0.004
2	250 ± 10	260 ± 10	9.5 ± 0.1	1.9 ± 0.1	0.232 ± 0.002
3	250 ± 10	260 ± 10	7.9 ± 0.1	1.8 ± 0.1	0.367 ± 0.002

Table 5.8: Measured friction stress: pull-force geometry. Parameters and results for pull-force test. Column 2 to 5:Parameters and uncertainties. Column 6: friction stress and standard deviation.

We have tested the simplest translational movement, namely, when pulling a rod out of a cylindrical tube. Fig. 5.24(a) shows the geometry which consists of a rod clamped in a silicone tube. The silicone tube is a small bore tube (260 μm), and the rod diameter is 250 μm. All parameters for the three different pull-force geometries are listed in Table 5.8, along with the measured friction stress. Panel (b) shows a close up on the area indicated with a white box in (a). According to measurements of the individual parameters there should not be an overlap, but we cannot exclude local deformation, even though it is impossible to observe on this picture. The geometry is mounted in a standard tensile tester, where we can measure the pull force along with the elongation.

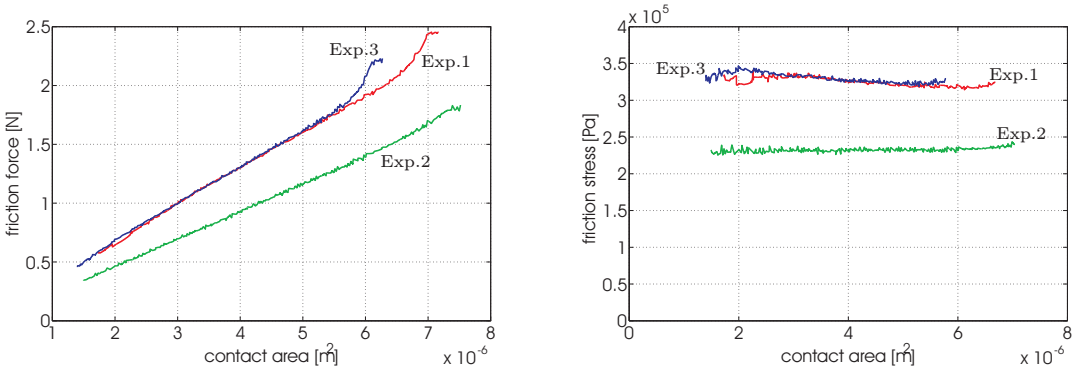

Figure 5.25: Measured friction force: pull-force geometry. Pull-force measurements of a 250 μmrod in a tube with a 260 μmbore. (a) Friction force (pull-force) as a function of the contact area. The pull velocity is 10 mm min^{-1}. The contact length was difficult to measure directly, and is estimated by assuring zero force at zero contact area. This also results in a constant friction stress as shown in (b). The friction stress is seen to be constant, but there is, however, a large deviation. Labels refer to experiments in Table 5.8

Experiments are performed by pulling the rod out of the tube, and measure the used force. Initially, the geometry elongates until the pull-force exceeds the static friction force, and the rod starts to slide. We shall study the dynamic friction in this setup, and the friction force as a function of the contact area is seen in Fig. 5.25(a). The contact area decreases during an experiment, and has been adjusted in order to assure zero force at zero contact. Fig. 5.25(b) shows the contact pressure, which is constant.

For this experiment with friction induced by a translational movement the friction force scales with the nominal contact area. One of the measurements deviates significantly from the others, this is not understood at the moment, and more experiments should be performed to draw conclusions. However, the results indicate that the friction stress in this case is in a range from 0.23 to 0.37 MPa. With a friction coefficient $\eta = 0.5$ we would, consequently, have a contact pressure σ_{rr} in the range from 0.46 to 0.74 Pa. The threshold pressure $p_{\rm th}$ obtained with small diameter plugs in small bore tubes were in the range 0.12 to 0.15 MPa, and we would expect it to equal σ_{rr}. However, the ratio between the two measurements is more than a factor of four. Even if the pressure was 20% larger after a recalibration of the p_{th}-data, it would not be sufficient to compensate for the deviation. At the moment the deviation is unexplained, but could be due to model assumptions, or that the contact pressure in the pull-force experiment increases, when the tube is elongated.

5.5 Comparing measurements and model predictions

In Chapter 4 we have established a plug-sealing model to predict threshold pressure, and relation between leakage and pressure.We have also developed a torque model to estimate friction stress for different contact areas, and contact pressures. In this chapter, we have in detail described the conducted experiments, and shall now extract the most important results. Therefore, we shall compare results and model predictions, in order to gain an increased knowledge of the performance of the seal.

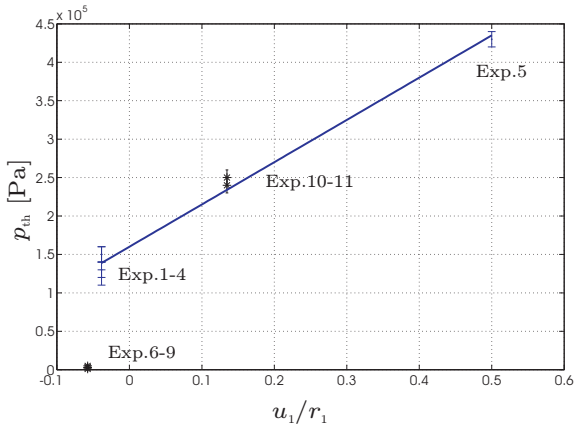

Figure 5.26: Measured threshold pressure from and comparison with plug-sealing model. The measured threshold pressure vs the relative displacement u_1/r_1. Details on the on the plug geometry used for the measurements are listed in Tables 5.3 and 5.4. Data are fitted with a linear regression, and values $k_1 = 1.6$ MPa, $k_e = 0.34$, and $p_0 = 0.16$ MPa are derived according to Eq. (5.6).

Sealing and threshold pressure
According to Chapter 4 the threshold pressure is given by

$$p_{th} = k_c\, k_e \frac{u_1}{r_1} + p_0. \tag{5.6}$$

In Tables 5.3 and 5.4 we listed the results for 11 experiments with the plug-sealing geometry. In the experiments we varied the plug-to-channel ratio resulting in different $u_1/r_1 = (R_1 - r_1)/r_1$. These values are plotted in Fig. 5.26, along with the threshold pressure, and it is noticed that a linear regression with $k_e = 1.6$ MPa, $k_c = 0.34$, and $p_0 = 0.16$ MPa fits the data.

As we showed in Chapter 4, the small and large bore tube do exhibit the same elasticity, but measurements show an elastic module 34% smaller than theoretically predicted by linear elasticity of thick walled tubes.

That p_0 is different from zero indicates that there is some uncertainty in measuring $u_1/r_1 = 0$. However, there is an abrupt increase in p_{th} between experiments Exp.6-9 and

Exp.1-4, suggesting the presence of adhesional forces. The observation of adhesional forces in the zero load limit is also known from friction measurements as described by Persson [39].

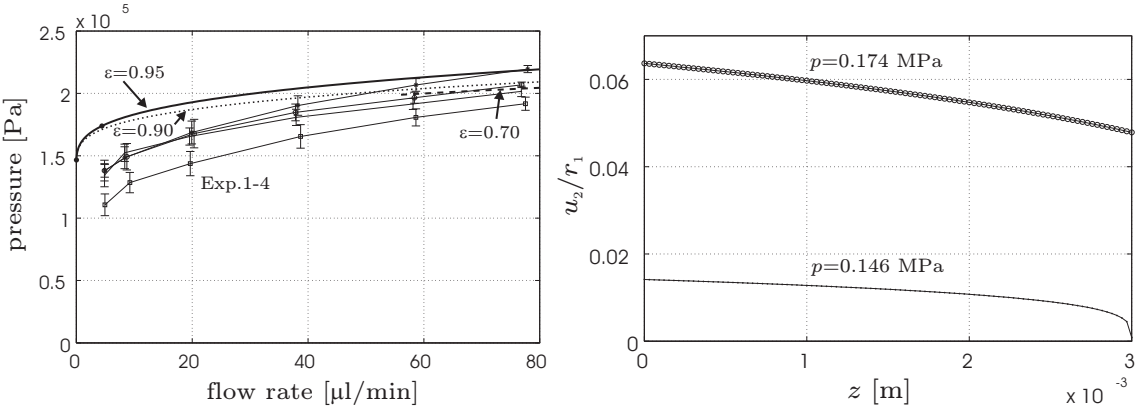

Figure 5.27: Leakage measurements and comparison with plug-sealing model. (a): Leakage measurements on small bore tube with small diameter rods are showed with data points and errorbars for standard deviation. The lines are the results of the plug sealing model (Eq. (4.15)) with different ϵ-values, which are indicated on the figure. Due to restrictions on the boundary conditions, the model does not start at zero flow rate. This off-set is increased as ϵ decreases. $\epsilon = 0.95$ appears to give the best resemblance of the data, in particular it captures the curvature at small flow rates. With this value of ϵ only 5% of the pressure is lost along the plug. On the solid line two data points indicated with $\bullet$ is represented as u_2/r_1 vs z in panel (b). (b): For $p = 0.146$ MPa, u_2-decreases strongly in the proximity of the right boundary, and for higher pressures this decrease is more moderate (calculated according to Eq. (4.12a) and Eqs. (4.14a) and (4.14b)). Due to the small u_2/ℓ_1-ratio lubrication theory is applicable and the leakage model is a good approximation. Details on parameters for the experiments are listed in Table 5.3. Model parameters: $r_1 = 125$ μm, $k_e = 1.6$ MPa, $k_c = 0.34$, $p_0 = 0.16$ MPa, $\mu = 1$ mPa s, $\ell_1 = 3$ mm. Different values of ϵ is indicated on the figure

Sealing and leakage

Understanding the relation between pressure and leakage, will provide a better background for the design of stronger and more intelligent seals. Fig. 5.27(a) shows the pressure flow rate characteristic for the plug-sealing geometry consisting of a small bore tube and small diameter rod. The measurements are represented along with three different model predictions for $\epsilon = 0.70$, $\epsilon = 0.90$ and $\epsilon = 0.95$. In the latter case, the model appears to capture the features at small flow rates, where pressure measurements indicate a larger sensitivity to variation in the flow rate. At larger flow rates both measurements and model exhibits a more moderate slope. Due to the restriction $u_2(z_2) > 0$, the modelled flow rate does not cross the zero-flow-rate-axis.

For two parameter sets (Q,p)indicated with $\bullet$ in panel (a), the u_2 profile has been represented as a function of z in panel (b). When liquid initially breaks though the seal, the channel and rod has almost contact at the downstream boundary (u_2 close to zero). When the pressure is increased further the distance between rod and channel increases.

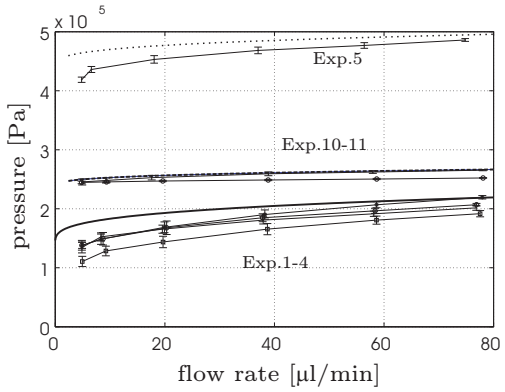

Figure 5.28: Pressure vs flow rate for all leakage measurements are shown with data points and errorbars. Details on the experiments are listen in Tables 5.3 and 5.4, and the individual experiments are labelled on the figure. Lines are results from the leakage model with $\epsilon = 0.95$. The difference in pressure level is determined by the initial displacement u_1 defined in the plug-sealing model Fig. 4.1. Model parameters: as for the experiment with the exception of $\ell_1 = 3$ mm.

In the beginning this flow restriction defined by u_2 is apparently very pressure sensitive.

Fig. 5.28 summarizes the comparison of all leakage experiments and the plug-sealing model. The model captures the pressure level, and resembles the pressure vs flow rate dependency for all experiments with the same $\epsilon = 0.95$. The model shows that only 5% of the pressure is lost along the plug.

The remaining 95% is either lost due to a larger viscous flow resistance after the down-stream edge or a pressure loss due to inertial forces, if liquid jets out in the larger outlet tube. To estimate which suggestion is the more realistic we shall calculate the Reynolds number for conditions corresponding to Exp.1-4.

According to Fig. 5.27(a) we have a parameter set $Q = 4.4\ \mu\mathrm{L\,min^{-1}}$ and $p = 0.174$ MPa, with a corresponding $u_2(z_2) = 0.6\ \mu$m. We can now calculate the cross sectional area $A = 2\pi R_1 u_2(z_2) \approx 5 \times 10^{-10}\ m^2$ and the mean velocity $V_{\mathrm{mean}} = Q/A = 0.14\ \mathrm{m\,s^{-1}}$. The Reynolds number is then

$$Re = \frac{V_{\mathrm{mean}} 2 r_1 \rho}{\mu} \approx 30, \tag{5.7}$$

where ρ is the mass density, and μ the viscosity. The tube diameter $2r_1 = D_h$ is also the hydraulic diameter, and if the outlet tube length is $L_h = 1$ cm, we can calculate the transitional Reynolds number Re_t according to Ref. [28]. $Re_t = 30L/D_h \approx 10^3$, and the flow is, therefore, laminar. There is no inertial pressure loss, and there must, consequently, be a large hydraulic resistor after the downstream plug edge.

We shall now make a quick calculation in order to estimate the dimensions of this resistance. Fig. 5.29(a) shows the plug-sealing model, where leakage has been induced due to an excessive inlet pressure. Panel (b) shows a magnification of the down-stream plug edge, where an additional flow restriction with length ℓ_2 and height u_6 is sketched. Panel (c)

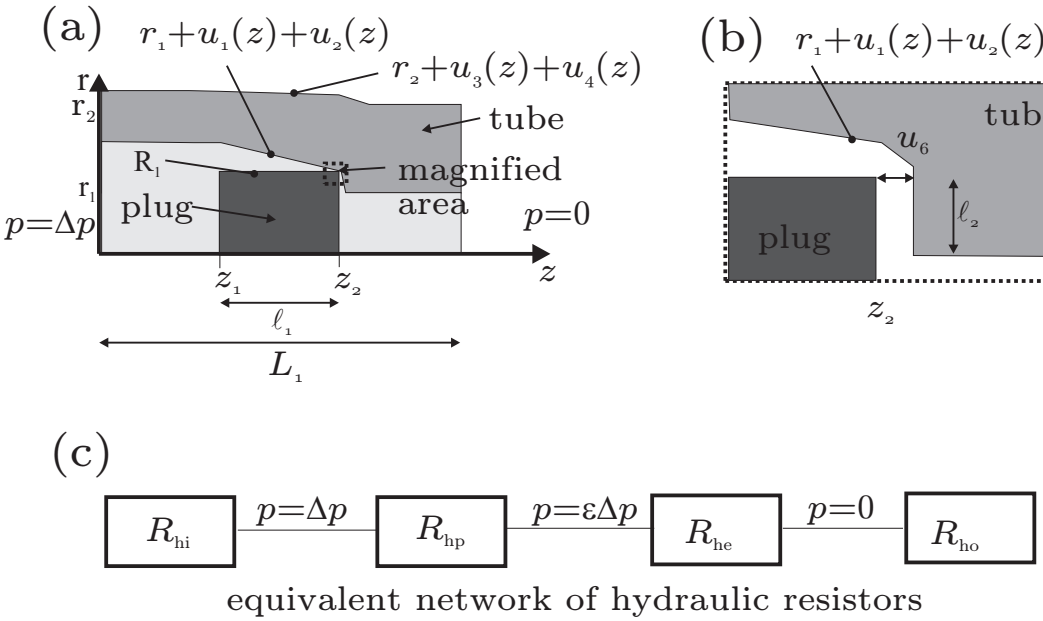

Figure 5.29: Hydraulic resistor model. (a): Increased pressure deflects the tube wall, and induces a leakage. Symbols are defined according to Fig. 4.1. (b): Magnification of the down-stream plug-edge (dashed box in panel (a)). An additional resistor exists at the plug-edge, as the plug diameter is larger than the channel bore. The flow resistor corresponds to a slit-flow channel with width $2\pi R_1$, and height u_6, and length ℓ_2. (c) Presentation of resistors as an equivalent network.

shows a series of four flow components in an equivalent network. The components are labelled $R_{\rm hi}$, $R_{\rm hp}$, $R_{\rm he}$, and $R_{\rm ho}$, for inlet, plug, edge and outlet hydraulic resistor, respectively.

The hydraulic resistance for the plug edge is calculated as $R_{\rm he} = \epsilon\Delta p/Q$ and the flow rate pressure relation is approximated with a slit flow

$$\Delta p = \frac{12\mu\ell_2}{2\pi R_1 u_6^3\epsilon}, \tag{5.8}$$

where $2\pi R_1$ is the width of the slit. Assuming that $\ell_2 = 5$ μm gives $u_6 \approx 0.3$ μm, which appears to be a realistic but small value. Supported by this little analysis the plug-sealing model strongly suggests that the major pressure loss is located around the downstream plug edge.

Due to resent years of development on even more complex finite element solvers (see for example Ref. [46]), it is now possible to simulate the interaction between fluid and structure. The plug-sealing geometry would be an excellent case to study further with these relatively new possibilities, as it would provide the first step in the process to model and design better pressure seals.

Friction

We have in Chapter 4 suggested the following empirical model

$$\sigma_{r\theta} = \eta\big(k_c\, k_e \frac{u_1}{r_1} + p_0\big), \tag{5.9}$$

where the terms in the parentheses corresponds to the contact pressure σ_{rr}. As we in Fig. 4.5 have shown that the membranes in the torque geometry behave similarly to a thick walled tube, when exerted to a internal pressure, Eq. (5.9) should fit the torque measurements.

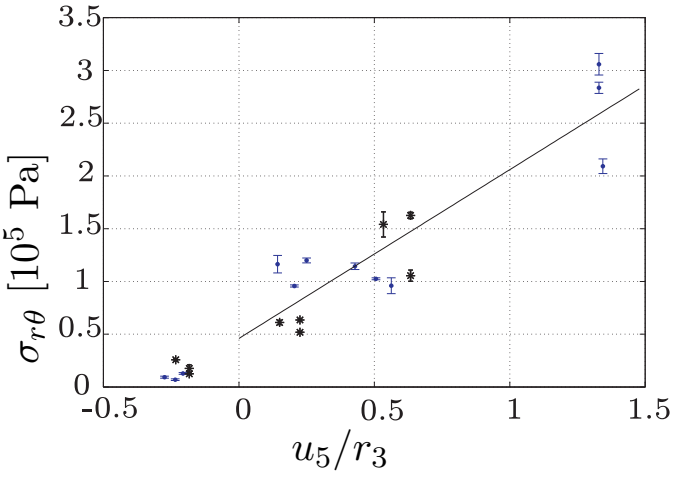

Figure 5.30: Friction stress σ_{r_θ} vs the displacement u_5 defined in Fig. 4.4. "$\cdot$" measurements with membrane M1; "$*$" measurements with membrane M2. Errorbars indicate standard deviations. Data points are mean values for one period of dynamic friction with $n = 1$ rpm, and standarddeviations are represented with errorbars. Data is extracted from Fig. 5.19. See Tables 5.5 and 5.6 for the different combinations of rod and membrane. The solid line is a curve fit on positive displacements. $\sigma_{r\theta}$ shows to be independent of the apparent contact area, and depends linearly on the displacement.

Fig. 5.30 shows the torque measurements fitted with a linear line, with $k_c = 0.26$, $k_e = 2.5$ MPa, $p_0 = 0.092$ MPa, and $\eta = 0.5$. The figure shows 21 individual data points obtained by averaging a period of dynamic friction for different combinations of membrane and rod. Dynamic friction data was represented in Fig. 5.19. All membrane holes were measured individually, and due to variations in the fabrication process there is also some variation in the measured torque. Also when punching a hole in a membrane, we do not obtain a perfect cylindrical hole. The hole is rather shaped as a cylinder, which has been narrowed on the middle (half of the height). Therefore, mean diameters were calculated of the maximum and minimum diameter of each hole. Consequently, there is some uncertainty on u_5/r_3, and we cannot expect zero friction at the zero-load limit.

Six data points represent negative values of u_5/r_3, and although the regression line appears to capture these data, the rods were clearly smaller than the membrane holes.

Therefore, these data shows the friction level, due to a contact force governed adhesional forces and by the combined mass of rod and lever.

	k_c	k_e MPa	p_0 MPa	E MPa
tube	0.34	1.6	0.16	2.4 ± 0.3
membranes	0.26	2.5	0.092	3.7 ± 0.2

Table 5.9: Elastic moduli based on data fits with plug-sealing and torque model. The friction coefficient was measured to $\eta = 0.5 \pm 0.1$, and for Poisons' ratio was used $\sigma = 0.49$.

Although $k_c = 0.26$, and there consequently is a 76% deviation from the theoretical expected module, the result is consistent with measurement obtained with the plug-geometry. Comparing results from the plug and torque geometry is summarized in Table 5.9. The discrepancy is believed to be explained by uncertainties on η, and boundary conditions. In particular the elasticity of the membrane holes will be significantly reduced, if small cracks appear in the boundary.

5.6 Summary

We have studied leakage and friction properties in geometries involving rubber and a hard substrate. It is shown that friction force scales with the nominal contact area, and the contact pressure. The threshold pressure being independent of contact area (in the investigated range), and dependent on contact pressure, enables down-scaling of contact area with the achievement of energy savings, without a trade-off in threshold pressure. When the contact area is down-scaled, we decrease the contact force and not the contact pressure. In the next chapter, we will use these findings to develop low energy valves with high pressure seals.

Chapter 6

Low energy low leakage valves: design, modelling and test

We will now take the next step from modeling and studies of basic properties, to test and characterization of real valves. We have realized three turning rod valves with different processes and in different sizes. From Chapter 5 we know that a relation between channel and rod diameter, determines the threshold pressure in a plug-seal, and although the differences between a simple seal and a turning rod valve is significant, we may expect that some compression also is necessary in the more complex component. However, what we also learned in last chapter was that the actuation energy goes up with compression, and we have to find the optimal balance.

We have produced and tested three different turning rod valves. As they all are turning valves we will often omit this adjective, and rather make a reference to the fabrication process or size. Proper and systematic naming is a surprisingly difficult task, and for historical reasons we have kept the adjective rod valve even though they all are rod valves. The three valves are named: the punched rod valve, the large molded rod valve, and the small molded rod valve.

6.1 The punched rod valve

The punched rod valve was the first component we constructed with the combination of rubber and a hard substrate, after quick studies of a turning valve where the rod was fabricated in polyoxymethylene (POM), and the house of polymethylmethacrylate (PMMA). Both are rigid materials, and it appeared that we had to demand small tolerances to both the rod and seat for proper sealing. It is probably not impossible to realize a valve in polymers with a high E-module, but we chose to substitute the seat material with a flexible incompressible rubber. A few examples of valves in hard materials are the fairly small PEEK-valves (polyetheretherketone) produced by Upchurch [44], and rather large ceramic valves known from conventional plumping. In the latter case a lubricating and sealing grease is required.

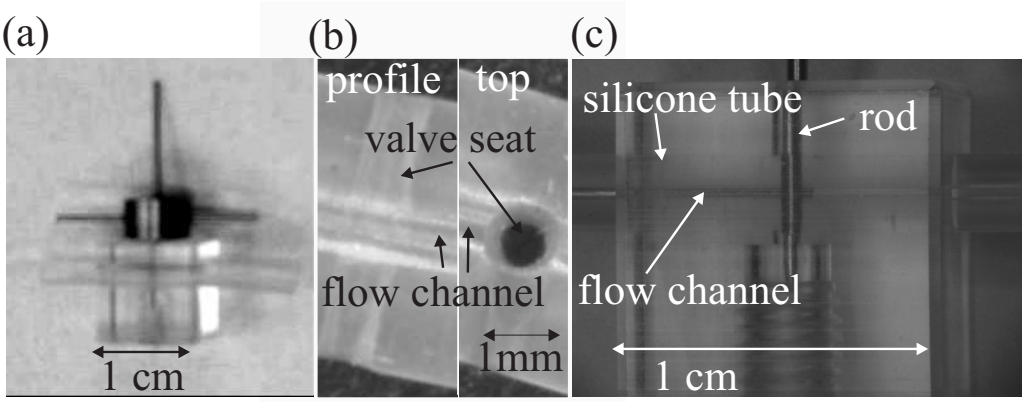

Figure 6.1: Pictures of the punched rod valve. The punched rod valve consists of a transparent PMMA-box with a drilled channel cross. The horizontal channel contains a silicone rubber tube, and the vertical channel contains a rod with a through going hole to open and close for a liquid flow. A pre-made channel is punched in the tube, in order to provide a valve seat for the rod. (a): The punched rod valve. (b) A profile and top view on silicone tube. The flow channel and valve seat is indicated on the figures. Sealing properties are very sensitive to the centering of the valve seat in the flow channel. (c): Magnification of the punched rod valve seal. Silicone tube, rod, and flow channel is indicated on the figure.

Valve type	Rod diameter 10^{-4} m	Rod chan. diam. 10^{-4} m	Flow chan. diam. 10^{-4} m	Rod seat diam. 10^{-4} m	Act. energy 10^{-3} J	Threshold pressure 10^{5} Pa
Punched rod valve	9.9 ± 0.1	5 ± 0.2	5.2 ± 0.1	3.2 ± 0.5	12 ± 5	Not detectable

Table 6.1: Parameters and performance of the punched rod valve.

Fig. 6.1 is a picture of the rod valve and details of the critical parts. Panel (a) shows the valve consisting of a PMMA-box, with a drilled channel cross. The horizontal channel contains a silicone tube, and the vertical channel contains a rod. Panel (b) is a magnification of the valve seat, which is punched with a sharp needle. Panel (c) shows a magnification of the seal in an assembled valve. Parameters of the valve can be seen in Table 6.1.

Fig. 6.2 is a graphical presentation of the performance, which also is shown in Table 6.1, and the data is obtained using the flow setup and the balance based torque setup. Panel (a) shows the sealing property which is very poor, and no threshold pressure is detected. It is believed that exact centering of the rod is crucial to the performance, and it will therefore be necessary with a centering tool similar to the one used for membrane

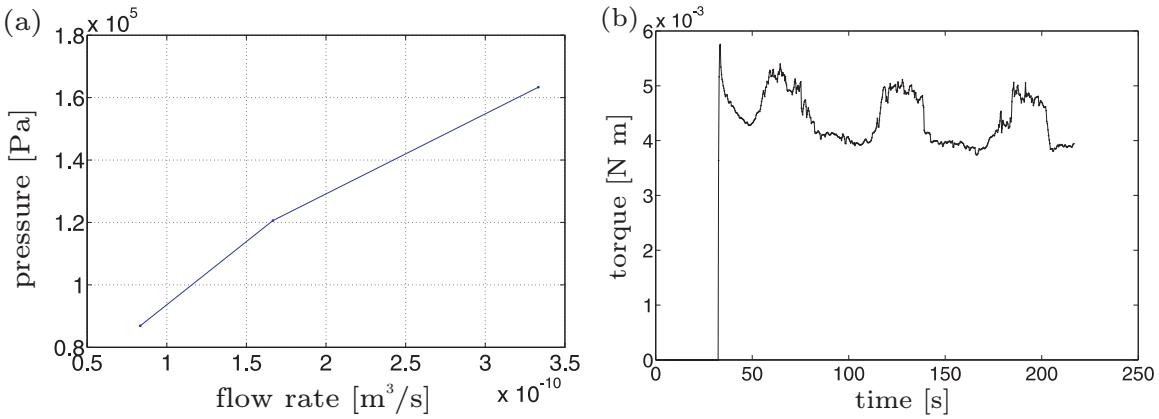

Figure 6.2: Measured flow property and torque: punched rod valve. Dimensions of the rod valve are seen in Table 6.1. (a): Pressure as a function of the steady state pumping flow rate Q_{pump}. This realization of the rod valve shows poor sealing properties, which is due to an improper alignment of the punched channel (valve seat), and the flow channel. In this case, it was not possible to detect a threshold pressure. Panel (b): friction torque as a function of time. The initial peak defines the maximum static friction torque, hereafter is seen the signal due to dynamic friction. The actuation energy based on the dynamic friction is $E_{act} = \tau\pi = 12 \pm 5$ mJ

preparation in Fig. 5.16. An other concern for the rod valve is the external support. If there is a small gap between outer tube wall and PMMA-housing, the rubber will be relatively easy to displace. Furthermore, compressed rubber under a high inlet pressure, may result in an axial expansion instead of building up a pressure seal. A FEM-simulation of this issue, could probably illuminate the problem. Panel (b) shows the friction properties measured at 1 rpm, and there appears to be a large periodic amplitude. The punched rod valve is good for prototyping, and especially if a better punching tool is developed. Even though down-scaling is possible with the small bore tube, we chose to proceed to the next step and get acquainted with molding processes.

6.2 The molded rod valve

We will now discuss construction, test and characterization of the molded valves. In analogy to the punched rod valve, we test sealing and friction properties. However, for the molded valve we will also investigate how these properties scale with the contact area.

Construction of demonstrators
To summarize our experiences on sealing, we know that it is necessary with a contact pressure in the sealing region, and an obvious way of creating it, is to use a large rod compared to the seat.

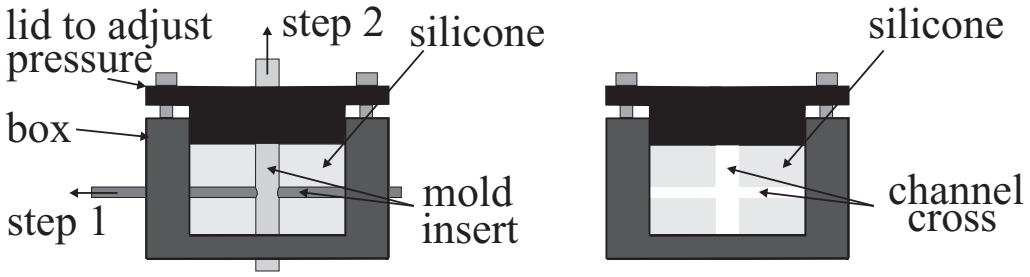

Figure 6.3: Sketch of the molding process for molded valve. A mold insert is formed by a vertical and a horizontal rod. The horizontal goes through the vertical rod, and the diameter is therefore smaller. When the silicone has cured the mold insert can be pulled out. On the sketch is also shown a lid to adjust the pressure on the seal.

The molded valves are produced by creating a mold insert, which on removal leaves a channel cross in the cured silicone rubber, as sketched in Fig. 6.3. There are two options to create a pressure seal with this geometry. The first is to insert a larger rod. The second, which we chose, is to leave the vertical rod (mold insert), and adjust the lid until the desired pressure seal is obtained. As silicone rubber is incompressible, we expect it to create a homogenous pressure on the rod. It is important to use a silicone rubber with little shrinkage, as the best sealing properties are obtained, when the rubber fils the box completely.

Fig. 6.4 shows pictures of the large and the small molded valve inserted in the flow setup, and 3D sketches are shown in Fig. 6.5. The valves are inserted in the flow setup and inlet and outlet ports are used for fluidic connection. The lever is used to turn the valve between open and closed states. Using the balance based torque setup, the lever can also be used to measure the torque, as the valve can be mounted directly to the torque setup as shown in Fig. 6.5. Valve parameters are listed in Table 6.2. For the large molded valve flat bottomed connection ports were used, which can result in leakage between the outer surface of the silicone plug, and the rigid wall. For the small molded valve, we used coned inlet ports with a capillary continuing into the silicone. In that way we ensured a perfect sealing connection.

On Fig. 6.5 is also shown the adjustable lid. The silicone was compressed to induce different pressures on the rod, by using a constant torque screwdriver. Due to the quan-

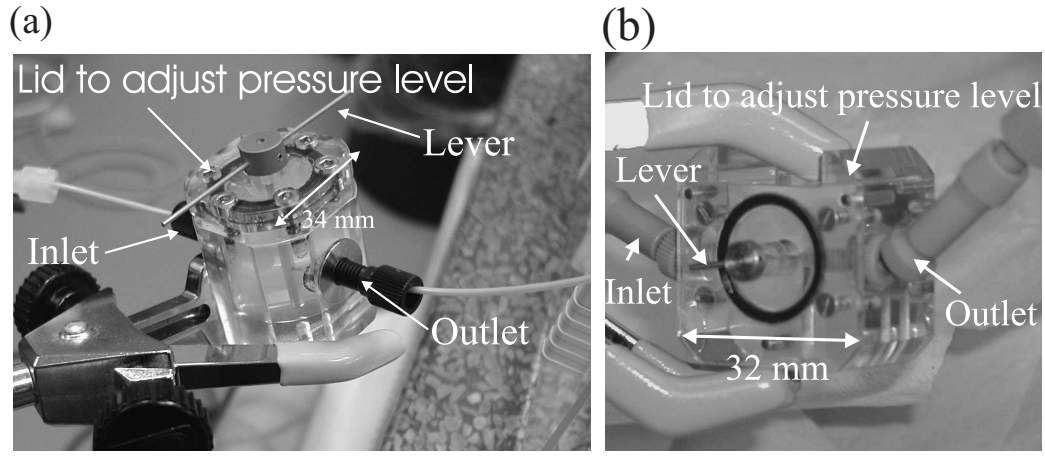

Figure 6.4: Pictures of the molded rod valves. Parameters of the molded valves are listed in Table 6.2. (a): Large molded valve. The lever is used to operate the valve and measure the friction torque. The lid can be adjusted to increase or decrease the pressure level. (b): Small valve. Small molded valve. Again, the lever is used to operate the valve, and the lid can be adjusted to make the appropriate pressure level.

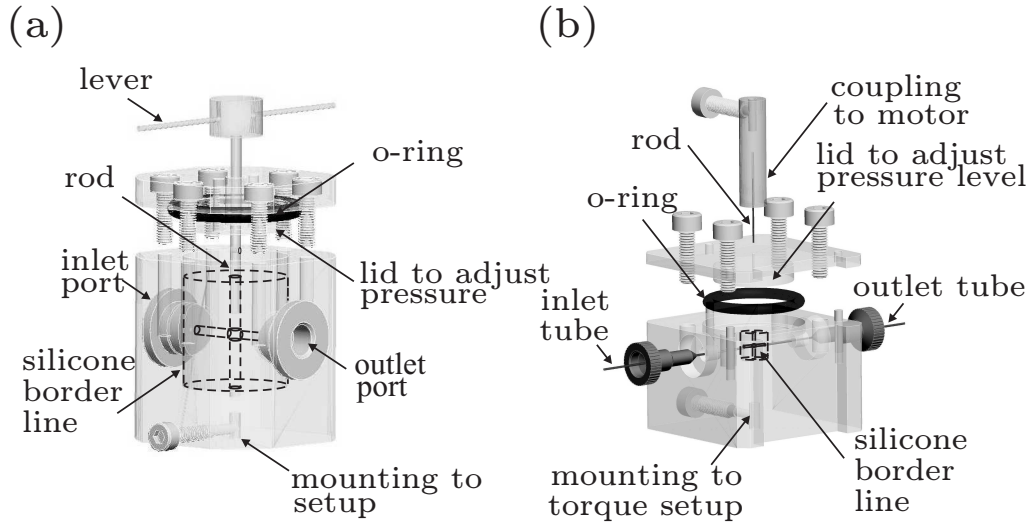

Figure 6.5: 3D drawings of molded turning valves. The silicone plug is indicated with a dashed line. (a) Large valve. Parameters for silicone plug: outer diameter 20 mm, height 23 mm. (b) Small valve. Parameters for silicone plug: outer diameter 5 mm, height 6 mm. On the figure is also seen a coupling to motor, which enables high-speed torque measurements the motor based torque setup. However, the coupling can be substituted with a lever, which also enables measurements with the balance based torque setup. Both torque setups are described in described in Chapter 5.

tification of the pressure utilized by the screwdriver, we will often refer to the pressure level as the torque level.

The mold insert for the large valve, was created in metal. However, when we down

Valve type	Rod diameter $10^{-4}m$	Rod chan. diam. $10^{-4}m$	Flow chan. diam. $10^{-4}m$	Rod seat. diam. $10^{-4}m$	Flow chan. length $10^{-3}m$
Lg. molded rod valve	19.9 ± 0.1	10 ± 0.2	9 ± 0.1	19.0 ± 0.2	19 ± 1
Sm. molded rod valve	2.5 ± 0.1	1 ± 0.2	0.65 ± 0.1	2.3 ± 0.1	3 ± 0.5

Table 6.2: Parameters of the molded rod valves. Actuation energy, threshold pressure, flow channel and rod seat diameter are all dependent on the the compression level, which is adjusted by tightening the lid.

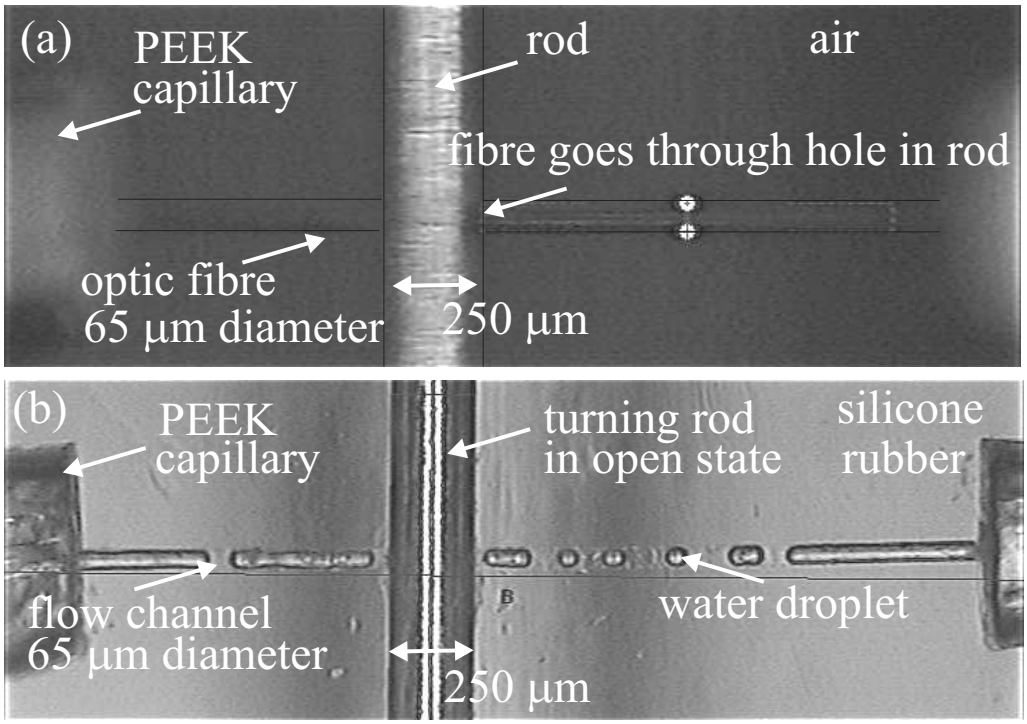

Figure 6.6: Pictures of channel cross in small molded valve.(a) Mold insert consisting of a rod, and a transverse fibre going through a hole in the rod. Air is surrounding the mold insert. The inner diameter of the PEEK capillary was 125 μm. (b) Liquid silicone rubber has filled the cavity, and after curing the optic fibre has been pulled out. Thereby, is created a flow channel, and the rod is now free to turn, and to open and close for a liquid flow. The PEEK capillary has, subsequently, been substituted with a large bore capillary to decrease flow resistance.

scale the system we have to think of alternative means, as steel wires below 200 μm are curled and too flexible. Fig. 6.6(a) shows the mold insert for the small valve. The vertical rod is a steel rod, where a 100 μm hole has been created with an Excimer laser [47]. The hole was aligned with two PEEK capillaries with an inner diameter on 125 μm. The

capillaries were threaded with a rigid optic fibre, and the fibre could afterwards be passed through the rod hole and into the receiving capillary. The cladding was not removed, as the fibre would need some strength to be pulled out after the molding process. It was also considered to connect the fibre to a laser and a sensor in order to ease the alignment of rod hole and capillaries, but it showed not to be necessary in this case. In panel (b) the fibre has been removed, and a flow channel with small water droplets is seen on the picture. The PEEK capillaries have been substituted with two large bore capillaries in order to decrease the flow resistance.

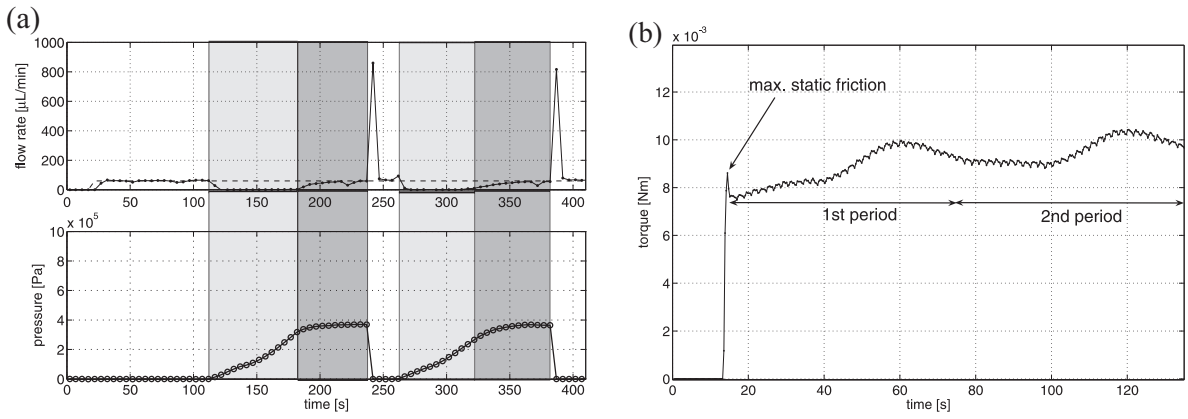

Figure 6.7: Sealing properties of the large molded rod valve at torque level 2. (a): The flow rate as a function of time. The dashed line indicates the flow into the valve Q_{pump} and the solid line the flow entering the balance Q_{bal}. The lower figure shows the corresponding pressure. The white zones are indicating periods with an open valve, and in gray zones the valve is closed. In the dark gray zones, the valve is closed, but the pressure seal is broken. Consequently, liquid is flowing through the seal, and reaches a steady state, which is observed as $Q_{\mathrm{bal}} = Q_{\mathrm{pump}} = 60\ \mu\mathrm{L\,min}^{-1}$. The threshold pressure is approximately 2.5×10^5 Pa. It is noted that Q_{bal} peaks, when the valve goes from closed to open. This is expected as there has been an accumulation and a pressure build up upstream to the valve. (b): The corresponding torque to operate the valve at 1 rpm. Initially, the torque increases until it reaches the maximum static torque. Hereafter, the signal is showing the contribution form dynamic friction, which is sinusoidal due to asymmetry in the construction. The dynamic friction is shown for the first two periods, i.e., for two revolutions. The apparent drift in the signal is not explained at the moment.

Large molded valve: Sealing property and actuation energy

Fig. 6.7 shows performance of the large molded valve, at torque level 2, with respect to sealing and friction properties. The upper plot in panel (a) shows the flow rates and the lower graph shows the corresponding dynamic pressure p. Q_{bal} is indicated with a solid line and Q_{pump} is indicated with a dashed line. The experiment is started a zero flow rate, and after approximately 20 s Q_{pump} is increased to to 60 μL min^{-1}, and Q_{bal} follows up after 5 s delay. An increase in pressure is too small to be noted. Between the white and light gray zone, the valve is shut, Q_{bal} decreases to zero, and the pressure increases. Between the light gray and the dark gray zone, the pressure seal is broken, Q_{bal} increases

until it reaches a steady state and equals Q_{pump}. At the end of the dark gray zone, the valve is opened, and accumulated water flows out on the balance with a flow rate above 800 μL min^{-1}. The pressure drops instantly with the discharge.

After approximately 260 s the cycle is repeated and shows a good reproducibility. The threshold pressure for the large molded valve is 2.5×10^5 Pa at torque level 2. Panel (b) shows the two first periods of a torque measurement with the balance based torque setup. Initially, we observe a small static friction. However, after a half cycle the dynamic friction exceeds the static friction. There appears to be a trend of increasing dynamic torque, and we have at this point no explanation of the phenomena. However, using the first cycle at torque level 2, we obtain an actuation energy of $E_{\text{act}} = 31.9 \pm 0.3$ mJ

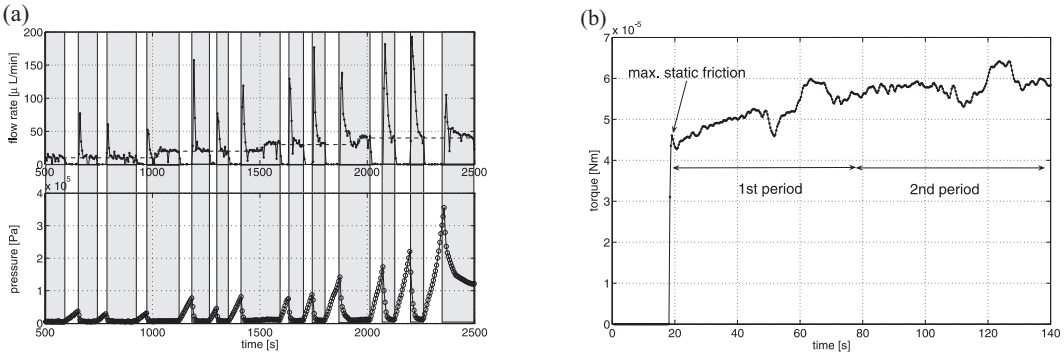

Figure 6.8: [Measured sealing properties and friction torque: small molded valve. (a): The upper graph shows the flow rate as a function of time at torque level 2. The dashed line indicates flow into the valve Q_{pump} and the solid line the flow through the valve Q_{bal}. If the two flow rates do not equal, there is either a leakage to the surroundings, an accumulation, or discharge of accumulated liquid. The lower figure shows the corresponding pressure. The valve is open in white and closed in gray zones. There was at no point a leakage through the seal and onto the balance. However, a leakage to the surroundings were observed at pressures above 2×10^5 Pa. At pressures below 2×10^5 Pa, the flow characteristics of the opening and closing cycle are reproducible. Whereas, the last cycle where the pressure reached 3.5×10^5 Pa showed a deviation from the desired characteristics. The channel was partly blocked on the return to the open state. The valve was operated with a position controlled motor. (b): The graph shows the torque to rotate the valve at torque level 0. The dynamic torque is shown for the first two periods, and the maximum static torque seems to be only slightly larger then the initial dynamic. The apparent drift is unexplained, but appears to be reproducible.

Small molded valve: Sealing property and actuation energy

Fig. 6.8 shows the sealing properties and friction for the small molded valve. Panel (a) shows Q_{pump} and Q_{bal} during the experiment. The small molded valve did not leak in the tested pressure range. The upper limit for the pressure sensor is 7×10^5 Pa, which means that the valve is sealing to to this pressure, at least. We will return to flow experiments in the discussion of Fig. 6.13. Fig. 6.8b shows the friction torque measured with the balance based torque setup. The actuation energy to open and close the valve is 0.15 $\pm$ 0.01 mJ.

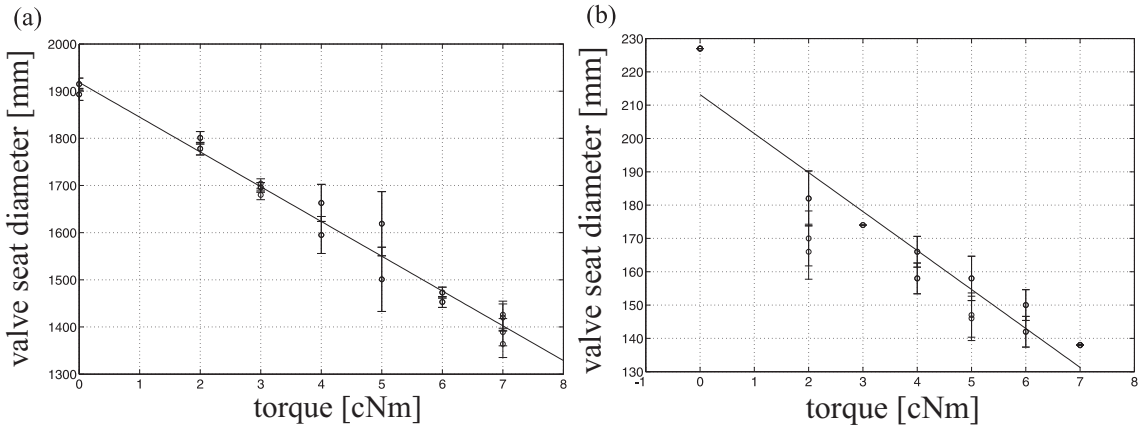

Figure 6.9: Valve seat diameter vs torque level: large and small molded valve. Errorbars represent standard deviations of the data points. (a): The large molded rod valve. Each torque level is represented by four data points, as we measured the diameter above and below the flow channel. In other words the data represent two measurement series of torque level adjustments. Only at high torque levels, level 7, there appeared to be a difference between upper and lower diameter. At torque level 4 and 5 there is a large difference between measurements from the two different series. However, a linear approximation is reasonable. The regression line intersects in 1920 μm and the slope is -74 μm cNm^{-1}. The mean value at zero torque level is 1900 μm. (b): The small molded rod valve. Torque level three is only represented by two data points from the same measurement series. All other torque levels are represented by 4 data points from two series. The valve seat diameter is decreased with increasing torque level, and although data fit poorly with a linear regression, we shall use it as a first approximation. The regression line intersects in 210 μm and the slope is -12 μm cNm^{-1}.The mean value at zero torque level is 230 μm.

Measurements on relation between torque level and deformation

Fig. 6.9(a) and (b) shows the relation between the valve seat diameter and the torque level for the large and the small molded valve, respectively. The torque level is adjusted with a constant torque screwdriver, and has the unit cN m referring to the torque level set on the screwdriver. The rod is pulled out of the seat in order to measure the diameter, but it has to be reinserted before the torque level is adjusted. Otherwise, the compressibility of the system is too large. For the large molded valve we have measured the diameter above and below the flow channel for two series of measurements. There is a fine linear relation between the diameter of the valve seat channel and the torque level. For the small molded valve the relation appears to be more complex, but wee shall approximate with a linear relation in the measured interval. During adjustments of the torque level it is important, that both the sleeves and the rod are inserted in the rubber, to keep a high degree of incompressibility. If not, we do not obtain a linear relation.

Friction torque vs torque level

Fig. 6.10(a) shows the first period of friction torque for different torque levels for the large molded valve. In panel (a), mean values of the friction torque are plotted as a function of the torque level. The largest contribution to the friction torque is obtained between torque level zero and two. Hereafter, there is only a minor increase in the torque. Panel (b) shows the measured torque vs torque level, with errorbars indicating standard deviations.

Friction torque vs torque level for the small molded valve is seen in Fig. 6.11. In panel (a) is shown the first dynamic period for different torque levels, and in panel (b) mean values with errorbars are plotted against the torque level. One measurement series shows a significant difference, which indicates that absolute control of the parameters is difficult. However, three measurements show the same trend, and we shall conclude that the torque is increasing with the torque level. The increase appears to cling off at torque level 5.

Flow and sealing property for different torque levels

Table 6.3 summarizes the flow properties for the two molded valves. At torque level 0 the large molded valve was leaking to both the surroundings and onto the balance. In both cases the hydraulic resistance was on the order of 10^{11} Pa s m^{-3}. At larger torque levels there was no observable leakage to the surroundings, and the threshold pressure increased. For the small molded valve we also observed a leakage at the lowest torque level, but never a leakage onto the balance.

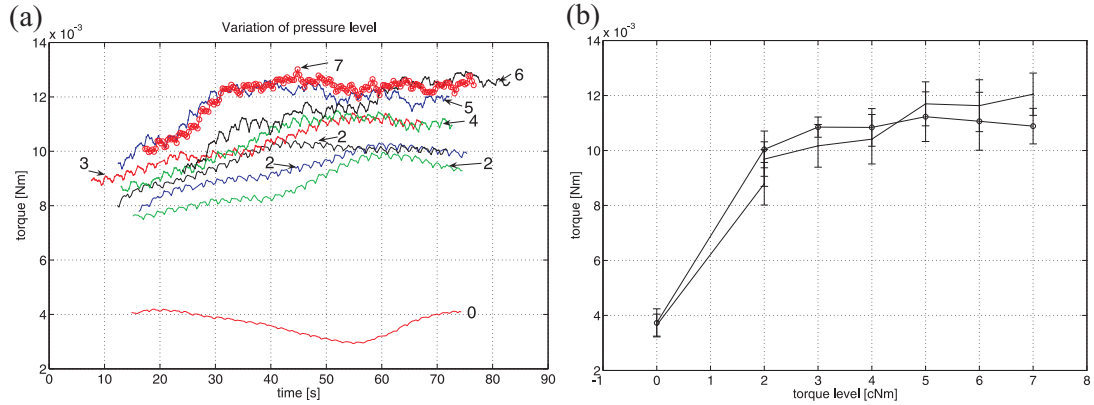

Figure 6.10: Friction torque for large molded valve at different torque levels. (a): The first period of the dynamic friction torque for different torque levels. (b): The dynamic friction torque as a function of torque level. Data points represent average values of the first dynamic period as seen in (a). The figure shows the result from two measurement series. The torque increases clearly with increased torque level. Colors on online version.

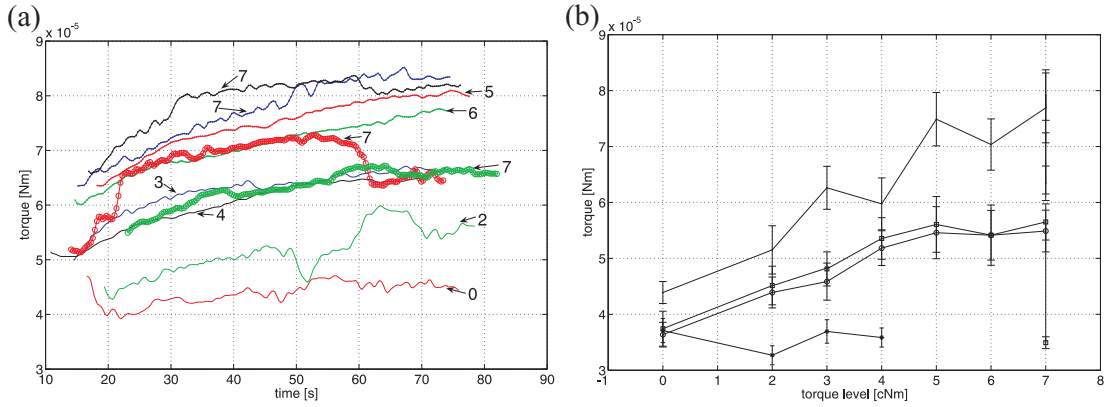

Figure 6.11: Friction torque for small molded valve at different torque levels. Panel (a): The first period of the dynamic friction torque for different torque levels. Panel (b). The dynamic friction torque as a function of torque level. Data points represent average values of the first dynamic period as seen in (a). The figure show results from four measurement series, where three of them clearly increases with increased torque level. The errorbars indicate standard deviations. Colors on online version.

Molded valve		Unit	Torque level 0	Torque level 2	Torque level 3	Torque level 4
Large	p_{th}	10^5 Pa	0	4.3 ± 0.9	6.7 ± 0.3	
	R_{open}	10^{11} Pa s m^{-3}	7.6 ± 0.6	11 ± 3	10 ± 4	
Small	p_{th}	10^5 Pa		> 7	> 7	> 7
	R_{open}	10^{13} Pa s m^{-3}		2.2 ± 0.2	6 ± 2	10 ± 1

Table 6.3: Mean values and standard deviation of threshold pressure and hydraulic resistances for the molded valves. The large molded valve was leaking to the surroundings at torque level 0, and the hydraulic resistance to surroundings and to the reservoir on the balance was on the same order. The small molded valve was also leaking to the surroundings at torque level 0, but there was no leakage onto the balance.

6.3 Direct measurements of actuation energy

So far we have separated the measurements of sealing and friction, and calculated the actuation energy based on the dynamic friction torque. We shall now make a direct measurement of the actuation energy, in a series of switching between open and closed states, and we will examine if the hydrodynamic pressure has an influence on the consumed energy.

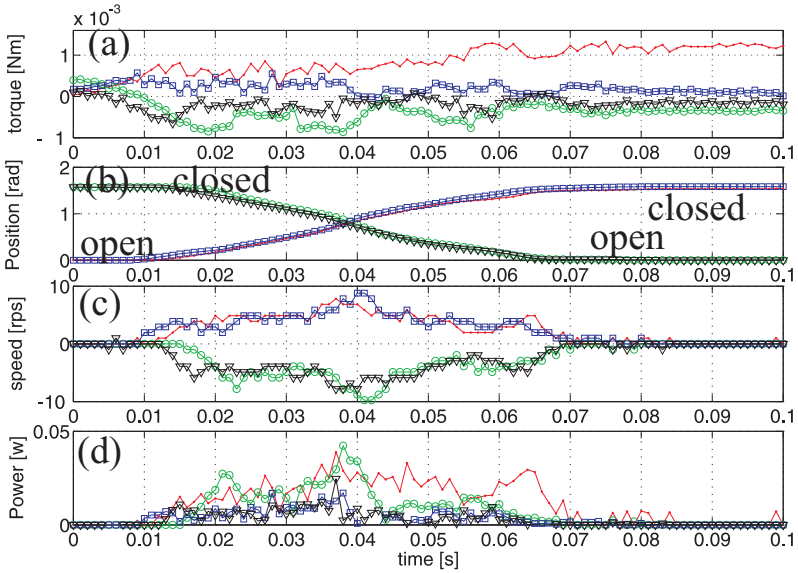

Figure 6.12: Measurements of motor parameters during opening and closing of the small molded rod valve at torque level 2. Markers and line colors: "· red", "∘ green", "□ blue", "▽ black" refer to the process of opening a valve, closing a valve, closing without load from rubber friction, and opening without load from rubber friction, respectively. (a): Measured torque. Even though the rotation has stopped after 0.07 s a large torque is still present. (b): Measured position of valve. At 0 the valve is open and at $\pi/2$ the valve is closed, it is noted that the new position is reached after 0.07 s. (c): Measured speed. Panel (d): Measured mechanical power which is the product of angular velocity and torque. Colors on online version.

Fig. 6.12 shows the data acquired from the motor, during the opening and closing of a valve. The figure also shows the measurements from a switching process, where the friction load has been removed. For high quality measurements, there should be a significant difference between the current from a loaded and an unloaded process. It appears that we are close to the lower limit of what we can measure. However, we have calibrated the motor against the balance based torque setup, in a similar torque range, and we can therefore estimate the error of the measurements. Panel (a) shows the torque, and the position given in radians are shown in panel (b). The speed n is plotted in panel (c), and the product of the angular velocity $\omega = 2\pi n$ and the torque gives the friction related power shown in panel (d). The actuation energy is calculated as an integration of the power.

Fig. 6.13 shows the corresponding measurements of flow properties and actuation en-

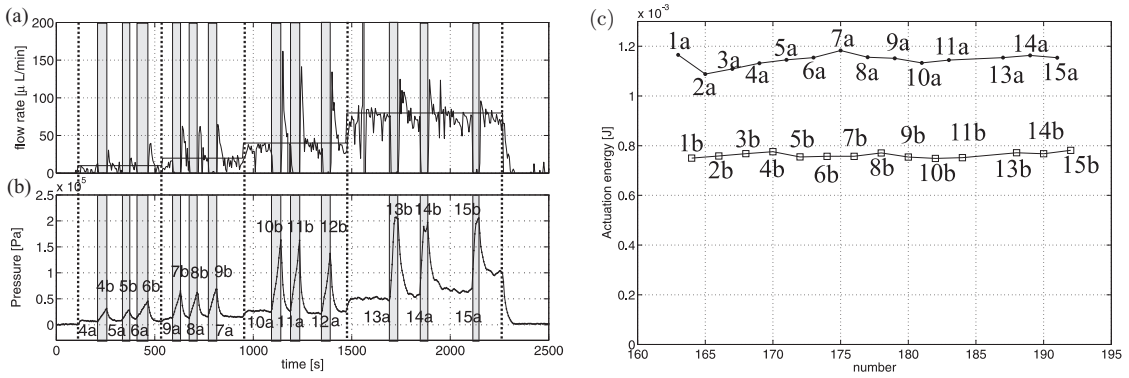

Figure 6.13: Direct measurements of sealing properties and actuation energy for the small molded valve at torque level 2. (a): Measurements of flow rate Q_{bal} (fluctuating solid line) and Q_{pump} (solid line), for several cycles of opening and closing the valve. Change of flow rate is indicated with horizontal dashed lines. The used flow rates for Q_{pump} are 10, 20, 40 and 80 μL min^{-1}. Gray areas indicate closed states and white areas indicate open states. (b): Measurements of pressures corresponding to measurements in (a). Between white and gray zones the valve is instantly (within 0.1 s) opened or closed. All edges are marked with a number and the letter "a" or "b", where "a" indicates that the valve is going from opened to closed state. (c): Actuation energies corresponding to the numbers in (a) and (b). The first three cycles are not observed on figure (a) and (b), as they were performed with zero flow rate, and in that case a pressure or flow rate change is not observable on (Q, p)-data. Actuation energies for open-to-closed state are systematically larger than the reversed process. This could be due to the control electronics, but it has not been further investigated.

ergy. In panel (a) the flow rates Q_{pump} and Q_{bal} are plotted with solid lines, where the latter is identified by its fluctuating nature. Change of flow rate is indicated with a vertical dashed line, and the corresponding dynamic pressures are shown in panel (b). It is noted that Q_{bal} is zero in all the gray areas, and the valve is therefore sealing. All processes of opening and closing the valve are denoted with a number and a letter, where "a" indicates the valve is closing and "b" that the valve is opening. "4a" is for example the first process of closing the valve at 10 μL min^{-1}, and the actuation energy is plotted in panel (c). One may think that the actuation energy would increase with the hydrodynamic pressure, but this is not observed.

Table 6.4 show the not calibrated and calibrated actuation energies for the closing process $E_{o\to c}$, the opening process $E_{c\to o}$, the closing process without load from rubber friction $E^0_{o\to c}$, and the opening process without load from rubber friction $E^0_{c\to o}$. The calibration is calculated according to Fig. 5.18(b). The total actuation of a cycle is the sum of opening and closing $E_{\mathrm{act}} = 1.36 \pm 0.03$ mJ. To compare we measured the friction torque, at torque level 2, with the balance based setup to $E_{\mathrm{act}} = 0.15 \pm 0.01$ mJ, i.e., an actuation energy 8.5 times lower. The speed was 1 rpm, and in the direct measurements we vary between 0 and 600 rpm. According to the measurements on velocity dependence this can contribute with a factor of 2, see Fig. 5.21. The remaining discrepancy may be explained within uncertainties, as we are at the limit of acceptable ratios between internal

	$E_{o\to c}$ mJ	$E_{c\to o}$ mJ	$E^0_{o\to c}$ mJ	$E^0_{c\to o}$ mJ
Not calibrated	1.14 ± 0.02	0.76 ± 0.01	0.3	0.3
Calibrated	0.80	0.562	0.2	0.2

Table 6.4: Direct motor based measurements of the actuation energy for the small molded valve at torque level 2. The calibrated data yields a smaller actuation energy, but the no load energy is contributing up to 35%, and for more precise measurements we would require a motor with less internal friction. The table contains processed data from experiments shown in Fig. 6.13(c).

friction in the motor and measured torque range.

6.4 Comparing model and experiments

Characterization of the turning microvalve was conducted using the microfluidic setup and the torque setup described in Chapter 5, respectively. The valve could be directly inserted to the flow setup using the inlet and outlet ports for fluidic connection. Also, using the drilled mounting channel shown in Fig. 6.5, the valve could be mounted in the torque setup letting the lever actuate the balance for torque measurements.

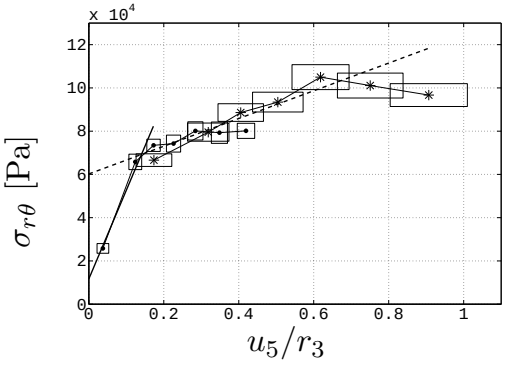

Figure 6.14: Friction stress for large "•" and small "∗" molded valve as a function of the displacement u_5/r_3. Data points represents mean values of one revolution, and boxes indicates uncertainties in two directions. The uncertainty for u_5 and r_3 is 30 and 10 μm for the large and small valve, respectively. The solid regression line fits the first three displacements for the large, hereafter the torque clings off and reaches a plateau. This plateau is consistent with measurements on the small valve. The dashed line is a fit to the data for the small molded valve. The elastic modulus k_m is calculated as the corresponding regression line divided by the friction coefficient η. k_m-values are listed in Table 6.5.

In Fig. 6.14 is shown the friction stress $\sigma_{r\theta}$ versus relative displacement u_5/r_3. The graph shows that friction scales with the nominal contact area of the valve, as the friction stress fits the same curve. The friction stress is shown as a function of the displacement u_5/r_3, where the symbols corresponds to the notation used for the torque model. The

friction increases linearly until $u_5/r_3 = 0.14$, hereafter it still increases linearly but more moderate. We shall refer to the conditions $u_5/r_3 < 0.14$ and $u_5/r_3 > 0.14$ as small and large displacements, respectively. From the linear fit we obtain the small displacements elastic modulus $k_m = 0.82$ MPa and the large displacement modulus $k_m = 0.13$ MPa, which leads to the following theoretical prediction for the friction stresses in a simple model for a turning valve.

$$\sigma_{r\theta} = \eta\sigma_{rr}, \tag{6.1a}$$

$$\sigma_{rr} = k_m \frac{u_1}{r_3} + p_0. \tag{6.1b}$$

A lower limit for the threshold pressure p_{th} is given by the modified plug seal equation

$$p_{\text{th}}^{\min} = k_m \frac{u_1}{r_3} + p_0. \tag{6.2}$$

	k_c	k_e MPa	k_m MPa	p_0 MPa	E MPa
tube	0.34	1.6		1.6	2.4 ± 0.3
membranes	0.26	2.5		0.92	3.7 ± 0.2
lg. valve/sm. disp.			0.82	0.023	1.5 ± 0.3
sm. valve/lg. disp.			0.13	0.12	1.5 ± 0.3

Table 6.5: Experimental obtained elastic moduli obtained (data fit). The friction coefficient was measured to $\eta = 0.5 \pm 0.1$, and for Poisons' ratio was used $\sigma = 0.49$. Parameters obtained from the large valve corresponds too small displacements with $u_5/r3 < 0.14$, and large displacement are obtained with the small valve ($u_5/r3 > 0.14$).

The results for the various elastic moduli for the plug setup, the torque setup and the turning valve have been summarized in Table 6.5. It must be noted that we cannot make a direct comparison of the moduli, as the boundary conditions have been changed. The silicone rubber in the turning valve is completely confined by a rigid wall, and can only expand into the flow channel. At large displacements the friction increased more moderately, indicating that we do not increase the contact pressure σ_{rr}, even though we increase u_5/r_3. A more thorough finite element analysis may reveal an instability due to buckling. However, such an analysis is not within the scope of this work.

In Table 6.6 it is seen that the experimental threshold pressure for the turning valves at $u_5/r_3 > 0.14$ are larger, than those obtained by the model calculation based on the plug seal. We can conclude that the turning valves are more efficient than expected, and this may be due to a self-sealing effect, i.e., the sealing pressure increases with the pressure across the valve. It is also noticed that the small valve is sealing even better than the large valve.

Displacement u_5/r_3	0.13	0.17	0.32
Large valve			
p^*_{th} [MPa]	0	0.18 ± 0.1	0.35 ± 0.2
$p^{\min}_{\text{th}}$ [MPa]	0.13	0.14	0.16
R^*_{open} [10^{11} Pa s m^{-3}]	7.6 ± 0.6	11 ± 3	10 ± 4
Rod diameter [mm]	1.99 ± 0.01	1.99 ± 0.01	1.99 ± 0.01
Contact length [mm]	23 ± 0.1	23 ± 0.1	23 ± 0.1
A_{nc}, contact area [μm^2]	144 ± 3	144 ± 3	144 ± 3
$\sigma_{r\theta}$, friction stress [MPa]	0.065 ± 0.005	0.071 ± 0.005	0.081 ± 0.005
τ, torque [mN m]	9.3 ± 0.1	10.2 ± 0.1	11.6 ± 0.1
E_{act}, contact area [mJ]	29.1 ± 0.3	31.9 ± 0.3	36.3 ± 0.3
Displacement u_5/r_3	0.32	0.41	0.50
Small valve			
p^*_{th} [MPa]	> 7	> 7	> 7
$p^{\min}_{\text{th}}$ [MPa]	0.16	0.17	0.19
R^*_{open} [10^{11} Pa s m^{-3}]	2.2 ± 0.2	6 ± 2	10 ± 1
rod diameter [μm]	250 ± 10	250 ± 10	250 ± 10
contact length [mm]	6 ± 0.5	6 ± 0.5	6 ± 0.5
A_{nc}, contact area [μm^2]	4.71 ± 0.02	4.71 ± 0.02	4.71 ± 0.02
$\sigma_{r\theta}$, friction stress [MPa]	0.081 ± 0.005	0.087 ± 0.005	0.093 ± 0.005
τ, torque [μN m]	47.6 ± 0.3	51.0 ± 0.3	54.5 ± 0.3
E_{act}, contact area [mJ]	0.15 ± 0.01	0.16 ± 0.01	0.17 ± 0.01

Table 6.6: Mean values and uncertainties of measured and calculated valve properties. * indicates measured value. The threshold pressure $p^{\min}_{\text{th}}$ is calculated from the simple plug-seal model using Eq. (6.2) and the values of k_m and p_0 for large and small displacements, as defined in Table 6.5. It is noticed that for $u_5/r_3 > 0.14$ the model prediction of threshold pressure is strongly underestimated. This is due the self sealing property of a valve, which is geometrically very different from a simple plug seal.

6.4.1 Experimental results on the actuation energy

The actuation energy E_{act} of the turning valve is an important parameter for designing portable microsystems. It is defined for one cycle of opening and closing as

$$E_{act} = \tau\pi, \tag{6.3}$$

where τ is the torque and π the turning angle in radians of two times a quarter-turn. If we desire a microvalve with say a threshold pressure of at least 0.35 MPa, we would according to Table 6.6 require a relative displacement of $u_5/r_3 = 0.32$. Using Fig. 6.14 and Eq. (6.1a) leads to a friction stress $\sigma_{rr} = 0.081$ MPa, and from that via the torque we calculate the actuation energy to be $E_{\text{act}} = 36$ mJ. This and the similar actuation energy $E_{\text{act}} = 0.15$ mJ for the small turning valve is listed in Table 6.6.

In Table 6.7 we also compare the obtained results with a typical check valve. As an example we have chosen the pre-stressed inlet check valve from a reciprocating micropump

	rod. diam. [μm]	contact length [μm]	nominal area [μm^2]	$\sigma^*_{r_\theta}$ [MPa]	E_{act} [mJ]
large valve	1990	23000	144	0.081	36
small valve	250	6000	4.76	0.081	0.15
	stroke volume [μL]	prestress [10^5 Pa]			E_{act} [mJ]
check valve	0.160	0.1			1.6×10^{-3}

Table 6.7: Comparing properties for turning and check valve. Actuation energy E_{act} and other parameters obtained from data fit. The friction coefficient was measured to $\eta = 0.5 \pm 0.1$, and for Poisons' ratio was used $\sigma = 0.49$. The friction stress is evaluated at $u_5/r_3 = 0.32$. The check valve is calculated on data from Ref. [14]

constructed by Maillefer *et al.* [14], and the actuation energy is calculated as the product of the stroke volume and the opening pressure. Disregarding viscous friction, it is noted that the check valve can be actuated approximately 94 times, for the amount of energy required by a turning microvalve. However, the turning valve provides a higher safety level, and it need not be activated while liquid is pumped through it in the open state. Which valve is the better one, depends obviously on the application. If the stroke volume is increased with a factor of 10 and requirements to the threshold pressure is increased with a factor of 10, the check and the turning valve would use the same amount of energy.

We have studied sealing and friction in microchannels, and have shown, for a given sealing, the friction force scales down linearly with the apparent contact area. Two turning valves constructed of similar materials and in different size, showed predicable threshold pressures, and a friction stress increasing linearly with the displacement. However, the increase is different between small and large displacements, which indicates an instability. We can, therefore, construct a low energy valve with a high pressure seal, by down scaling. Even though the principle of the turning valve is simple and well-known, we believe that this is the smallest realization of the valve to date.

This analysis is based on simple modelling, and important parameters for realistic operation conditions as temperature and fast actuation have been neglected. A more rigorous study on how these parameters influences the performance of the turning valve would be desirable, and necessary for true robust design.

6.5 Summary

We have in this chapter described the fabrication of punched and molded turning valves. For the molded valve we demonstrated by the construction of a large and micron-sized valve that actuation energy scaled linear with area. We also showed that actuation energy depends on contact pressure, but due to a more complex geometry, the dependency was not linear in the entire range.

The molded valves demonstrated excellent sealing properties, even for reasonable fric-

tion stresses, which is due to the self-sealing geometry. Depending on the application and safety level actuation energy of a turning microvalve, is comparable to passive check valves, which often is used in reciprocating pumps. However, further optimization of the friction stress may be possible by considering means to decrease the friction coefficient as discussed in Chapter 3.

In the next chapter we will discuss how the technology can be used to fabricate a reciprocating piston pump for drug delivery, and estimate the performance based on results from this chapter.

Chapter 7

Conclusion and outlook

We have in this thesis described a technology, where a soft rubber material and a hard smooth substrate has been used in the fabrication of microfluidic components, where sealing properties have been in focus. This focus is a consequence of the strong requirements to safety, which must be obeyed, if the technology should be used in applications for insulin delivery.

A portable delivery system is driven on a tight energy budget, and despite the strong demands to safety, the component needs to be energy efficient. We have fabricated and tested a microfluidic turning valve, and have shown that it, as promised, has excellent sealing properties, without a trade-off to increased actuation energy. The smallest valve, with a rod diameter of 250 μm is sealing to at least 0.7 MPa, with an actuation energy of 0.15 mJ. Although larger, the actuation energy is comparable to energy consumed in check valves guiding the liquid flow in a reciprocating pump. However, the turning valve provides a significantly larger safety level.

One of the key factors to success of microfluidic systems is integration, to obtain small compact devices with high functionality. Using findings from this thesis, we will sketch how to construct a pump, with the studied technology. The pump consists of two turning valves to rectify the flow generated by a reciprocating piston.

Piston pumps have according to Ref. [13] never been realized in micro scale. The following should, therefore, provide a sound basis before this area is explored. We shall make an estimate of energy consumption, robustness against back pressure, and free flow.

7.1 Low-leakage, low energy piston pump: integration

Fig. 7.1(a) is a 3D sketch of the pump consisting of two turning valves and a reciprocating piston. An inner casing tube is filled with a rubber lining, to provide a flow channel with good sealing properties. Three rods are pierced through the channel, and the pump

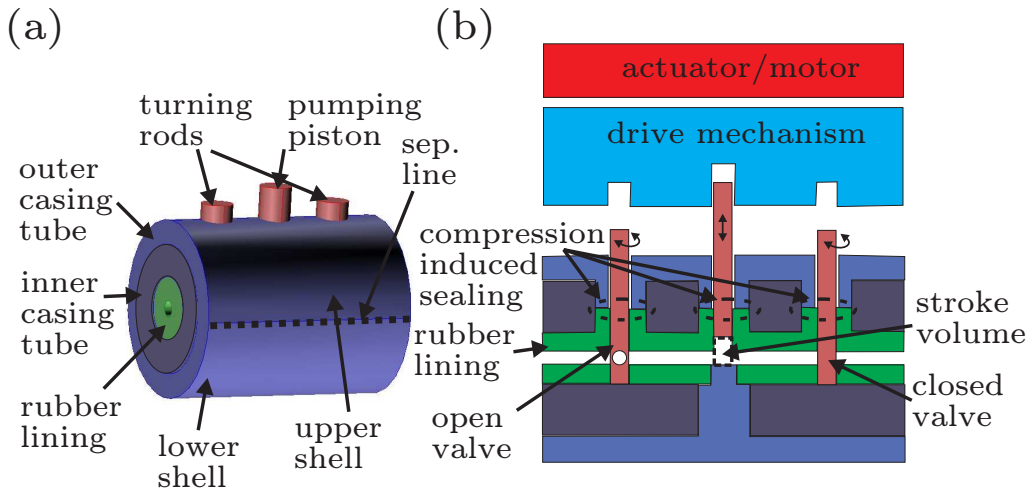

Figure 7.1: 3D sketch of piston pump, using low energy turning valves with high pressure seals. Integration of two valves and a pump chamber. (a) 3D sketch of the pump consisting of an inner tube casing with a rubber lining. An outer tube casing ensures compression to avoid leakage. The outer casing is assembled by an upper and lower shell. (b) Cross-section of pump. An actuator and a drive mechanism is also indicated on the figure. The drive mechanism should ensure a reciprocating movement of the piston, and quarter-turnings of the valves. The stroke volume is indicated with a rectangular dashed box. Interface from where compression is generated are indicated with dashed ellipses.

is surrounded by a rigid outer casing tube. The outer casing tube is an assembly of an upper and a lower shell. Panel (b) shows a cross section of the pump, with indications of a drive mechanism and an actuator module. When the outer casing tube is mounted it ensures compression, which is required to utilize the sealing properties of the otherwise too flexible silicone. Compression induced regions are indicated on the figure. When the piston reciprocates, it compresses the pump chamber in a periodic way. The valves are sequentially turned to ensure a forward flow, and no risk of free flow. The stroke volume is also indicated on the figure.

Fabrication process

Fig. 7.2 shows the envisioned fabrication process of the pump. In panel (a), an inner casing tube is assembled with two rods constituting the valves, a mold insert to create the pump chamber, and a horizontal rod is passed through all the vertical inserts. To ensure low friction, the vertical mold inserts should be fabricated in teflon, or an other material with low surface energy, as suggested in Ref.[39]. This will provide the lowest possible friction coefficient. In panel (b), liquid rubber is injected into the inner casing tube. After curing, the inserts are removed as shown in panel (c). This leaves a structure with a flow channel, a pump chamber, and two valves. Dashed ellipses indicate the region, where we can induce a compression to ensure sealing surfaces. The compression is induced, when a pressure is applied from the top. In panel (d), the pump piston is inserted, and the two shells of the outer casing tube is assembled with the rest of the pump.

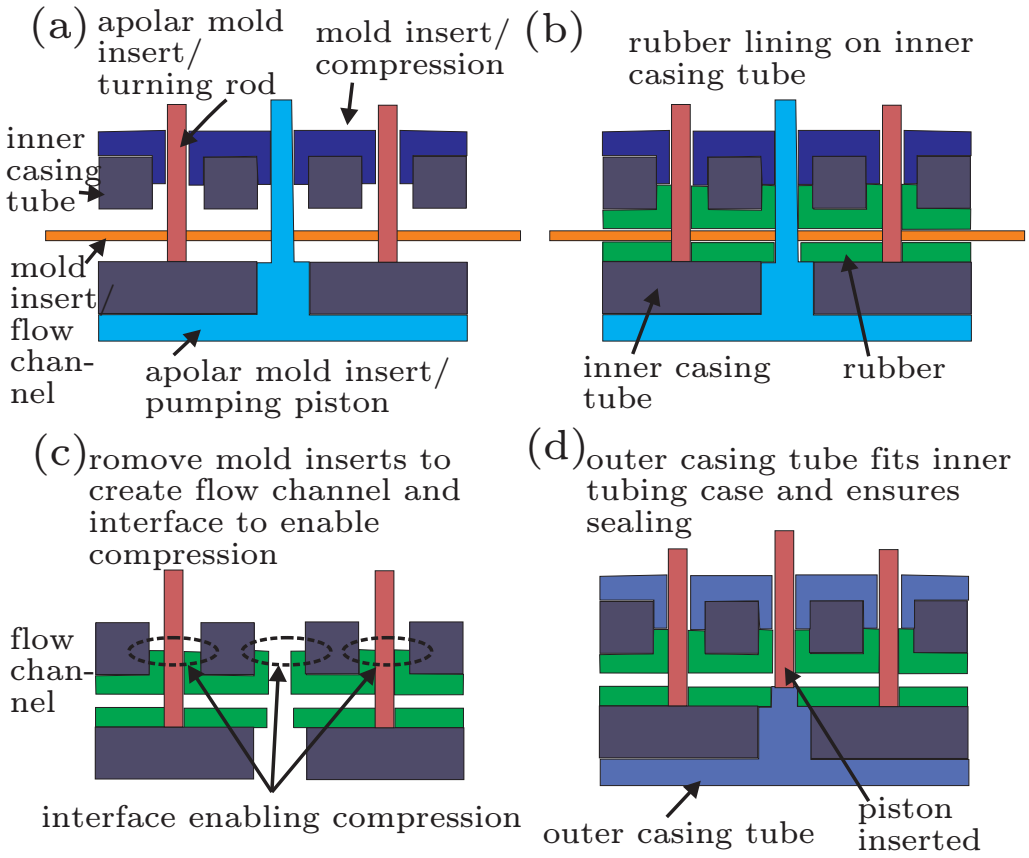

Figure 7.2: Illustration of molding process for piston pump using turning valves. (a) Inner casing tube with mold insert to create flow channel, two apolar mold inserts which are to be used as turning valves. An apolar mold insert to create the pump chamber, and an insert to enable compression is also shown. The two latter parts are surrounding the inner casing. Apolar mold inserts (low surface energy) ensures a low energy rubber surface, and, consequently, a low friction coefficient Ref. [39](b) A rubber lining is created by injecting liquid rubber into the inner casing. (c) Mold inserts are removed and leaves a flow cannel and a pump chamber. (d) The pumping piston is inserted and the upper and lower shell of the outer casing tube is pressed on.

Estimated performance

Table 7.1 is an estimate of energy consumption and sealing property of the pump. The estimate is based on findings in the experimental sections. It is noted that the major part (95%) of the energy is consumed by the reciprocating piston. Only 2.5% is dissipated in the valves, and an other 2.5% in the liquid flow. With an energy capacity on 58 J in the battery, as suggested in Table 2.1, we are able to pump 3.82 mL, which is more than a conventional insulin reservoir. However, we have not considered the energy consumption in actuator and drive mechanism. With a rough estimate, it would consume a similar amount of energy, and the concept does not appear feasible, as sketched here. Nevertheless, we cannot reject the feasibility of the technology, as there still is room for optimization.

	Quantity	No.	Eng./cyc.	Frac. of tot. eng.
Turning valve				
Rod diam. [μm]	250			
Contact length [mm]	6			
Contact area [μm^2]	4.71			
Friction stress ($p_{\text{th}} = 0.35$ MPa)	0.0810			
Torque [μN m]	47.7			
Actuation energy [mJ]	0.15	2	0.30	2.5%
Pump chamber				
Rod diam. [mm]	1			
Stroke length [mm]	1			
Stroke volume [μL]	0.79			
Max. contact length [mm]	6			
Max. contact area [μm^2]	18.8			
Max. friction stress ($p_{\text{th}} = 0.1$ MPa)	0.3			
Max. force [N]	5.7			
Max. actuation energy [mJ]	11.3	1	11.3	95%
Fluidic channels				
Cycle time [s]	0.4			
Flow rate [μL s^{-1}]	2.0			
Hyd. res. [10^{14} Pa s m^{-3}]	2			
Viscous eng. loss. [mJ]	0.31	1	0.31	2.5%
Total energy [mJ]			11.9	100%
Capacity of battery [J]	58			
No. of cycles	4870			
Pumped volume [mL]	3.82			100%

Table 7.1: Estimate of energy consumption and sealing property of pump illustrated in Fig. 7.1. The pump consists of two active turning valves to rectify the flow, and a pump chamber with a reciprocating piston. The components are made of a hard smooth substrate, and a soft silicone rubber. The rubber corresponds to Material 1 in Table A.1. The friction coefficient between sliding objects is $\eta = 0.5$. Using the specification of Table 2.1 we have a battery capacity of 58 J. If we neglect, energy consumption in the actuator and in other hardware, we would be able to run 4870 cycles and pump 3.82 mL or 382 units of insulin. Due to the chosen friction stress for the valves, the pump will be safe against free flow till 0.35 MPa. This result is obtained from characterization of the large molded valve. The small molded valve promises an even better sealing, for reasons that are not understood at the moment. Due to the choice of friction for the pump chamber, we can pump against 0.1 MPa without leakage. This results is obtained with the pull-force geometry and the plug-sealing experiment. According to Table 2.1 the pump should run in 10 s to deliver the maximum bolus flow rate, and deliver every 48 min to provide the minimum basal increment (or min. basal flow rate).

Optimization and concerns

In order to improve this system, research should be focused of minimizing the friction coefficient. An actuation force on 5 N is a strong demand to a linear actuator driven on a low voltage battery. Electromagnetic actuators are according to Ref. [22] very energy efficient and enables a fast time response. However, the delivered force is proportional to the current, which is limited by the energy source.

An other concern could be reduced accuracy in dosing due to the flexible silicone. If the silicone is not supported properly it will increase compliance of the system. A last concern is stiction between rubber and substrate.

Advantages of the pump

- High safety level against free flow
- Low energy consumption due to down-scaling, but probably not enough
- Simple and mature pumping principle

Disadvantages and issues

- Suitable actuators have to be explored or developed
- Compliance due to elastic material. Need to be minimized by ensuring that the incompressible rubber lining does not leave cavities and bubbles in the molding process.
- Will the rubber lining detach from the inner casing tube during operation
- Stiction between rubber and hard resting/sliding substrate could be an issue. Especially time effects would need to be studied
- Although demonstrators are possible, issues regarding high volume production need to be addressed in future project.

Robust design

High quality, low-cost devices is of major importance for commercial success, where high quality also means reliability and small variation in the performance. Robust design is a systematic method to minimize variation in a given device. The method has been used in many areas of engineering, but is rarely seen in literature on microfluidics. Taylor has illustrated how to minimize variation in a piston pump, where the flow rate is given by a parameterized expression, Ref [48]. A requirement for robust designing is knowledge on how the system responds to changes in design parameters and variations in the surroundings. Typically the design equation is established on basis of exploring experiments, where the considered parameters have been varied systematically.

In Ref. [6], we suggested how to use a finite element tool in the design phase, in order to minimize the variation in flow rate for a simple piston pump. However, the example is far from realistic and should only illustrate the principles of the idea. True design using a finite element solver, would also require the development of a very efficient minimization algorithm, in order to analyze more realistic geometries.

In this thesis we have been concerned with understanding and modeling of parameter influence. Such equations can of course also be used as a model equation for robust design. However, we will leave this topic just by drawing attention to that this systematic design tool can be explored, when we can control and model the parameter influence.

7.2 Conclusion

We have investigated a technology for engineering of microfluidic components which promises good sealing properties. A good sealing property is a way to ensure a high safety level for applications in drug delivery.

One of the major benefits of down-scaling mechanical systems is less energy consuming devices, and we have shown that such savings also are feasible with respect to performance governed by friction between rubber and a hard substrate. In particular, we have demonstrated this achievement by constructing and testing a turning microvalve.

We have also used the studied technology to suggest the construction of a pump in an unexplored branch of micropumps. Namely, the construction of a reciprocating piston pump, Ref. [13]. The pump utilizes the turning microvalves to rectify the fluid flow, instead of the conventional passive check valves. For a limited amount of actuation force, the turning valve provides a significantly larger safety level than a check valve. It is believed that it is realistic to construct demonstrators of this pump in a true micro-scale. Further optimization of the friction processes appears necessary, but at this point we have only minimized energy by down-scaling. Furthermore, the suggested pump design should only serve as an example, and several parameters may be changed in order to obtain a feasible demonstrator. Knowing how the system responds to changes in design parameters and variations in the surroundings, the design could be optimized using the method of robust design.

Appendix A

Rubber and tribo-test parameters

This appendix contains additional information on the mechanical properties of the used silicone Table A.1. Table A.2 show parameters for the tribo-test setup.

Name	Unit	Small bore tube	Large bore tube	Material 1	Material 2
Use/characteristics		Tube	Tube	Mold	Sheet
Poisson's ratio		0.49	0.49	0.49	0.49
E-module (tangent) (0-50%) low velocity	MPa	1.7 ±0.2	1.6 ±0.2	1.0 ±0.1	2.0 ±0.1
E-module (tangent) (0-50%) high velocity	MPa	1.9 ±0.0	2.2 ±0.0	1.0 ±0.1	2.2 ±0.0
E-module (tangent) (0-5%) low velocity	MPa	3.0 ±0.3	2.2 ±0.3	1.4 ±0.2	2.9 ±0.1
E-module (tangent) (0-5%) high velocity	MPa	3.1 ±0.2	2.5 ±0.1	1.2 ±0.2	3.0 ±0.2
E-module (Young's) (0-5%) low velocity	MPa	2.4 ±0.3	2.4 ±0.3	1.5 ±0.3	3.7 ±0.2
E-module (Young's) (0-5%) high velocity	MPa	4.4 ±0.9	3.0 ±0.4	1.5 ±0, 3	4.6 ±0.2
Shore 'A'		50	50	40	60
E-module (Young's) conversion table	MPa	2.2	2.2	1.5	4.45

Table A.1: Material properties and their use or characteristics for the four different silicone rubbers. Tangent E-module is defined as $E = d\sigma_{rr}/d[(L_1 - L_0)/L_0]$, where L_1 is the final length, L_0 the initial length, and σ_{rr} is the pull stress. Young's module is defined as $E = \sigma_{rr}/[(L_1 - L_0)/L_0]$, where L_1 still is the final length, but it has to be within the linear range. Young's E-module is larger than the tangent E-module, as the tangent decreases with the deformation.In Ref. [49] is given a conversion table between IRHD hardness and Young's module. The IRHD-hardness is comparable related to Shore 'A' values for some materials. Except for Mat 1 with the highest Shore A value there is a fairly good agreement. The E-module were measured at a low(5×10^{-3} m min^{-1}), and a high velocity 1×10^{-1} m min^{-1}. Up to 40 % larger values appear for high velocity measurements. The liquid silicone mold had a shrunk less than 0.1 % after curing.

	Roughness Ra in grinding dir.	Roughness Ra normal to grinding dir.	Inner diam 10^{-2} m	Outer diam. 10^{-2} m	Contact area 10^{-4} m^2
Fine metal surface	0.55	0.85			
Rough metal surface	0.6	1.5			
Rubber ring			1.1	2.85	5.43

Table A.2: The rubber rings are constructed of Material 1 in Table A.1.

Appendix B

Work presented at MicroTAS-2004

Title
Minimization of performance variations in microfluidic components using the method of robust design

Authors
Lennart Bitsch, Henrik Bruus, and Jörg P. Kutter

Reference
MicroTAS-2004, Malmö, Sweden, September 2004, proc. vol. 1, p. 572-574.

Topic No. 1.4 Fluid mechanics and modelling
Poster

Minimization of performance variations in microfluidic components using the method of robust design

Lennart Bitsch[†*], Henrik Bruus[*], and Jörg P. Kutter[*]
[†]Novo Nordisk A/S, Brennum Park, DK-3400 Hilleroed, Denmark
[*]MIC - Department of Micro and Nanotechnology,
Technical University of Denmark, DK-2800 Kongens Lyngby, Denmark

Topics: **Microfluidics, modelling, robust design, finite element method, optimization**

Robust design is a systematic method to minimize variation in a given device. The method has been used in many areas of engineering, but is rarely applied in microfluidics. Taylor has illustrated how to minimize variation in a piston pump, where the flow rate is given by a parameterized expression [1]. A requirement for robust designing is knowledge on how the system responds to changes in design parameters and variations in the surroundings. We analyze the response numerically utilizing the strength of the recently developed multiphysics software FEMLAB.

A finite element model of a simple piston pump was set up in FEMLAB 2.3. The sketch of the pump along with a contour plot of the distributed pressure is shown in Fig. 1(a). To simplify the calculations we have chosen a design of limited complexity with only three design variables, the pressure from the piston P, and the heights, $h1$ and $h2$, of the inlet and outlet channel, respectively (also shown in Fig. 1(a)). We model the pump for a given position of the piston during a pump stroke.

Let us assume we require a target flow rate Q_{T} for a given position of the piston, and that the design variables are limited between lower and upper boundaries. Different sets of design variables can satisfy this condition, but we need to find the set with the smallest variance σ_Q^2 on the flow rate. The variance can be calculated by error propagation

$$\sigma_Q^2 = \sum_{i=1}^{N} \left(\frac{\partial Q}{\partial X_i} \right)^2 \sigma_i^2, \tag{1}$$

where Q is the flow rate, X_i is the ith design variable, σ_i is the standard deviation of X_i, and N is the number of design variables. It is noted that second order derivatives are ignored. In other words, in order to perform the analysis we need a mathematical model, but also information on uncertainties from the fabrication process.

The three design variables are allowed to vary within specified intervals. The lower boundaries are : 0.1 pascal for P, and 10 μm for $h1$ and $h2$. Similarly, we define the upper boundaries as 10 pascal, and 100 μm. In the example shown here, the standard deviations are equaled to the the lower boundary values. Besides minimizing variation, we need to satisfy the constraint $Q = Q_{\mathrm{T}}$. For the optimization we used the built-in matlab function *fmincon*, which minimizes the variance σ_Q^2 in Eq. (1). Apparently, the variance has different local minima, as seen in Table 1, but it is also clear that optimization makes a difference. This is seen as the relative standard deviation $s_Q = \sigma_Q \, Q_{\mathrm{T}}^{-1}$ is reduced from 79% to 9%. The second optimized design is the one represented in Fig. 1(a). Typically, the interval of the so-called $6\sigma_q$ product tolerance should be defined of some *a priori* specified limits, LSL and USL. This is illustrated in Fig 1(b) using the variance from the second optimization in Table 1. It is noted that if the $6\sigma_q$ product tolerance should fit within the limits, the standard deviations of the design variables need to be smaller, as we have already minimized contributions from the partial derivatives in (Eq. 1).

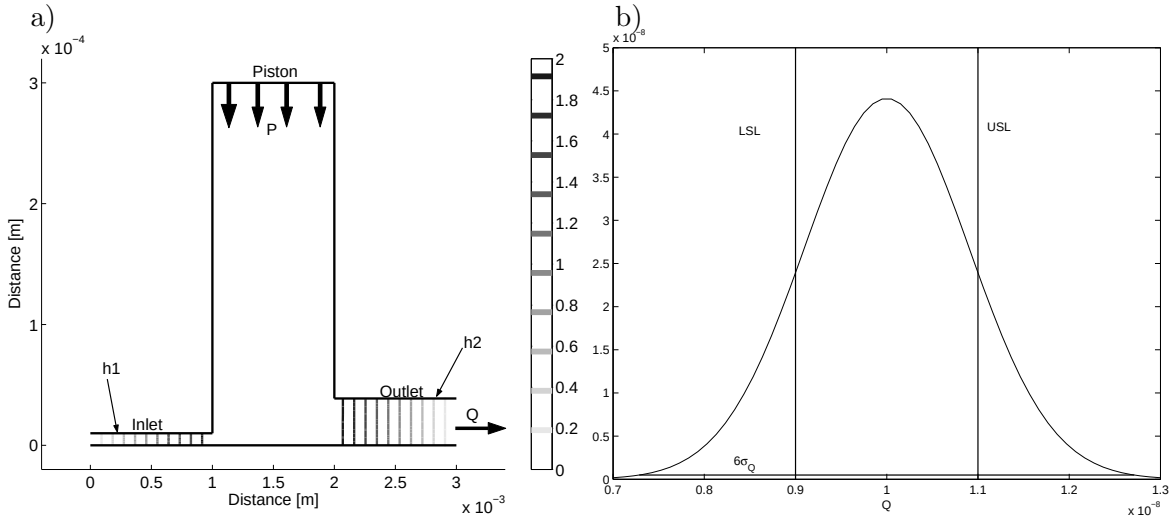

Figure 1: Panel a) A simple representation of a piston pump. The pump is being optimized at a specific time, when the piston is pumping. The three design variables P, $h1$, and $h2$, and the flow rate Q are also shown. The pressure contour lines illustrate that the pressure drop occurs only at the inlet and outlet. The pressure within the pump chamber is almost constant. Panel b) A gaussian distribution using the standard deviation of the second design from Table 1. LSL and USL indicate the lower and upper specification limits for the flow rate. Here, the limits are defined as $\pm 10\%$ of the target flow rate Q_{T}. The horizontal line indicates the interval of the $6\sigma_Q$ product tolerance, and it is larger than the specified limits.

	P [Pa]	$h1$ [μm]	$h2$ [μm]	Q [$\mathrm{m^2\,s^{-1}}$]**	s_Q
Not optimized	0.1 ± 0.1	10 ± 1	100 ± 1	1.00×10^{-8}	79%
Optimization 1	0.3 ± 0.1	10 ± 1	71 ± 1	1.00×10^{-8}	31%
Optimization 2	2.1 ± 0.1	10 ± 1	39 ± 1	1.00×10^{-8}	9.0%

Table 1: Three designs with the target flow rate $Q_{\mathrm{T}} = 10^{-8}$ [$\mathrm{m^2\,s^{-1}}$]. This unit appears for flows in two dimensions. It is noted that the same flow rate can be obtained with different magnitudes of the relative standard deviation s_Q. Different optimizations are a result of different initial guesses.

References

[1] W.A. Taylor: SOCE News, The Society of Concurrent Engineering, Spring 1996 issue, p.1-6.

Appendix C

Paper submitted to J. Micromech. Microeng, 2006.

Title
Low-energy, turning microvalve with high-pressure seal: sealing and friction

Authors
Lennart Bitsch, Jörg P. Kutter, Torben Storgaard-Larsen, Henrik Bruus

Reference
JMM, (submitted 2006).

Low-energy, turning microvalve with high-pressure seals: scaling of friction

Lennart Bitsch[(1,2)], Jörg P. Kutter[(1)], Torben Storgaard-Larsen[(2)], Henrik Bruus[(1)]

[(1)]MIC – Department of Micro and Nanotechnology,
Technical University of Denmark, DTU Bldg. 345 East,
DK-2800 Kgs. Lyngby, Denmark
[(2)] Novo Nordisk A/S, Brennum Park, Hillerod, DK-3400, Denmark

E-mail: lbi@mic.dtu.dk

Abstract. We present the design, fabrication, test and scaling characteristics of a silicone-based turning microvalve. Opening and closing is managed by turning a steel rod, with a diameter of 250 μm. The actuation energy for opening and closing the valve is 0.15 mJ, and when closed the valve withstands pressures higher than 0.7 MPa. The valve design in combination with studies of the scaling behavior of friction and sealing shows the feasibility of low energy turning microvalves with a high-pressure seal. For an appropriate parameter range we show that the friction force scales linearly with the apparent contact area and with the relative radial displacement of the elastic channel walls. Finally, our results illustrate the necessity of parameter control in order to develop a robust valve with the benefits of down-scaling.

Submitted to: *J. Micromech. Microeng. 24 April 2006.*

PACS numbers: 46.55.+d,47.15.gm,47.15.Rq,81.40.Pq

1. Introduction

For a number of years it has been predicted that microfluidic systems would significantly contribute to commercial success in various fields. One such field is drug delivery for which micropumps have been under development ever since the late seventies [1] and up until today [2]. In a survey on the commercial opportunities of microfluidics, it was stated that one of the reasons for lacking or postponed success for applications in drug delivery was the immaturity of the technology [3]. One possible methodological approach to reach the required maturity level is *robust design*, which ensures optimal performance for a given range of parameters [4]. This well-established method, rarely used in microfluidics, does require predictability of the scaling behavior and parameter dependency. In the work presented here, we have chosen to focus on improving the performance of a microvalve by *model-based down-scaling*.

Furthermore, it has also been argued that the long development time of many microsystems is due to the mechanical properties of silicon, which for a long time has been the preferred material for microprocessing. However, as stated by Quake and Scherer [5], silicon is not the material most suitable for liquid handling, and the use of soft materials is going to have a tremendous impact on the commercialization of microfluics. Therefore, the valve design reported herein relies on *soft, polymer-based materials*, in particular silicone rubber.

Valves are essential components for proper flow control in microfluidic systems. Two properties are especially vital for a valve in a portable microsystem: a low energy consumption and a near perfect sealing in the closed state with a high threshold pressure before breakthrough occurs. Attempting to fulfill both these requirements at the same time constitutes the central design challenge for making such microvalves. It is readily appreciated for drug delivery systems that the sealing properties of the valves involved are crucial, as even a small leakage may have fatal consequences. Consequently, a reliable *active valve* to precisely control delivery is desirable.

For a valve design utilizing a microplug polymerized inside the channel, Hasselbrink *et al.* [6] have shown that static friction scales with the surface area and the normal force. The valves showed impressive sealing properties, but the in-channel polymerization proved cumbersome, and, furthermore, a better understanding of sliding friction in microstructures was required. The application of this technology in an active valve was shown in [7]. In the development of a so-called gate type valve, Frank *et al.* [8] focused on low leakage and low energy consumption. This particular type of valve shows good self-sealing properties, which means that an increased fluidic pressure increases the contact pressure and thus minimizes leakage. However, the rigid silicon used is not ideal for sealing purposes.

Here, we study a simple silicone-based turning (rotating) valve as sketched in Figure 1. It is chosen primarily for its simplicity, its low energy consumption, and its good sealing properties in the closed state. Energy is only consumed when the valve is switched between the open and the closed state. Moreover, energy consumption is

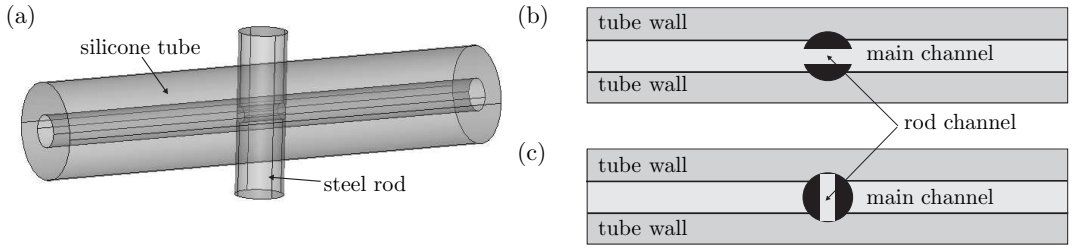

Figure 1. (a) Sketch of the turning microvalve with silicone walls and a steel rod. (b) The open state: the rod channel is parallel to the main channel. (c) The closed state: the rod channel is perpendicular to the main channel.

further reduced by down-scaling the valve, since, as shown in this work, friction scales with surface area. The valve has good sealing properties in terms of a high threshold pressure for breakthrough, due to the elasticity of the silicone rubber channel walls and because in the closed state the passageway through the steel rod is positioned perpendicular to the main channel.

The paper is organized as follows. In section 2 we study, as our first test system, the sealing properties of steel plugs in silicone microchannels and the related threshold pressures for leakage. In section 3 a second test system allows us to study friction of rotating steel rods in contact with pierced silicone membranes. In particular, we examine how the friction force behaves when scaling down. In section 4, we present the design, fabrication and experimental test results of the turning microvalve. Finally, a conclusion is presented in section 5.

2. The plug setup: sealing and threshold pressures in silicone channels

In this and the following section two experimental test setups for studying the basic sealing and friction properties of silicone-based microchannels are presented: the plug setup and the torque setup. These test setups have a high degree of similarity with the final turning valve, but due to their simpler geometry they allow for more clear-cut studies. In the experiments detailed below we have used linear flow velocities below 60 μm s^{-1}; all measurements were conducted at a constant temperature of 20 °C.

2.1. Theory and model for the plug setup

The sealing properties of silicone microchannels were studied using the plug setup sketched in Figure 2. A wide steel plug of radius R_1 is inserted in a more narrow liquid-filled silicone tube of initial inner radius r_1. As $R_1 > r_1$ the inner wall of the elastic tube near the plug is displaced by the distance u_1, so that the tube now exerts a uniform pressure on the rod. This seals the channel for liquid flow for moderate over-pressures Δp at the inlet. As the inlet over-pressure is gradually increased the inner wall of the tube expands, initially only in the part of the tube upstream from the plug. But, eventually, a certain threshold pressure p_{th} is reached where the tube also expands

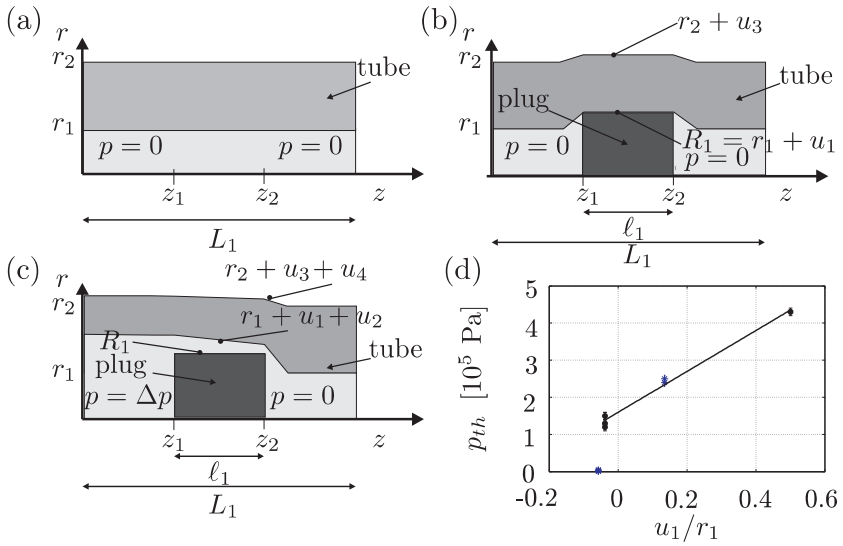

Figure 2. (a) Sketch of an axisymmetric elastic silicone tube (dark gray) of length L_1, inner radius r_1, and outer radius r_2. The tube is filled with water (light gray) at zero over-pressure $p = 0$. (b) The same tube after insertion of a wide steel plug of length ℓ_1 and radius $R_1 > r_1$. The plug causes displacements u_1 and u_3 of the inner and outer tube wall, respectively. (c) The inlet is pressurized to the over-pressure $p = \Delta p$ causing additional displacements u_2 and u_4 of the inner and outer tube wall, respectively. Note that Δp exceeds the threshold pressure, and the seal is leaking. (d) The measured threshold pressure p_{th} vs u_1/r_1. Data are fitted with a linear regression line.

around the plug, by the additional displacement $u_2 > 0$. When this happens the seal is broken and a leakage flow bypassing the plug arises, see Figure 2(c).

We shall derive a simple expression to estimate p_{th} and study its dependence on the relative deformation u_1/r_1. For simplicity, we consider a cylindrical tube, subjected to a uniform internal pressure p and zero external pressure. We assume further that there is no displacement in the axial direction. The expression for the threshold pressure is

$$p_{\text{th}} = k_c k_e \frac{u_1}{r_1} + p_0, \tag{1}$$

where k_c is an experimental correction factor, k_e is an elastic modulus, and p_0 is the residual normal pressure for zero deformation arising from adhesion forces, and boundary uncertainties. For the special case of tubes with a large relative width $(r_2 - r_1)/r_1$, it can be shown that $k_e = (2/3)E$, where E is Young's modulus. The discrepancy between this approximation and the numerical calculations is less than 1% for tubes used in these experiments. See reference [12] for a more detailed discussion of this approximation.

2.2. Experimental realization of the plug setup

To conduct experiments on the sealing properties and the threshold pressure, it is necessary to use a microfluidic measurement setup. The setup we employed is sketched in Figure 3. A syringe pump feeds liquid into the system at a constant flow rate, while

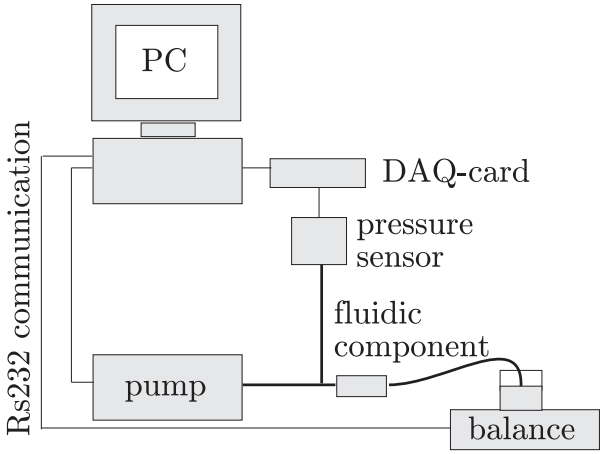

Figure 3. Sketch of the flow setup. A syringe pump forces liquid through the microfluidic component into a waste beaker placed on a balance. The inlet pressure is measured by a pressure sensor, while the outlet pressure is always atmospheric pressure. The PC sets the flow rate on the syringe pump and collects data from the electronic balance (through an RS232 interface) and from the inlet pressure sensor (through the DAQ-card). This setup was used for all flow measurements involving the plug-setup test geometries and the fluidic characterization of the turning valves.

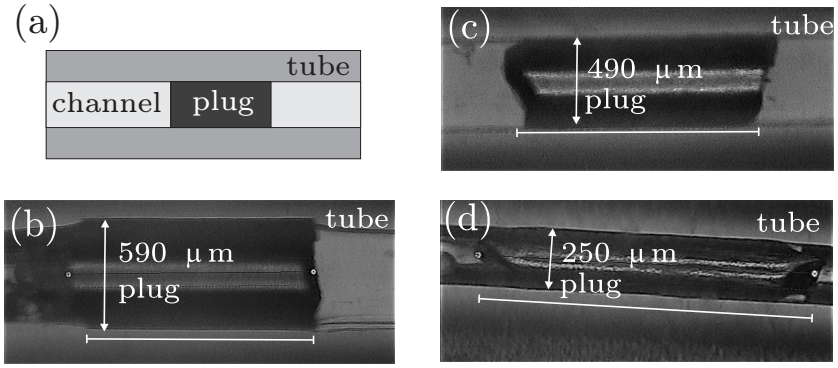

Figure 4. (a) Sketch of the plug-setup test geometry: a steel plug in an elastic silicone tube. (b) Microscope picture of one of the test geometries, a channel of diameter 520 μm containing a plug of diameter 590 μm. The horizontal white bar indicates the length of the plug. (c) as panel (b) but with channel diameter 520 μm and plug diameter 490 μm. (d) as panel (b) but with channel diameter 260 μm and plug diameter 250 μm.

a pressure sensor measures the dynamic pressure upstream of the flow component (e.g., the plug setup). The inlet flow rates are given by the pump, and the outlet flow rates are measured by collecting the effluent liquid in a waste beaker placed on a balance. For steady-state measurements without unaccounted for losses, these two flow rates should be equal.

tube	$2r_2$ [μm]	$2r_1$ [μm]	$2R_1$ [μm]	$2R_1$ [μm]
small bore	1200	260 ± 10	250 ± 10	390 ± 10
large bore	3700	520 ± 10	490 ± 10	590 ± 10

Table 1. Measured parameters for the four used plug setup geometries. For each of the two different tubes, characterized by the outer and inner diameter $2r_2$ and $2r_1$, respectively, two different plugs of diameter $2R_1$ have been employed.

2.3. Experimental results for the plug setup: sealing and threshold pressure

We have conducted 11 experiments with different plug setup test geometries. Three of these are shown in figure 4. All used combinations of tubes and plugs are listed in table 1.

In Figure 2(d) a plot of the eleven measured threshold pressures p_{th} as a function of the relative displacement u_1/r_1 for the different plug setup geometries is shown. An abrupt increase from zero to above 0.16 MPa in p_{th} is seen as u_1/r_1 increases above -0.04. For the most negative value of u_1/r_1, i.e., the plug is smaller than the lumen of the tube, the threshold pressure is clearly seen to be zero, while for the points around $u_1/r_1 = -0.04$ a non-zero threshold pressure is found. This indicates that there may be some uncertainty in determining when $u_1/r_1 = 0$. A linear fit through the data points for the three largest deformations yields $k_c = 0.34$ and $p_0 = 0.16$ MPa, which is a relatively high value.

We conclude that p_{th} is independent of the contact area of the pressure seal, but, after an initial sudden jump to above 0.16 MPa as u_1/r_1 becomes positive, scales linearly with the relative displacement u_1/r_1.

3. The torque setup: scaling properties of friction in silicone channels

In this section the sealing properties are studied using the so-called torque friction setup further described in subsections 3.1 and 3.2 below.

Many experiments on the subject of friction between hard substrates and rubber are conducted in order to understand the sliding between a rubber tire and asphalt. A modern understanding of sliding friction is reviewed by Persson *et al.* [9]. In this article they also describe an exact model for a quantitative prediction of rubber friction on hard and rough substrates. The model involves detailed knowledge on viscoelastic rubber models, surface roughness, and the authors emphasize the importance of including roughness on all length scales. The use of such a model is beyond the scope of this work, and we will therefore take a more empirical approach.

In contrast to friction between two hard substrates, rubber friction is mainly due to a bulk process, and is therefore related to the viscoelastic properties of the rubber [10]. During sliding, two processes can induce deformation and thereby internal friction in the rubber. These are adhesional forces and surface roughness, and for rough surfaces the adhesional contribution is reduced. Friction is, just like the viscoelastic properties,

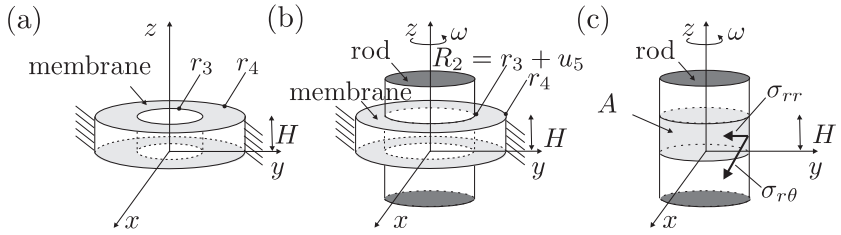

Figure 5. Sketch of the torque setup to study friction of a rotating steel rod piercing through an elastic silicone membrane. (a) A ring-shaped membrane of thickness H and inner and outer radius r_3 and r_4, respectively. The membrane is fixed at the outer radius. (b) After insertion of a rod of radius $R_2 > r_3$ the inner ring wall is displaced by u_5, and the rod rotates with angular velocity ω. (c) The friction stress $\sigma_{r\theta}$ and normal pressure σ_{rr} acting on the rod at the cylindrical contact area (light gray) between the membrane and the rod.

highly dependent on temperature. For high sliding velocities, the temperature increases on the contact interface. This is the so-called flash temperature, and its presence will make measurements difficult to interpret. Persson *et al.* have calculated the friction for a sliding rubber block on a fractal surface. Here, the flash temperature appears negligible below 100 μm s^{-1} [9].

When referring to the interface between sliding objects, one typically distinguishes between the nominal area and the area of real contact. The nominal area is the apparent area which is observed without magnification, and the area of real contact is the actual contact area between the microscopic surface asperities.

Due to a linearity between normal force and area of real contact, rubber friction is linearly dependent on the applied load. However, this is not true for very small loads, as friction does not decrease to zero at zero-limit due to adhesional forces. At very large loads there is an upper limit for the linearity between area of real contact and load [9, 11].

3.1. Theory and model for the torque setup

To analyze the scaling properties of friction between silicone and a steel rod, we employ the torque setup depicted in Figure 5. A ring-shaped elastic silicone membrane of thickness H and inner and outer radius r_3 and r_4, respectively, is fixed at the outer radius, see panel (a). A steel rod of radius $R_2 > r_3$ is inserted in the membrane hole thus displacing the inner ring wall by u_5, see panel (b). When the rod rotates relative to the silicone membrane with an angular velocity ω, it experiences a torque τ due to the friction forces acting on the cylindrical contact area between the rod and the membrane. The normal pressure σ_{rr} and the friction stress $\sigma_{r\theta}$ acting on the contact area, see panel (c), are modelled by standard expressions as

$$\sigma_{r\theta} = \eta \sigma_{rr} \tag{2}$$

$$\sigma_{rr} = k_c k_e \frac{u_5}{r_3} + p_0, \tag{3}$$

where η is the friction coefficient, k_e is an elastic modulus equal to $(2/3)E$ and k_c is an experimentally determined correction factor, analogous to the one appearing in equation (1).

3.2. Experimental realization of the torque setup

The experimental realization of the torque setup is shown in Figure 6. The core of the setup, shown in panel (b), consists of a horizontal steel rod piercing two vertically arranged silicone membranes. The rod can be made to turn by rotating the two silicone membranes, which are connected to a stepper motor via a PMMA housing. A thin lever is mounted on the rod perpendicular to the rod's axis, such that when the rod is rotated the lever presses down onto an aluminum block placed on an electronic balance, see panel (a). In steady-state the torque τ delivered by the friction forces between the rotating silicone membranes and the static rod equals the torque from the reaction force delivered by the aluminum block to the lever. The friction torque τ can thus be calculated as

$$\tau = m_{\mathrm{bal}} g \, L_{\mathrm{lev}} \cos\theta, \tag{4}$$

where L_{lev} is the length of the lever from the rod to the aluminum block, m_{bal} is the mass measured on the balance, θ is the angle between the lever and the surface of the aluminum block, and g is the gravitational acceleration. The scaling properties of this type of friction are then analyzed by studying the scaling properties of the friction stress $\sigma_{r\theta}$ given by

$$\sigma_{r\theta} = \frac{\tau}{R_2 A}, \tag{5}$$

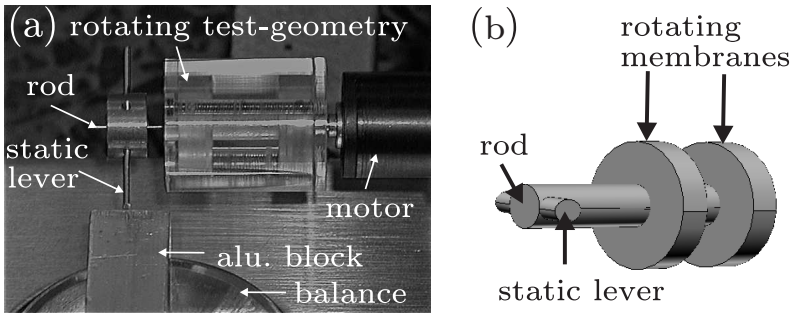

Figure 6. The balance-based torque setup and details on test geometry. (a) The torque test-geometry is fixed on the motor axle and rotates with a set speed. A rod is hanging in two membranes inside the geometry, and on the rod is mounted a lever that rests on an aluminum block. The aluminum block is positioned on a balance. When the membranes rotate in steady-state, friction induces a torque in the rod, and, consequently, a static force is acting on the aluminum block. This force is measured on the balance. (b) Inside the test-geometry the rod is suspended hanging in two membranes. The membranes rotate with the geometry, and the rod and lever are static.

Range of diameter of membrane holes [μm]	diameter of the rods [μm]			
small hole: $330 - 510$	250 ± 10	390 ± 10	490 ± 10	740 ± 10
large hole: $610 - 870$	490 ± 10	740 ± 10	990 ± 10	

Table 2. Measured parameters for the torque setup. The thickness of the membrane is $H = 1.0$ mm, and the outer membrane diameter is $2r_4 = 1$ cm. Note that a range is given for the diameters of the membranes holes.

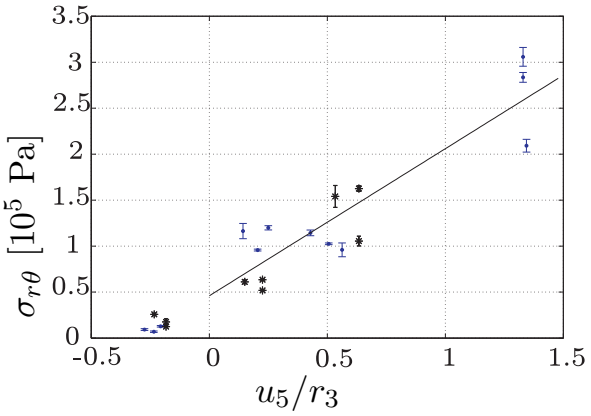

Figure 7. Friction stress "$\cdot$" for small and "$*$" for large membrane hole as a function of the displacement u_5/r_3, for different combinations of membrane hole and rod diameter given in table 2. Errorbars indicating standard deviations are shown for all data points. The solid line is a linear regression for positive displacements.

where A is the apparent contact area between the steel rod and the silicone membranes.

The geometry of the rotating housing shown in Figure 6(a) is fabricated in PMMA by drilling and milling processes. The silicone membranes shown in panel (b) are 1 mm thick and have an outer diameter of 10 mm. The holes in the membranes are made by a simple punching technique using a steel puncher. Two groups of hole diameters were fabricated, small ones of about 420 μm and large ones of about 740 μm. However, the punching technique does not result in very reproducible holes, which is why the hole diameters had to be measured individually. In table 2 the range of hole diameters as well as the rod diameters are listed.

3.3. Experimental results from the torque setup on scaling of friction

Figure 7 is the main result of the friction studies. It shows the friction stress $\sigma_{r\theta}$ as a function of the relative displacement u_5/r_3, for 25 different combinations of membrane holes and rod diameters listed in table 2. The data points are mean values obtained for one full revolution of the stepper motor. The graph shows that the friction stress depends linearly on the relative displacement u_5/r_3, but does not depend on the apparent contact area. In fact, the area varies by a factor of 4 from 3.1 to 12.4 μm^2 for the 25 measurements. Consequently, the friction force scales linearly with the area. The

regression line shown in figure 7 includes only the data point for positive u_5/r_3 values.

Using the slope and intercept of the regression line for $\sigma_{r\theta}$ versus u_5/r_3 together with equations (2) and (3), we obtain the correction factor $k_c = 0.26$ for the torque setup. This is in good agreement with the value $k_c = 0.34$ obtained for the plug setup, see section 2.3. The fact that the measured values of k_c are much smaller than unity can be explained by the difference in geometry and boundary conditions in the actual experiments compared to the simple theoretical model described section 3.1.

In conclusion, given the linear dependency of the friction stress and relative displacement, and the good agreement in the results for the elastic modulus $k_c k_e$ from the two different test setups, we find it acceptable to proceed using the model summarized in equations (1)–(3) to analyze the turning valve and predict its performance under down-scaling.

4. The turning microvalve

Having obtained a good understanding of the sealing and friction properties of steel rods in silicone microchannels, we now proceed with the design, fabrication and test of the turning microvalve.

4.1. Design and fabrication of the turning microvalve

To understand the sealing properties of a turning valve we can relate to the experiences made with both the plug setup and the torque setup and adjust those findings according to the boundary conditions imposed by the details of the turning valve design. For example, even though the turning rod displaces the inner channel wall in the same way the plug did in the plug setup, we would predict a higher threshold pressure as compared to a corresponding value of u_3/r_1 in the plug setup. The value will be higher since the outer wall is now supported and hence enhances a self sealing effect. The analogy to the friction properties of the torque setup is more straightforward, the main difference being that we now have a rod turning in a channel seat instead of a seat of two membrane holes turning around the rod. More subtle differences may arise from the fact that we now have only two edges instead of four.

Figure 8 is a 3D-drawing of the turning valve. The valve is constructed using conventional drilling, milling and molding processes. A cavity for the silicone rubber is fabricated in PMMA and is equipped with an adjustable lid. Dashed lines on the figure indicate the border of the silicone part which has been cured around a mold insert in the shape of a cross. The turning rod constitutes one part of the cross, while the other part is created by removing a smaller placeholder rod from the silicone after curing. This smaller rod assures the creation of a fluidic channel and it also keeps the bore in the larger rod free of silicone during the molding and curing process. After removal of the placeholder rod this leaves a channel for liquid flow, and a turning valve mechanism to control the flow. When the lid is tightened by means of screws it squeezes the silicone,

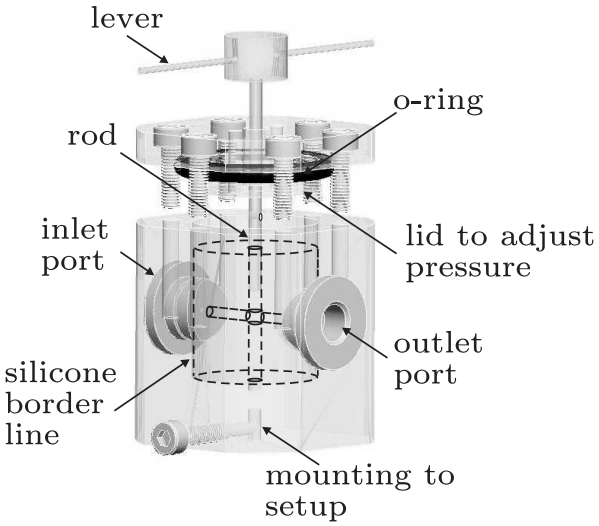

Figure 8. 3D drawing of the turning valve.

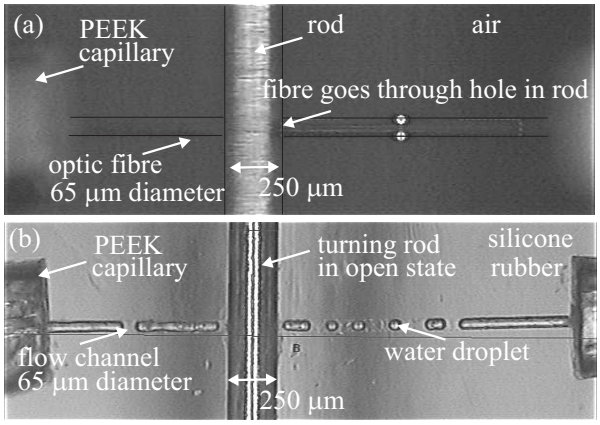

Figure 9. Construction of the channel crossing in a small molded valve. (a) Mold insert consisting of a rod, and a transverse fibre going through a hole in the rod and into a receiving PEEK capillary. Air is surrounding the mold insert. The inner diameter of the PEEK capillary is 125 μm. (b) Liquid silicone rubber has filled the cavity, and after curing the optical fibre has been pulled out. As a result a flow channel is created, and the rod can freely be turned to open and close for a liquid flow in this channel.

but due to its incompressible nature the rubber expands into the flow channel and the channel seat containing the turning rod. In that way, the contact force between the rod and the silicone is increased resulting in a larger threshold pressure. In order to control the normal force the screws in the lid were tightened with a constant-torque Allen wrench.

Two turning valves have been fabricated: a larger one with an outer rod diameter of 1990 μm and a rod channel diameter of 900 μm, and a small one with an outer rod diameter of 250 μm and a rod channel diameter of 65 μm. Figure 9 shows the molding process for the small molded valve. In this case, the mold insert for the flow channel is not a second rod but an optical fiber.

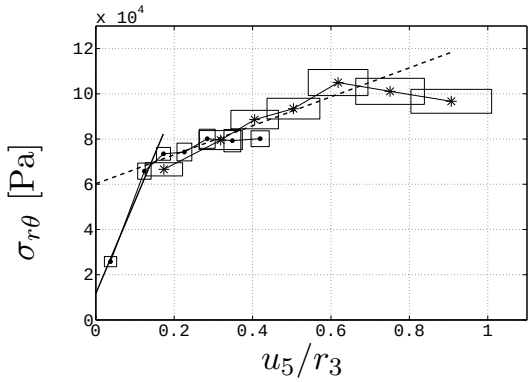

Figure 10. Friction stress for large "•" and small "∗" molded valves as a function of the displacement u_5/r_3. Data points represent mean values of one revolution, and boxes indicate uncertainties in both $\sigma_{r\theta}$ and u_5/r_3. For both the large and the small valve, the uncertainty for u_5 and r_3 is 30 and 10 μm, respectively. The solid regression line fits the first three displacements for the large valve, hereafter the torque clings off and reaches a plateau. This plateau is consistent with measurements on the small valve. The dashed line is a fit to the data for the small molded valve. The values of the elastic modulus k_m are listed in table 3 and calculated as the the corresponding regression line divided by the friction coefficient η.

4.2. Experimental results on friction and threshold pressure

The characterization of the turning microvalve was performed using the microfluidic setup and the torque setup as described in section 2.2 and 3.2, respectively. The valve could be directly incorporated into the flow setup using the inlet and outlet ports for fluidic connection. Also, using a drilled mounting channel shown in figure 8, the valve could be mounted in the torque setup allowing the lever to actuate the balance for torque measurements.

In figure 10 the friction stress $\sigma_{r\theta}$ is plotted versus the relative displacement u_5/r_3. Here we use the same notation as for the torque setup, and as in figure 7 we note that for the geometries of the various turning valves the friction stress does not depend on the contact area but only on the displacement. The friction stress increases linearly until $u_5/r_3 = 0.14$, hereafter it continues to increase linearly albeit at a much slower rate. We shall refer to the conditions $u_5/r_3 \leq 0.14$ and $u_5/r_3 > 0.14$ as small and large displacements, respectively. From the linear fits we obtain the elastic modulus for small displacements to $k_m = 0.82$ MPa and the modulus for large displacements to $k_m = 0.13$ MPa, which leads to the following expressions to theoretically predict friction stresses in a simple model for the turning valve,

$$\sigma_{r\theta} = \eta\sigma_{rr}, \tag{6}$$

$$\sigma_{rr} = k_m \frac{u_5}{r_3} + p_0. \tag{7}$$

A lower limit for the threshold pressure p_{th} is given by the plug seal equation

$$p_{\text{th}} = k_m \frac{R_2 - r_3}{r_3} + p_0. \tag{8}$$

	k_c	k_e MPa	k_m MPa	p_0 MPa	E MPa
tube	0.34	1.6		0.16	2.4 ± 0.3
membranes	0.26	2.5		0.092	3.7 ± 0.2
lg. valve			0.82	0.023	1.5 ± 0.3
sm. valve			0.13	0.12	1.5 ± 0.3

Table 3. Experimental determination of elastic moduli obtained from data fits. The friction coefficient was measured to $\eta = 0.5 \pm 0.1$, and for Poisson's ratio $\sigma = 0.49$ was used.

Displacement u_5/r_3	0.13	0.17	0.32	0.41	0.50
p_{th} [MPa], large valve	0	0.18 ± 0.1	0.35 ± 0.2		
p_{th} [MPa], small valve			> 0.7	> 0.7	> 0.7
p_{th} [MPa], model calc.	0.13	0.14	0.16	0.17	0.19

Table 4. Mean values and standard deviation of measured threshold pressure p_{th} for the large and small molded valves, and calculated p_{th} from the simple valve model using equation (8) and using the values of k_m and p_0 from the large turning valve for displacements $u_5/r_3 \leq 0.14$. For larger values of the displacement the model valve corresponds to the small valve. It is apparent that for $u_5/r_3 > 0.14$ the model predictions of the threshold pressure are strongly underestimated.

The results for the various elastic moduli for the plug setup, the torque setup and the turning valve are summarized in table 3. It must be noted that we cannot make a direct comparison of the moduli, as the boundary conditions are different. The silicone rubber in the turning valve is completely confined by a rigid wall, and can therefore only expand into the flow channel. For large displacements the friction stress increased more moderately, indicating that we cannot further increase the contact force σ_{rr}, even though we increase u_5/r_3. A more thorough finite element analysis may reveal instabilities due to buckling of the silicone. However, such an analysis is beyond the scope of this work.

From table 4 it is seen that the experimental threshold pressures for the turning valves at $u_5/r_3 > 0.14$ are larger than those obtained by the model calculation based on the plug seal. We can therefore conclude that the turning valves are more efficient than expected. This may be due to the self sealing effect of the particular geometry. It should also be noted that the small (scaled down) valve is performing better than the large valve.

4.3. Experimental results on the actuation energy

The actuation energy E_{act} of the turning valve is an important parameter in the design process of portable microsystems. It is defined for one cycle of opening and closing as

$$E_{act} = \tau\pi, \tag{9}$$

	rod. diam. [μm]	contact length [μm]	nominal area [μm^2]	$\sigma_{r\theta}$ [MPa]	E_{act} [mJ]
large valve	1990	23000	144	0.081	36
small valve	250	6000	4.76	0.081	0.15
	stroke volume [μL]	prestress [10^5 Pa]			E_{act} [mJ]
check valve	0.160	0.1			1.6×10^{-3}

Table 5. Actuation energy E_{act} and other parameters obtained from data fits. The friction coefficient was measured to $\eta = 0.5 \pm 0.1$, and for Poisson's ratio $\sigma = 0.49$ was used. The friction stress is evaluated at $u_5/r_3 = 0.32$.

where τ is the torque and π is the turning angle in radians of two times a quarter-turn. If we desire a microvalve with, say, a threshold pressure of at least 0.35 MPa, then according to table 4 a relative displacement of $u_5/r_3 = 0.32$ would be required. Using the results from figure 10 and equation 6 yields a friction stress of $\sigma_{rr} = 0.081$ MPa, and from there via the calculation of the torque we arrive at an actuation energy of $E_{\text{act}} = 36$ mJ. Similarly, for the small turning valve we obtain $E_{\text{act}} = 0.15$ mJ, see also table 5.

In table 5 we also compare the turning valves to a typical check valve in terms of activation energy. As an example we have chosen the pre-stressed inlet check valve from a micropump constructed by Maillefer *et al.* [13], and the actuation energy is here calculated as the product of the stroke volume and the opening pressure. Disregarding viscous friction, it is noted that the check valve can be actuated approximately 94 times for the amount of energy required by a turning microvalve. However, the turning valve provides a higher safety level, and it needs only be activated to change from one state to another. Its energy consumption is thus largely independent of the flow rate and the dosed volumes. Consequently, depending on specific parameters (e.g., stroke volume of the pumps involved) there is a volume threshold above which the turning valve is clearly more economical with regard to energy consumption.

5. Discussion and conclusion

We have studied sealing and friction in elastic silicone-based microchannels, and have shown that the friction force scales linearly with the apparent contact area and with the relative displacement of the channel wall. Two turning valves of different sizes constructed from similar materials showed the same linear scaling as well as predictable threshold pressures. It can thus be concluded that it is possible by down scaling to construct a low energy valve with a high pressure seal. Even though the principle of the turning valve is simple and well-known, we believe that this is the smallest realization of the valve to date.

The presented analysis is based on simple modelling and variations in only

a few prinicipal parameters such as size and elastic displacement. Variations in other parameters playing a role for realistic everyday operation conditions, such as temperature and a fast actuation time, have so far been neglected. A more rigorous study on how these parameters influence the performance of the turning valve is desirable and necessary for true robust design.

Acknowledgments

We would like to thank our colleagues at Novo Nordisk Jan Jakobsen, Bjørn G. Larsen, Steffen Hansen, Jan Preuthun, Klaus Bendix, Ion M. Sivebæk and Gabriel Jørgensen for fruitful discussions on design, fabrication, and test.

References

[1] Woias P, Mastrangelo C H and Becke H 2001 *Proc. SPIE* **4560** 39-52
[2] Laser D J and Santiago J G 2004 *J. Micromech. Microeng* **14** R35R64
[3] Ducrée J, and Zengerle R (editors), *FlowMap Microfluidics Roadmap for the Life Sciences*, Books on Demand GmbH, Norderstedt, Germany, 2004, ISBN:38334-0744-1.
[4] Taylor W A 1996 *SOCE News, The Society of Concurrent Engineering* **Spring 1996 issue** 1-6
[5] Quake S A and Scherer A 2000 *Science* **290** Issue. 5496, 1536-1540
[6] Hasselbrink E F, Shepodd T J and Rehm J E 2002 *Anal. Chem.* **74** 4913-4918.
[7] Kirby B J, Shepodd T J and Hasselbrink E F 2002 *J. Chromatography A* **979** 147-154
[8] Frank J A, Pisano AP 2003 *Proc. Transducers, Solid-State Sensors, Actuators and Microsystems, 12th International Conference on*, **1** 143 - 146.
[9] Persson B N J, Albohr O, U Tartahlino, Volokitin A I and Tossatti E. 2005 *J.Phys.: Condens. Matter* **17** R1-R62.
[10] Grosch K A 1963 *Proc. Royal Soc. London, Series A, Matehematical and Physical Sciences*, **274** 21-39
[11] Schallamach A 1952 *Proc. Phys. Soc.*, **65**, part 9, Sep. 1, 1952, No. 939 B.
[12] Mal A K and Singh S J 1991 *Deformation of elastic solids* (Englewood Cliffs NJ: Prentice Hall)
[13] Maillefer D, Gamper S, Frehner B, Balmer P, van Lintel H and Renaud P 2001 *Technical Digest. MEMS 2001. 14th IEEE International Conference on Micro Electro Mechanical Systems* 413-17

Bibliography

[1] The World Healt Organisation is the United Nations specialized agency for healt. On the international website www.who.int is found more information on the prevalence of diabetes, and WHO's Diabetes Programme. The website was last accessed april 2006.

[2] External Novo Nordisk presentation on diabetes, Introduction to diabetes mellitus, 2002

[3] External Novo Nordisk presentation on diabetes, Protein Delivery Systems

[4] Bitsch L, Kutter J P, Storgaard-Larsen T, Bruus H, *Low-energy, turning microvalve with high-pressure seal: sealing and friction*, JMM, (submitted 2006).

[5] Bitsch L, Olesen L H, Westergaard C H, Bruus H, Klank H, and Kutter J P, Micro particle-image velocimetry of bead suspensions and blood flows, Exp. Fluids **39**, 507 (2005).

[6] Bitsch L, Bruus H, and Kutter J P, *Minimization of performance variations in microfluidic components using the method of robust design*, MicroTAS-2004, Malmö, Sweden, September 2004, proc. vol. 1, p. 572-574

[7] Bitsch L, Olesen L H, Westergaard C H, Bruus H, Klank H, and Kutter J P, *Micro PIV on blood flow in a microchannel*. MicroTAS 2003, Lake Tahoe, USA, October 2003, proc. vol. 1, p. 825-828.

[8] Bitsch L, Olesen L H, Westergaard C H, Bruus H, Klank H, and Kutter J P, *Transmission micro PIV resolving velocities normal to the focal plane*. MicroTAS 2003, Lake Taho, USA, October 2003, proc. vol. 1, p. 821-824.

[9] Bitsch L, Storgaar-Larsen T, and Nielsen O C, *Pump assembly with active and passive valve*, 2005 (patent pending)

[10] Jens Ducrée and Roland Zengerle [editors], *FlowMap Microfluidics Roadmap for the Life Sciences*, Books on Demand GmbH, Norderstedt, Germany, 2004, ISBN: 38334-0744-1.

[11] *www.diabetesnet.com* The Diabetes Mall is an independent source for diabetes information, and diabetes books. Last accessed the April 2006.

[12] Woias P, Mastrangelo C H and Becke H, *Micropumps - summarizing the first two decades*, 2001, *Proc. SPIE*, **4560** 39-52

[13] Laser D J and Santiago J G, *A review of micropumps* 2004 *J. Micromech. Microeng.*, **14**, R35-R64

[14] Maillefer D, Gamper S, Frehner B, Balmer P, van Lintel H and Renaud P,*A high-performance silicon micropump for disposable drug delivery systems* , 2001 *Technical Digest. MEMS 2001. 14th IEEE International Conference on Micro Electro Mechanical Systems* 413-17

[15] Spencer W J, Corbett W T, Dominguez L R, and Shafer B D, *An Electronically Controlled Piezoelectric Insulin Pump and Valves*, 1978, *IEEE Transactions on Sonics and Ultrasonics* **25**, Issue 3, 153-156

[16] Smits J G, 1990, *Piezoelectric Micropump with Three Valves Working Peristaltically*, *Sensors and Actuators*, **21** Issue 1, 203-206

[17] van Lintel H T G, van de Pol F C M, and Bouwstra S, *A Piezoelectric Micropump Based on Micromachining of Silicon*, 1988, *Sensors and Actuators*, **15** Issue 2, 153-167.

[18] Unger M A, Chou H-P, Thorsen T, Scherer A, Quake S R, *Monolithic Microfabricated Valves and Pumps by Multilayer Soft Lithography*, 2000, *Science* **288** Issue.5463 113-115.

[19] Commercial website for integrated fluidic circuits (IFC), *www.fluidigm.com*, last accessed April 2006.

[20] Hasselbrink E F, Shepodd T J, Rehm J E, *High-Pressure Microfluidic Control in Lab-on-a-Chip Devices Using Mobile Polymer Monoliths*, Analytical Chemistry, **74**, 19, pp. 4913-4918, 2002.

[21] Kirby B J, Shepodd T J, Hasselbrink E F, *Voltage-addressable on/off microvalves for high-pressure microchip separations*, Journal of Chromatography A, **979**, 1-2, pp. 147-154, 2002.

[22] Gilberson R G, and Busch J D, A survey of microactuator technologies for future spacecraft missions, The Journal of The British Interplanetary Society, **49**, pp. 129-138, 1996.

[23] Dr. Fritz Faulhaber GMBH & CO. KG, Schönaich, Germany. Website, www.faulhaber.de. Website last accessed April 2006.

[24] Nguyen N-T, and Wereley S T, *Fundamentals and applications of microfluidics*, 2002, Atrech house, inc, Norwood, MA 02062.

[25] Doffing F, Drese K S, 2005, *Low-cost on-chip valves for lab-on-a-chip Applications*, personal correspondance

[26] Hartshorne H, Backhouse C J, Lee W E, 2004, *Ferrofluid-based microchip pump and valve*, *Sensors and Actuators B*, **99**, 2004, 592-600.

[27] Frank J A, Pisano AP, *Low-leakage micro gate valves* 2003 *Proc. Transducers, Solid-State Sensors, Actuators and Microsystems*, *12th International Conference on*, **1** 143 - 146.

[28] Gravesen P, Branebjerg J, Jensen O S, 1993, *Microfluidics - a review*, *J. Micromech. Microeng.* **3**, Issue.4, 168-182.

[29] Trebotich D, Chang W, Liepmann D, (2001) *Modeling of blood flow in simple microchannels*, *Proc. Modeling and Simulation of Microsystems 2001*, 218-222

[30] Sugii Y, Nishio S, Okamoto K, (2002) *In vivo PIV measurements of red blood cell velocity field in microvessels considering mesentery motion*, *Physiol. Meas.* **23**, 403-416

[31] Koutsiaris A G, Mathioulakis K S, Tsangaris S,(1999) *Microsope PIV for velocity-field measurement of particle suspensions flowing inside glass capillaries*, *Meas. Sci. Technol.* **10**, 1037-1046

[32] Meinhart C D, Wereley S T, Santiago J G, (1999) *PIV measurements of a microchannel flow*, *Exp. Fluids*, **27**, 414-419

[33] Olsen M G, Adrian R J, (2000), *Out-of-focus effects on particle image visibility and correlation in microsopic particle image velocimetry*, *Exp. Fluids* **[Suppl.]**, S166-s174

[34] Fung Y C, 1993, *Biomechanics*, 2nd ed., Springer-Verlag

[35] Nikas G K, 2003, *Elastohydrodynamics and mechanics of rectangular elastoremeric seals for reciprocating piston rods*, *Journal of tribology*, **125**, Jan 2003, 60-69.

[36] Persson B N J, Albohr O, Tartaglino U, Volokitin A I, 2005, *On the nature of surface roughness with application to contact mechanics, sealing, rubber friction and adhesion*, *J. Fys.: Condens. Matter* **17** (2005), R1-R62

[37] Schallamcach A, 1971, *How does rubber slide?*, *Wear*, **17** (1971), 301-312

[38] Grosch K A, 1963, *The relation between the friction and visco-elastic properties of rubber*, *Proceedings of the Royal Society of London*, Series A, Mathematical and Physical Sciences, **274**, No. 1356 (Jun. 25, 1963), 21-39

[39] Persson B N J, 1998, *Sliding friction*, Springer-Verlag

[40] Schallamach A, 1952, *The load dependenceof rubber friction*, **65**, Part 9, No. 393 B, (Sep. 1, 1952)

[41] Mal A K and Singh S J 1991 *Deformation of elastic solids* (Englewood Cliffs NJ: Prentice Hall)

[42] Bird R B, Armstrong R C, Hassager O, 1977, *Dynamics of polymeric liquids*, Wiley, New York.

[43] *KLOEHN Ltd.* fluidic components and subassemblies, *www.kloehn.com.* Last accessed April 2006.

[44] Upchurch Scientific, fluidic components, *www.upchurch.com.* Last accessed April 2006.

[45] *Maxon motor*, high preceesion drives and systems, *www.maxonmotor.com.* Last accessed April 2006.

[46] *Comsol*, multiphysics, *www.comsol.com.* Last accessed April 2006.

[47] The laser cut holes were created by Martin F. Jensen *Teknologisk Institut*, *www.danishtechnology.dk.* Last accessed April 2006.

[48] Taylor W A, 1996, *The Society of Concurrent Engineering, SOCE News*, Spring 1996 issue, p.1-6.

[49] Hastrup K, 1992, *Plast og gummi ståbi*, Teknisk Forlag, København 1992 ISBN 87 571 1380-7, only in Danish.